DEVELOPMENT OF CEMENTITIOUS MATERIALS FOR EXTRUSION-BASED 3D PRINTING

A THESIS

submitted by

A. V. RAHUL

for the award of the degree

of

DOCTOR OF PHILOSOPHY

DEPARTMENT OF CIVIL ENGINEERING
INDIAN INSTITUTE OF TECHNOLOGY MADRAS.

MARCH 2020

THESIS CERTIFICATE

This is to certify that the thesis titled **DEVELOPMENT OF CEMENTITIOUS MATERIALS FOR EXTRUSION-BASED 3D PRINTING**, submitted by **A.V. Rahul**, to the Indian Institute of Technology Madras, for the award of the degree of **Doctor of Philosophy**, is a bona fide record of the research work done by him under our supervision. The contents of this thesis, in full or in parts, have not been submitted to any other Institute or University for the award of any degree or diploma.

Prof. Manu Santhanam
Research Guide
Professor
Dept. of Civil Engineering
IIT Madras, 600 036

Dr. Atul Narayan
Research Guide
Assistant Professor
Dept. of Civil Engineering
IIT Madras, 600 036

Place: Chennai

Date:

ACKNOWLEDGEMENTS

I would like to express my gratitude to all the many people who have supported me during the last three and a half years in the work leading to this doctoral thesis. First and foremost, I would like to thank my supervisors, Prof. Manu Santhanam and Dr. Atul Narayan for giving me the chance to work with them, for constantly motivating me, and for the regular discussions and feedback. I am also thankful to IIT Madras for accepting me as a Ph.D. student and for letting me use the lab facilities. I thank Prof. Narayanan Neithalath for allowing me to do an exchange program at Arizona State University and for his valuable suggestions during the exchange period. I thank Prof. Murali Krishnan for his guidance during the preliminary studies, his suggestions as a doctoral committee member, and also for allowing me to use the lab facilities in the transportation division.

I am thankful to my friends and employees of Tvasta–Industrial 3D Printing, particularly Adithya, Parivarthan, Pragadeeshwar and Yuvraj for designing the concrete 3D printers used and also providing the automation and software support for this Ph.D. work. Special thanks to Zimam and Hitesh for being good friends, for their help received while conducting the experiments and for the stimulating discussions.

Thank to all my friends and colleagues in the BTCM division and also other division in IIT Madras, especially Sachin, Nithya, Manu and Biju. I am also thankful to all the lab staff in the BTCM division for the help received while conducting the experiments.

My love and thanks to my beloved and caring wife Anjana for all the emotional support and motivation during the difficult times. Finally, my wholehearted thanks to my brother and parents, especially my mother Ajitha for understanding and allowing me to pursue this Ph.D. work.

ABSTRACT

KEYWORDS: Extrusion-based 3D printing; Yield stress-based mix design approach; Desorptivity; LECA; Thermodynamic-based modelling

Extrusion is a process in which a moldable material is forced through a die to fabricate an element with a desired cross-section. In the construction industry, its use has been limited to the manufacturing of precast panels and pipe segments. However, with the recent advent of digital fabrication methods, the extrusion process started to gain more interest in the construction industry. The most common among the digital fabrication methods is extrusion-based concrete 3D printing. It is a technique in which a structure is built by the layerwise deposition of a continuously extruded material. The current study presents the mixture development of cementitious materials suitable for such applications. Two types of 3D printer are used in the study, viz., a small scale screw pump-based system, wherein the material is conveyed continuously by the use of an Archimedes screw, and a larger scale piston pump-based system, wherein the material is first filled inside a piston-cylinder and then forced out by using a ram extruder.

The study comprises of four stages. In the first stage, the mix development for the small-scale printer system is carried out. Test methods for assessing various aspects related to 3D printing such as extrudability, buildability, robustness and the assessment of structural build-up with time were developed. The role of special additives like nanoclay, micro-silica and viscosity modifying agent (VMA) in developing extrudable mixes was investigated. The maximum robustness was obtained for the mix containing VMA while the structural build-up was maximum for the mix with micro-silica addition.

The second stage involved the mixture development for the large-scale 3D printer system. For the large-scale system, a key aspect is the liquid phase separation in the concrete that may occur due to the high pressure applied during the extrusion process. Desorptivity, a parameter derived from a soil mechanics theory, was used to assess the water retention capacity of the mixes formulated for the large-scale printer. The addition

of methylcellulose was found to increase the desorptivity, and therefore decrease the tendency for phase separation during the extrusion process. Extrudability tests were conducted for a wide range of mixes and a desorptivity-based index was proposed to assess the phase separation during the extrusion process. Further, mixes incorporating coarse aggregates were also developed. Light weight expanded clay aggregates (LECA) of maximum size 10 mm were used as the coarse aggregates. It was possible to extrude mixes with up to 30 % coarse aggregate addition.

For the mixes developed for the larger 3D printer, the buildability was assessed using uniaxial compression tests on fresh concrete, performed after different rest durations of 0 to 420 minutes after casting. For both mixes with and without LECA addition, the younger specimens (up to 180 min) showed an elasto-plastic type response, while the older ones (beyond 180 min) exhibited a strain-softening type response, more typical of hardened concrete. The strength and elastic modulus of the concrete increased with LECA addition at all ages which may be due to the higher amount of dewatering that occurs with increase in LECA content. Finally, the effect of using low density aggregates on plastic and buckling type collapse that may occur during printing are also discussed.

The third stage of the study involved the assessment of the mechanical characterization of 3D printable concrete. The compressive and flexural strength of printed elements were determined and compared with normal mould cast concrete. The compressive strength of the printed concrete was similar when tested in different loading directions but lower by 12-22 % as compared to the mould cast concrete. The flexural strength was found to depend on the region subjected to the maximum bending moment. When tested along the direction where the maximum bending moment occurs at the interfaces between layers, the flexural strength was lower by about 32-40 % while it was higher by 13-20 % when tested in directions where maximum bending stress is induced in the bulk concrete. To understand the effect of interfaces on mechanical behaviour, porosity assessments and bond shear tests were carried out. It was found that the bulk in 3D printed elements has a lower porosity as compared to mould cast concrete while the interfaces are relatively weak with higher porosity. Similar trends were also observed in comparing the bond shear tests in printed elements with shear strength of mould cast concrete.

The fourth and final stage of the study involved developing a rheological model for cement paste using a thermodynamic framework. In developing the model, it is assumed that the material has multiple natural configurations, such that the evolution of natural configuration with time is based on the maximum rate of dissipation criterion. Thixotropic behaviour was captured in the model by making the Helmholtz potential as a function of a structural parameter and the rate of dissipation as a function of its time derivative. To corroborate with experimental results, steady shear and step shear experiments were performed using cement paste. The predictions from the model were found to match well with the experimental data. The developed model can be useful in performing computer simulation of the extrusion process, which can be considered as a future extension of this work.

TABLE OF CONTENTS

LIST OF TABLES

LIST OF FIGURES

ABBREVIATIONS

RM	Rapid Manufacturing
SCC	Self-Compacting Concrete
VMA	Viscosity Modifying Admixture
HRWA	High-Range Water-Reducing Admixture
FBRM	Focused Beam Reflectance Measurement
RPM	Rotations per Minute
HPMC	Hydroxypropyl Methylcellulose
PEG	Polyethylene Glycol
LECA	Light Weight Expanded Clay Aggregate
CEM	Concrete Equivalent Mortar
SSA	Specific surface area

NOTATION

M	Torque
Y	Yield stress
V	Variability factor for assessing robustness
I	Index for assessing phase separation during extrusion
I_{norm}	Index, I normalized with respect to the water content in the mix
$\tau_c(t)$	Uniaxial compressive strength of mortar measured at a time t
$E(t)$	Elastic modulus at time t measured from the uniaxial compression tests
κ_r	Reference configuration
κ_r	Current configuration
κ_r	Natural configuration
$\mathbf{F}_{\kappa_r}$	Gradient of the mapping from $\kappa_r \mapsto \kappa_t$
$\mathbf{F}_{\kappa_p}$	Gradient of the mapping from $\kappa_p \mapsto \kappa_t$
$\mathbf{G}$	Gradient of the mapping from $\kappa_r \mapsto \kappa_p$
$\mathbf{L}$	Velocity gradient tensor
$\mathbf{D}$	Symmetric part of velocity gradient tensor
$\mathbf{T}$	Stress tensor
$\hat{\mathbf{T}}$	Deviatoric part of stress tensor
ξ	Rate of dissipation function
ψ	Helmholtz potential
λ	Structural paramater

CHAPTER 1

INTRODUCTION

Rapid manufacturing (RM) is a method of fabricating components directly from a computer model, with little or no human intervention (Pham and Gault, 1998). The term, in general, encompasses a family of digital fabrication techniques like stereolithography (Jacobs, 1992), fused deposition modelling (Mohamed *et al.*, 2015), selective laser sintering (Bourell *et al.*, 1992) and 3D printing (Gross *et al.*, 2014). Such techniques have proven to be beneficial in many industrial processes. Many industries such as automotive, aerospace, and industries manufacturing consumer based products have been successfully using various RM techniques to optimize the cost and time of their manufacturing process (Wohlers, 1998). Despite these advantages offered by RM, the construction industry has not utilized the opportunity yet. It has lagged behind the other industries in using automation and implementing the same level of technological advancement (Martinez *et al.*, 2008).

But recently, both industries and academia in the construction sector have begun active research in developing digital fabrication methods. In this chapter, an overview about such methods, with a more detailed description on the extrusion-based concrete 3D printing is presented. This is followed by the objectives and the scope of the study. Finally, the overall methodology adopted in the study and the arrangement of the remaining chapters of the thesis is presented at the end of this chapter.

1.1 Digital fabrication methods in the construction industry

Traditionally, concreting involves the mixing of aggregates, cement, water, and in some cases supplementary cementitious materials and chemical admixtures. This fresh concrete is then transported by various means and then placed. Since it does not have enough strength to maintain the desired shape in the fresh state, a formwork is needed to support it. After placing it in the form, the concrete is subjected to compaction for removing the entrapped air voids. This traditional method is labour-intensive, and the need for formwork and achieving high compaction provides a restriction on the possible design and geometry of the structure (Martinez *et al.*, 2008). For instance, Figure 1.1 shows the cost distribution for a typical construction project. More than 50 % of the total cost is attributed to the cost of formwork and labour (Jha, 2012). Use of digital fabrication methods can provide an innovative solution to such problems (Buswell *et al.*, 2007, 2008; Lim *et al.*, 2012). An extensive review on applying such methods in the construction industry can be found in the work by Wangler *et al.* (2016). Mesh mould casting, particle-bed 3D printing, smart dynamic casting and extrusion-based concrete 3D printing are some methods that have been developed in the recent times.

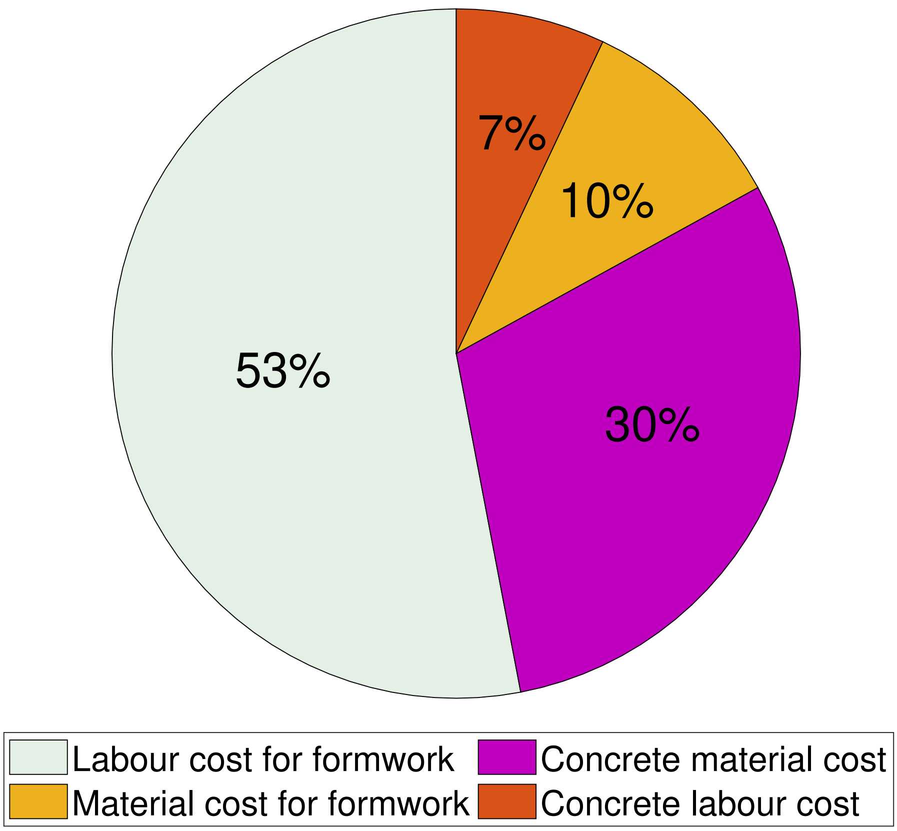

Figure 1.1: Cost distribution for a typical construction project (Jha (2012))

Mesh mould casting is a process of fabrication which uses an industrial robot to bend and weld metal wires to from a three-dimensional mesh structure (see Figure 1.2). Once the robot completes the mesh fabrication, concrete is poured inside the mesh with the mesh itself acting as the formwork. Therefore, the digitally fabricated mesh serves a dual purpose; it acts as the formwork for the fresh concrete, and it also acts as the reinforcement for meeting the structural requirements (Hack and Lauer, 2014; Hack *et al.*, 2015, 2017; Sandy *et al.*, 2016; Kumar *et al.*, 2017; Buchli *et al.*, 2018).

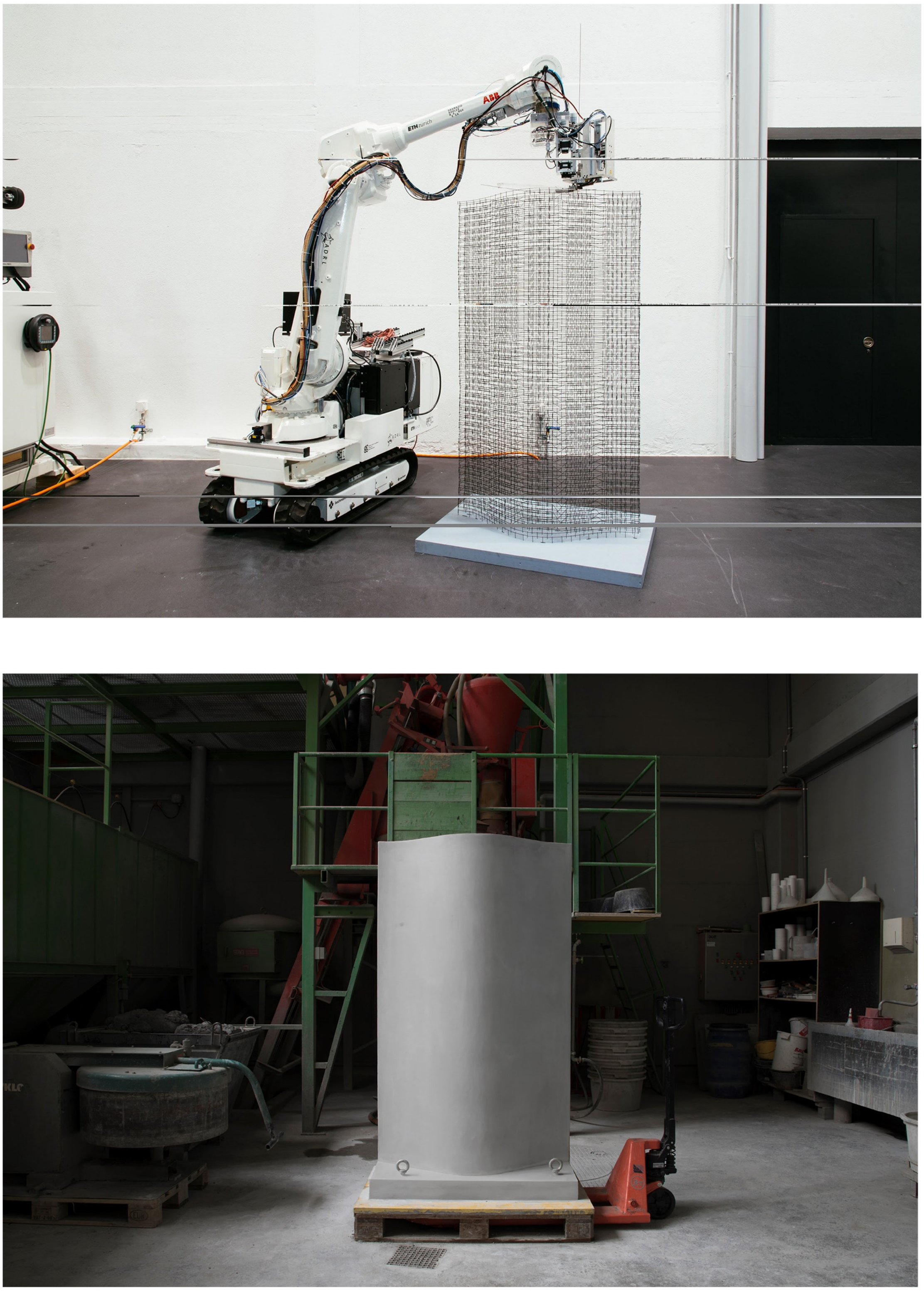

Figure 1.2: Mesh mould casting (taken from Buchli *et al.* (2018))

Figure 1.3: A column segment fabricated by binder activation technique (taken from Lowke *et al.* (2018))

Another digital fabrication construction method that does not require a component-based formwork is particle-bed 3D printing. The process essentially consists of two steps: (i) the deposition of dry particles, and (ii) the application of a fluid phase on top of the deposited dry particle layer at certain specific locations. Based on a computer model, the two steps are repeated one after the other until the entire component is fabricated. Particle-bed 3D printing applicable to construction can be categorized into three sub-classes, namely, binder jetting, selective binder activation and paste intrusion (Lowke *et al.*, 2018). In the binder activation technique, the particle bed consists of a mixture of fine aggregates and cement. The binder present in the particle bed is then activated by spraying water or a solution of water mixed with chemical admixtures at specific locations on the particle bed. Figure 1.3 shows a segment of a column fabricated by binder activation technique. In selective paste intrusion, the particle bed consists solely of fine aggregates. A paste consisting of cement, water and chemical admixtures are then sprayed, which intrudes though the particle bed and provides the required binding. In binder jetting technique, a particle bed consisting of aggregates along with a hardener is activated by the spraying of a resin. The resin and the hardener then react to bind the matrix together. Apart from academia, industries have also been actively involved in the development of particle-bed 3D printing techniques. For instance, a large-scale particle-bed 3D printer called D-shape was developed by Dini (D-shape, 2019). Figure 1.4 shows a sculpture called 'Underwater Moma' constructed using D-shape.

Figure 1.4: Underwater Moma, a 3D printed underwater sculpture (taken from D-shape (2019))

Recently, ETH Zurich developed a digital improvisation of conventional slipforming technique called smart dynamic casting (Lloret *et al.*, 2015). In this method, the concrete is slipformed though a robotically moving formwork. The cross-section of the formwork is varied dynamically to produce custom-shaped vertical elements such as that shown in Figure 1.5. The concrete initially enters the slipforming system in a fluid state, but after exit, it is transformed to a hardened state through hydration control achieved by adding accelerators in small increments. An inline feedback system is used to control the rate of the upward movement of formwork (Lloret-Fritschi *et al.*, 2017).

Figure 1.5: A column with varying cross-section fabricated by smart dynamic casting (taken from Wangler *et al.* (2016))

1.2 Extrusion-based concrete 3D printing

Extrusion is a process in which a moldable material is forced through a die to fabricate an element with a desired cross-section. The material is extruded out at a constant displacement rate, either using a screw-pump-based system, wherein the material is conveyed continuously by the use of an Archimedes screw, or a piston-pump-based system, wherein the material is first filled inside a piston-cylinder and then forced out by using a ram extruder (Perrot *et al.*, 2018).

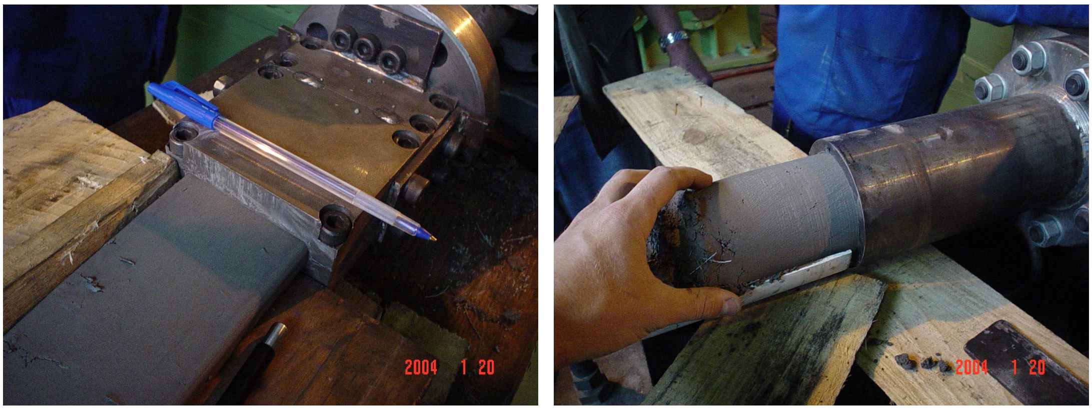

Figure 1.6: Plate and pipe elements manufactured using extrudable cement composites (taken from De Koker and van Zijl (2004))

So far, the use of extrusion process has been limited to the manufacturing of small precast panels and pipe segments (see Figure 1.6). However, with the recent advent of extrusion-based 3D printing, the process has started to gain more interest in the construction industry. Extrusion-based 3D printing (or simply 3D printing) is a digital fabrication technique which combines extrusion process with additive manufacturing. In this method, a structure is fabricated by a layerwise extrusion of cementitious materials (see Figure 1.7), based on a predefined three-dimensional computer model. For a typical 3D printing process, the first step is to slice the 3D model in the STL (standard tessellation language) file format into many individual filament layers and generate a set of machine instructions called G-codes. This can be achieved by using open source software like Slic3r (2019). Then, a user-interface/control software is used for communicating with the 3D printer using the G-codes. Finally, the material is extruded out through the print head based on the print path dictated by the G-codes. Instead of using a separate slicing and user-interface software, programs like Repetier-Host (2019) can also be used which can serve a dual purpose of both slicing and also provide the user-interface for controlling the 3D printer.

Figure 1.7: Layerwise deposition of concrete in extrusion-based 3D printing

Extrusion-based 3D printing is the most extensively studied among the different digital fabrication techniques, by both industries and academia. This is because, compared to other digital fabrication methods, extrusion-based 3D printing is scalable, i.e, the process can applied to manufacture small architectural elements to very large-scale structures. The earliest work of using the technology in the construction industry was by Pegna (1997), and later it was popularized by Khoshnevis who invented the technique of contour crafting (Khoshnevis and Dutton, 1998). Contour crafting is a 3D printing technique which uses a side trowel to provide a good surface finish to the extruded filament (see Figure 1.8). Therefore, print quality is superior in contour crafting compared to conventional 3D printing techniques (Khoshnevis, 2004; Khoshnevis *et al.*, 2006).

Following the invention of contour crafting, there has been a rapid rise in the use of 3D printing in the construction industry. Figure 1.9 shows its growth in the recent times, particularly with regard to developing large-scale structures. Today, there are numerous research groups and also industries working in the area of concrete 3D printing. Among these, some noteworthy mentions are freeform construction developed at the University of Loughborough (Lim *et al.*, 2012) and the projects by the companies like Winsun, ApisCor and TotalKustom. Figures 1.10 and 1.11 show full-scale structures 3D printed by the companies TotalKustom and Winsun respectively.

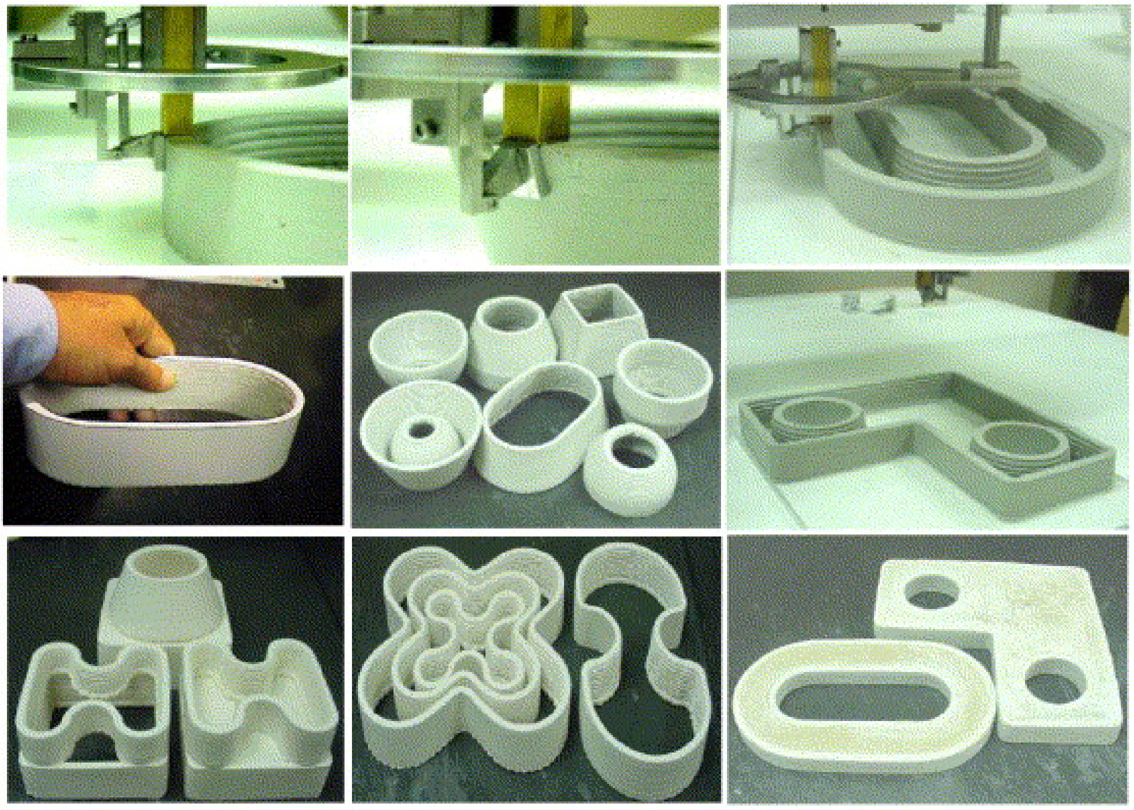

Figure 1.8: 3D printed elements with good surface finish by contour crafting technique (taken from Khoshnevis (2004))

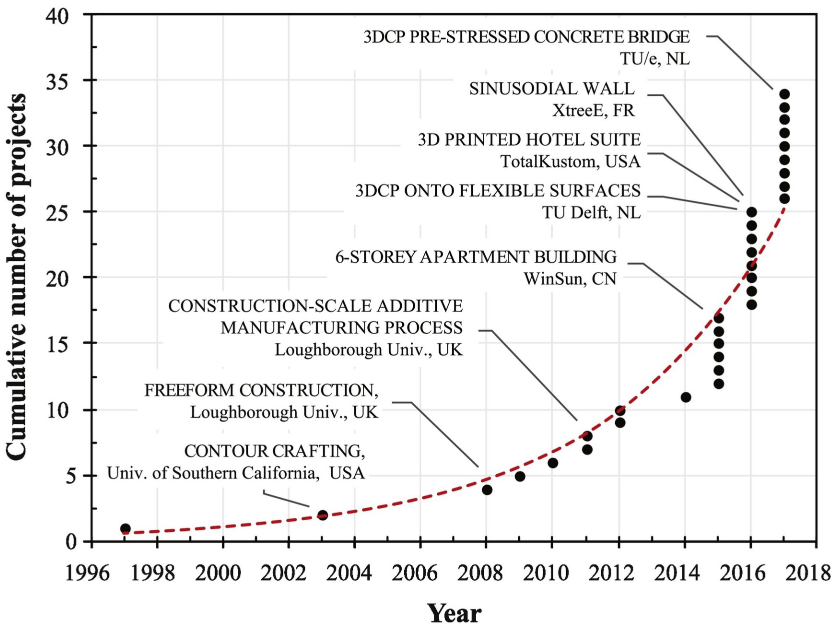

Figure 1.9: Growth of large-scale 3D printing in the construction industry (taken from Buswell *et al.* (2018))

(a)

(b)

Figure 1.10: (a) 3D printing of a suite room of size 12.5 $\times$ 10.5 $\times$ 4 m in Lewis Grand Hotel, Philippines by TotalKustom (b) Completed and furnished suite room (taken from TotalKustom (2019))

Figure 1.11: Wave-shaped 3D printed building (taken from Winsun (2019))

1.2.1 3D printer systems and process parameter

The nozzle or the print head of a 3D printer can be mounted either on a gantry or a robotic arm based system. The gantry system allows 3 degrees of freedom, i.e., movements along x, y and z directions, whereas the use of a robotic arm provides a system with six degrees of freedom. However, the robotic arm based systems are more expensive and not ideal for large-scale additive manufacturing. The advantage of the robotic arm based system is that it allows to also print on curved or inclined surfaces. Figure 1.12 shows examples of gantry and robotic arm based 3D printer systems. The use of only a three degree of freedom gantry system may cause twisting at the corners of the extruded concrete filament (see Figure 1.13). Therefore, a gantry system provided with an additional fourth degree of freedom that allows for the rotation of nozzle at the corners is more commonly used.

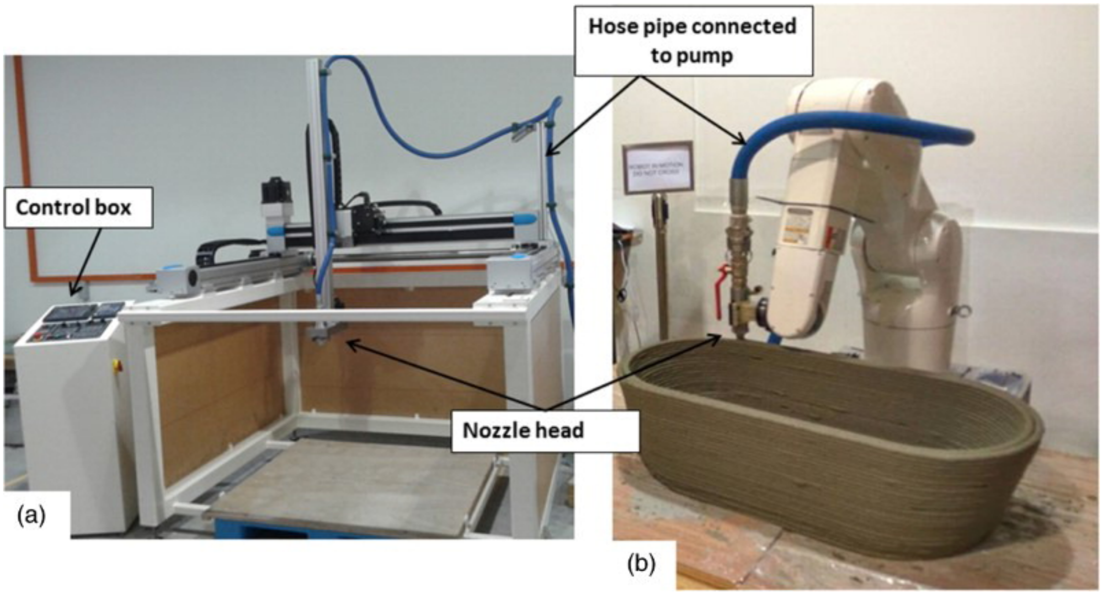

Figure 1.12: Gantry and robotic arm based 3D printer systems (taken from Tay *et al.* (2017))

Figure 1.13: Twisting at the corners of extruded concrete filaments (taken from Bos *et al.* (2016))

The process parameters for a 3D printing job include the extrusion speed, nozzle size and print speed. For an extruded filament to have the same dimension as that of the nozzle, the print speed should be calibrated based on flow rate from the pump. The calibration procedure for this will be later illustrated in section 3.2.2.

1.3 Aim of the current research work

Digital-based fabrication methods have the potential to revolutionize the construction industry. Reduction in the material wastage and labour cost, faster construction time and geometric flexibility are the advantages of using such methods. In the preceding section, the digital fabrication methods that applies to the construction were discussed in detail. Among these, the most promising is extrusion-based 3D printing. Realizing its advantages, many countries around the world have started research programs to develop the technology of extrusion-based 3D printing. Russia, China, United States, Netherlands, Germany and France are such countries, only to name a few. In a developing country like India, extrusion-based 3D printing has even bigger potential. Building of affordable houses for economically weaker section is a major problem concerning the country. The Pradhan Mantri Awas Yojana-Housing For All scheme (PMAY-HFA, 2019) was initiated in 2015 by the Prime Minister of India to develop affordable houses for the urban mass. 3D printing can be one of the ways by which the scheme can be implemented. Due to the faster construction speed, a large number of houses can be constructed within a short time. Development of fast and form-free precast elements is another domain where it could find application. But, to make the technology viable, it is important to understand the material requirements for layer-wise extrudability. This work aims to provide a better understanding of the cementitious material requirements suitable for extrusion-based 3D printing.

This work aims to understand the challenges in the mixture proportioning, both for small-scale laboratory-based and large-scale 3D printers. The work also aims to understand the mechanical behaviour of printed concrete and how its mechanical performance differs from that of conventional concrete. The need for accurate rheological models is paramount for applications like 3D printing. However, the existing models are only one-dimensional and phenomenological. This work aims to develop a complete three-dimensional rheological model for cementitious systems using a sound thermodynamic framework.

1.4 Objectives

1. To develop a systematic mixture design procedure for printable concrete and also, test methods for the assessment of buildability, extrudability, workability retention and robustness, using a laboratory-scale 3D printer.

2. To characterize the water retentivity of cementitious materials to predict the occurrence of phase separation when high extrusion pressure is applied in large-scale 3D printer systems. Further, to use this understanding to develop mixes with the incorporation of coarse aggregate for the large-scale 3D printer system.

3. To determine the compressive, flexural and bond strength of 3D printable concrete, along with porosity in the bulk and at the interfaces between layers of 3D printed specimens in comparison to mould cast specimens.

4. To develop a three-dimensional rheological model that accounts for the yielding and thixotropic behaviour of cementitious systems. The model can be useful in performing simulation studies for predicting the deformation in the layers or the occurrence of failure during the printing process.

1.5 Scope

1. The automation related work necessary for 3D printing is outside the scope of the current project.

2. The study will be limited to only portland-cement-based materials. Geopolymer and other alternative binders are not investigated in this study.

3. The special additives considered in the study are Attapulgite clay, hydroxypropyl methylcellulose (HPMC) and micro-silica.

4. The proposed rheological model is able to account for yielding and thixotropic behaviour of cement paste. The effect of cement hydration on rheology will not be accounted for in the model. The validation of the proposed model is done at a paste level and not extended to mortars and concrete.

1.6 Overall methodology and the arrangement of the thesis

The overall methodology for the entire thesis work is shown in Figure 1.14. Stage 1 involves the mix development for 3D printable concrete using a small laboratory-scale concrete 3D printer. Test methods for assessing the properties of printable concrete like extrudability, buildability, robustness and structural build-up are developed. The work carried out in Stage 1 is presented in the Chapter 3 of the thesis. Chapter 3 includes the detailed description of the methodology adopted for the experiments and the major results and conclusions pertaining to Stage 1.

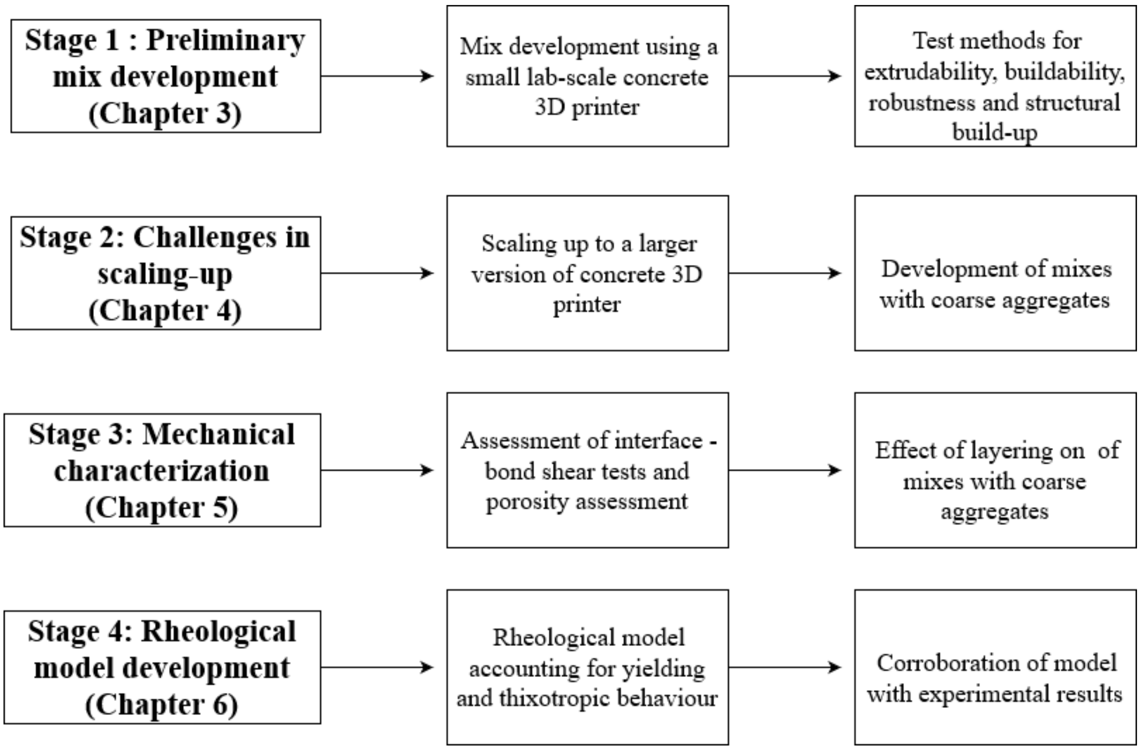

Figure 1.14: Flowchart depicting the overall methodology and the arrangement of the thesis

Stage 2 consists of mix development for a large-scale concrete 3D printer. In this regard, a key aspect is the assessment of the water drainage that may occur in concrete when subjected to the higher extrusion pressure in the large-scale 3D-printer system. Desorptivity is used a fundamental parameter to assess phase separation during the extrusion process. This understanding is then used in developing additional mixes with the inclusion of coarse aggregates. All the work pertaining to Stage 2 including the methodology is presented in Chapter 4 of the thesis.

In Stage 3, the hardened properties of 3D printable concrete are assessed and comparisons are made with respect to conventional mould cast concrete. At first, the effect of layering is studied using direct bond shear tests as well as by assessing the porosity in the bulk and at the interfaces in the bulk and at the interfaces between layers of 3D printed elements. Then, the influence of layering on the compressive and flexural strength is investigated. Finally, some perspectives on the structural design of 3D printed elements are also formulated. The methodology, results and discussions of the work carried out in Stage 3 are presented in Chapter 5 of the thesis.

Stage 4 involves the development of a three-dimensional rheological model for cement paste and its experimental corroboration. The model is developed using a thermodynamic framework. The yielding and thixotropic behavior of cement paste are accounted for in the model. The need for such models for applications like 3D printing, the development of the model framework and the experimental corroboration are presented in Chapter 6 of the thesis. Finally, in Chapter 7, the general conclusions from the overall study and the directions for future research are discussed.

CHAPTER 2

LITERATURE REVIEW

2.1 Introduction

In this chapter, a detailed literature review and the need for the current research are discussed. At first, a literature review on the rheology of cementitious systems is presented. This is followed by a review on the current approaches for the mixture proportioning of 3D printable concrete. The different techniques for assessing the resistance against phase separation that may occur during an extrusion process are also discussed. This is followed by a literature review on the mechanical properties of 3D printable concrete. Based on the literature review conducted, the need for the current research is explained in the final section of this chapter.

2.2 Rheology of cementitious system

Cement paste belongs to a class of non-Newtonian fluids that possess yield stress. When cement paste is subjected to a constant stress history, with the magnitude of the stress below a certain stress level, the deformation eventually reaches a steady state. However, if the applied constant stress is above this critical stress level, the material deforms continuously over time, at a reasonably constant rate (see Figure 2.1) (Struble and Schultz, 1993; Qian and Kawashima, 2016). If the material is subjected to a strain-sweep experiment in oscillatory shear, the apparent storage modulus of the material can be observed to decrease drastically when the strain amplitude increases beyond a critical value. Further, the apparent loss modulus can increase from a relatively low value to a value higher than the storage modulus at strain levels beyond this critical strain (see Figure 2.2) (Schultz and Struble, 1993; Qian and Kawashima, 2016). Nehdi and Rahman (2004) performed stress-sweep in oscillatory shear and made similar observations.

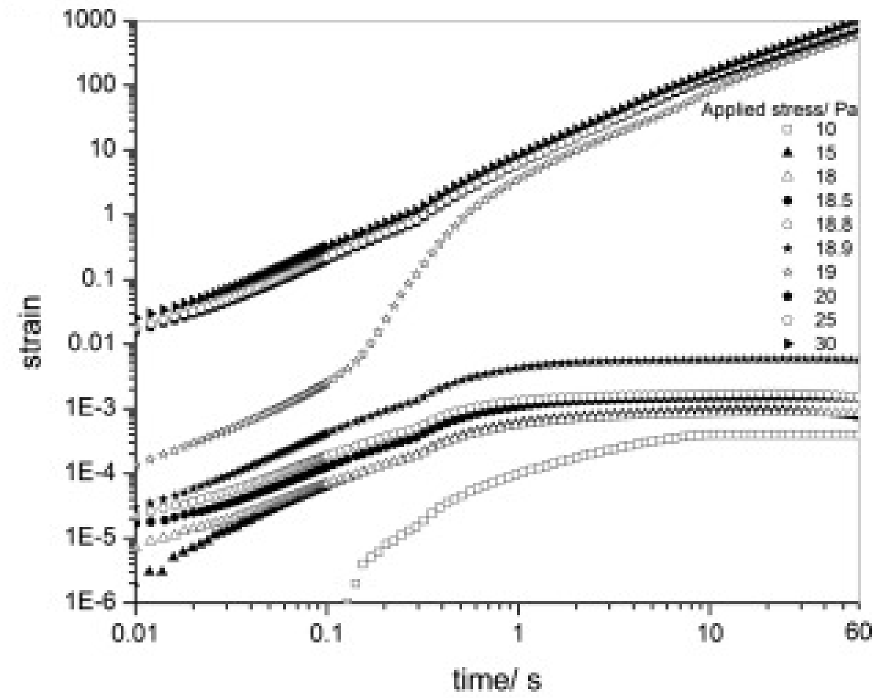

Figure 2.1: Creep test at different stress levels on a cement paste sample (taken from Qian and Kawashima (2016))

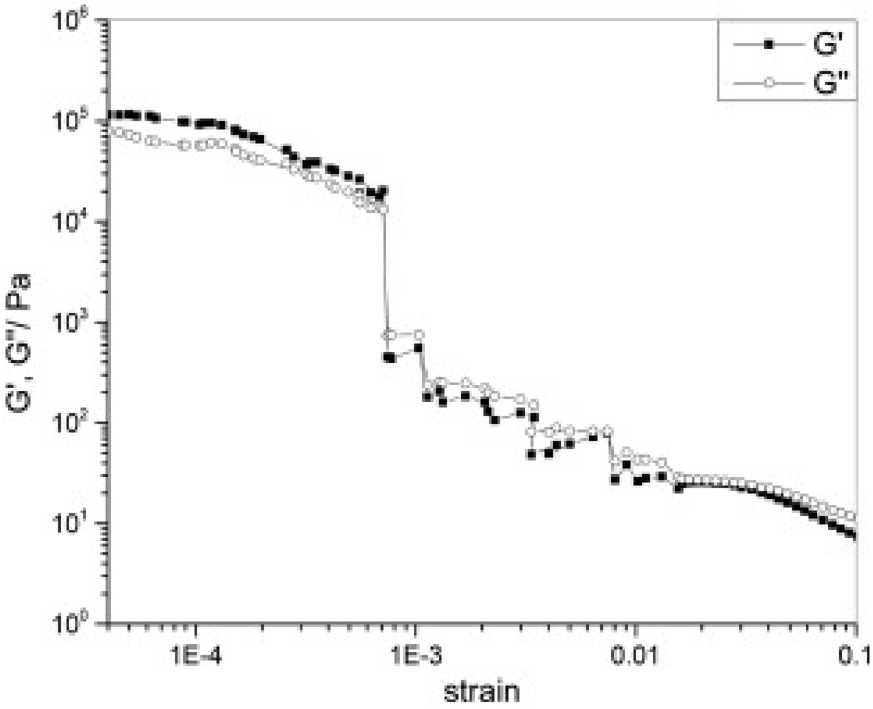

Figure 2.2: Strain sweep test on a cement paste sample (taken from Qian and Kawashima (2016))

In steady-shear experiments, the stress response of cement paste would eventually reach a steady state. If the steady-state shear stress is plotted against the respective shear-rate, and the variation is extrapolated to zero shear-rate, the corresponding shear stress is non-zero. The intercept of the variation of steady-state shear stress with shear rate can be considered as the yield stress of the material (Nessim and Wajda, 1965; Banfill and Saunders, 1981; Papo, 1988; Papo and Piani, 2004; Fernàndez-Altable and Casanova, 2006; Ferron *et al.*, 2007; Hwang *et al.*, 2009). Further, the slope of the steady-state stress versus strain rate is not a constant but a decreasing function of the strain rate. This indicates that cement paste shows a shear-thinning behavior (Lapasin *et al.*, 1979, 1983; Papo and Piani, 2004; Wallevik, 2005; Jayasree and Gettu, 2008; Wallevik, 2009).

Cement paste also exhibits thixotropic behavior. When cement paste is subjected to a steady-shear, the stress initially overshoots to a maximum value and then attains a steady-state condition. The overshoot has been found to depend on the rest duration provided prior to the test, while the steady-state stress has been observed to be independent of the rest duration (Roussel, 2005). Such history-dependent overshoots in steady-shear experiments are characteristic of thixotropic behavior. Thixotropy can also be observed in a shear ramp-up and ramp-down test. The area enclosed within the loop of shear stress vs. shear rate decreases with subsequent cycles of ramp-up and ramp-down, which is again characteristic of a thixotropic material (Williams *et al.*, 1999; Papo and Piani, 2004; Banfill, 2006; Jayasree and Gettu, 2008; Wallevik, 2009).

2.2.1 Models to describe the yielding behaviour

The yielding behaviour in cementitious systems is most commonly described by using the Bingham model. Mathematically, the Bingham model can be represented by the following equation (Bingham, 1922):

$$\begin{aligned} \text{Yield criterion:} \quad & Y \geq && \sqrt{II_T}, \\ \text{Below yield:} \quad & \dot{\gamma} = && 0, \\ \text{Above yield:} \quad & T_{12} = && Y + \eta\dot{\gamma}, \end{aligned} \tag{2.1}$$

where II_T is the second invariant of the deviatoric stress tensor. The term Y and η denote the yield stress and the plastic viscosity respectively. Until the yield criterion is satisfied, the material remains rigid with no deformation. Once the yield criterion is satisfied, the material exhibits a liquid-like behaviour (Beverly and Tanner, 1992). A graphical illustration of the Bingham model is shown in Figure 2.3. The y-intercept of the line denotes the yield stress while the slope of the line denotes the plastic viscosity. The yield stress denotes the minimum stress required to initiate flow in the material, while plastic viscosity denotes the resistance to flow, once the flow has been initiated. For cementitious systems that exhibit a shear thinning behaviour, a Herschel-Bulkley model may be used. The model is given by the following equation (Herschel and Bulkley, 1926):

$$
\begin{aligned}
\text{Yield criterion:} \quad Y &\geq \sqrt{II_T}, \\
\text{Below yield:} \quad \dot{\gamma} &= 0, \\
\text{Above yield:} \quad T_{12} &= Y + k\dot{\gamma}^n,
\end{aligned}
\tag{2.2}
$$

where k and n are called the consistency factor and flow index or power law exponent respectively.

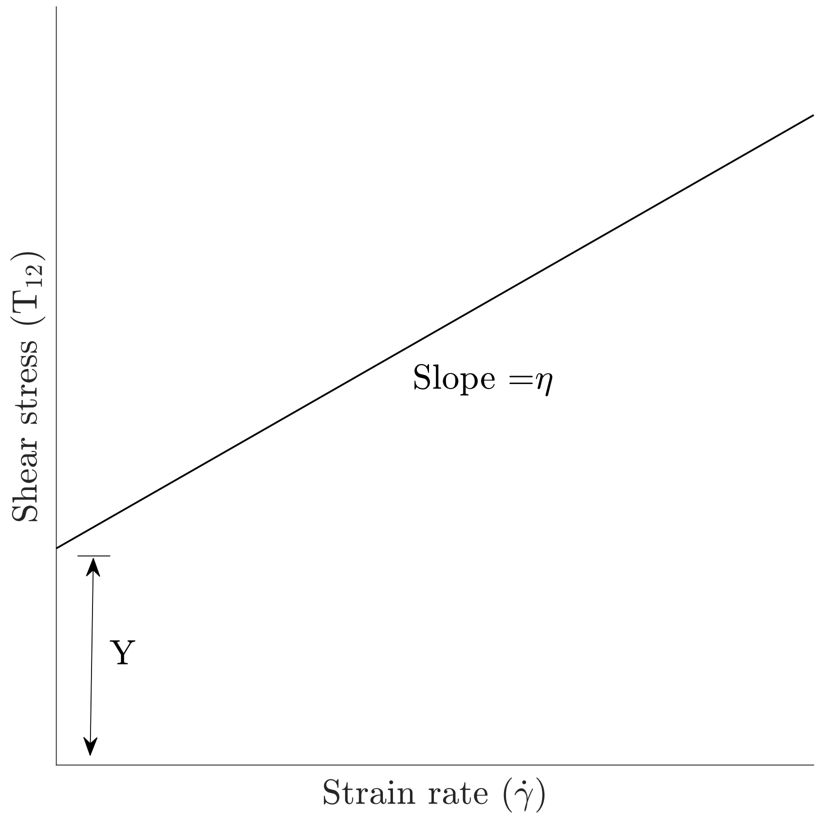

Figure 2.3: Bingham model

2.2.2 Thixotropic models

Both the Bingham and the Herschel-Buckley model does not account for the thixotropic behaviour of cement paste. Due to the complexities involved in characterizing thixotropic fluids, developing a mathematical model for describing thixotropy can be difficult. Based on the approach used, Mewis and Wagner (2009) classified thixotropic models, in general into three categories. In the first approach, memory functions are introduced in the constitutive equation for describing the time effects due to thixotropy. For instance, Goddard (2006) developed a constitutive equation for thixotropic materials by using a fourth order viscosity tensor. The viscosity tensor was assumed to be a function of a history dependant second order tensor called texture tensor. Wallevik (2005) developed a thixotropic model for cement paste along these lines. He incorporated two types of memory function in the constitutive equations, one for the history of coagulation rate and the second for the shear-rate history.

The second approach is by incorporating a structural parameter λ in the constitutive equation, using which several phenomenological models have been developed. The value of the structural parameter represents the structuration state of the material. For instance, a higher value for the structural parameter can imply an intact microstructure, whereas a lower value represents a relatively broken down microstructure. In such models, some or all of the material parameters like viscosity and modulus are made to be functions of the structural parameter. The time evolution of the structural parameter is then used to capture the build-up and breakdown of the internal microstructure (Cheng and Evans, 1965; Coussot *et al.*, 2002). Finally, there is a third category of models based on the actual microstructural changes in the material. Such models are based on changes in floc size and the Brownian collisions that may occur when the material is subjected to shear. Wallevik (2009) developed a rheological model for cement paste along these lines that predicts the mechanical behaviour due to both thixotropy and hydration.

2.2.3 Shortcomings of the current models

Although the Bingham and Herschel-Bulkley models are widely used, these models can only predict the steady state stress response of cementitious systems. As pointed out earlier, when cement paste is subjected to a constant shear rate, the stress initially overshoots to reach a peak value and thereafter decreases to reach a steady state condition. As seen in Figure 2.4, this peak value can be much higher than the steady state stress. The transient state behaviour prior to reaching the steady state cannot be captured using these models.

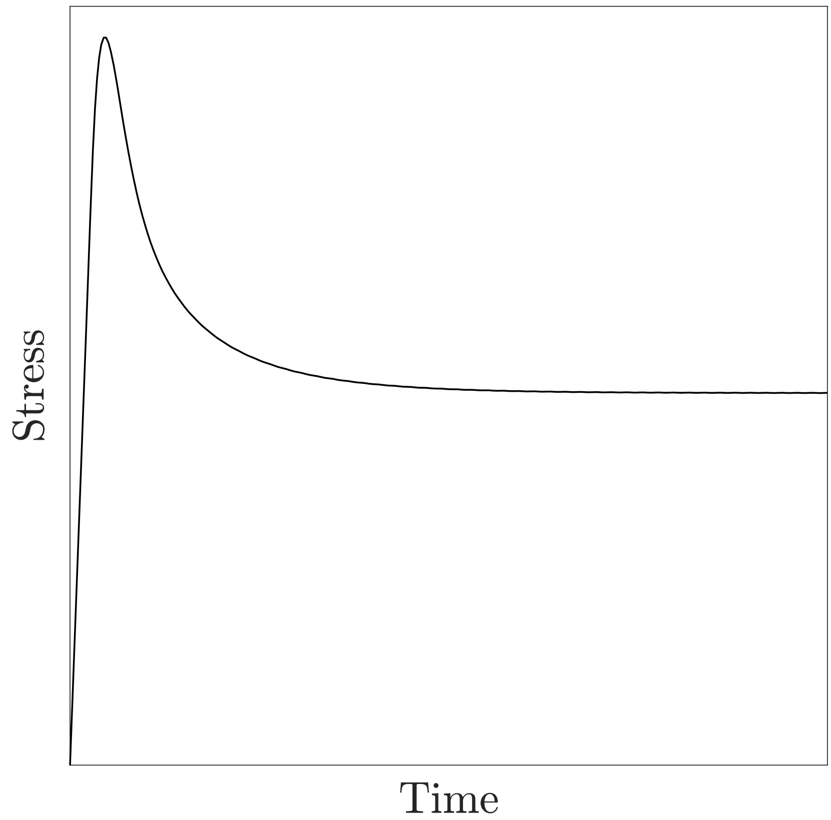

Figure 2.4: Stress overshoot in a steady shear experiment for cementitious systems

The phenomenological models such as the one developed by Coussot *et al.* (2002) can describe both the transient and the steady state behaviour of cementitious systems (Roussel, 2005). However, such models are only one-dimensional and the compliance of such phenomenological models to fundamental laws of continuum mechanics and laws of thermodynamics is questionable. In this regard, the work that by Dunn and Fosdick (1974) on the Rivlin–Ericksen fluid model of second grade is worth mentioning. Prior to their work, based on many plausible arguments from experimental observations, the coefficient of the first Rivlin–Ericksen tensor (α_1) in the model was postulated to be always greater than zero. However, based on thermodynamic considerations, Dunn and Fosdick (1974) demonstrated that this condition leads to instabilities even in simple shearing flows such as the flow between parallel plates; and for certain plate separation distances, it was shown that the flow does not even exist. They also demonstrated the instabilities in arbitrary flows inside rigid and fixed cylinders when using the model with the condition $\alpha_1 > 0$. For such a case, unless the velocity field is severely restricted, the flow evolves such that the average stretching in the material exponentially increases to infinity. The study by Dunn and Fosdick (1974) clearly points out the importance of thermodynamic considerations while developing models and the likely consequences when these requirements are not met.

For applications like 3D printing, accurate rheological models can be useful in predicting the vertical collapse height or the deformation occurring during the printing process. For this, a complete three-dimensional model needs to be developed that also complies with the requirements of thermodynamics.

2.2.4 A thermodynamic-based approach for modelling

One possible approach that has not yet been employed to describe the rheology of cement paste is by using a framework of multiple natural configurations. Such an approach has proven to be useful in developing a wide range of constitutive models, some noteworthy examples being the work by Rajagopal and Srinivasa (2000) to model rate type fluids, models for classical plasticity (Srinivasa, 2001; Rajagopal and Srinivasa, 2004*a*), twinning (Rajagopal and Srinivasa, 1997, 2004*b*), systems undergoing chemical reactions (Kannan and Rajagopal, 2011), polymer crystallization (Rao and Rajagopal, 2002), alloys with shape memory (Rajagopal and Srinivasa, 1999, 2004*b*), and mixtures of fluids (Málek and Rajagopal, 2008). In this approach, it is assumed that a body in the current configuration at time t, upon the removal of the external forces or stimuli, instantaneously takes a stress-free configuration, which is called as the natural configuration. The inelastic response of materials is described through the evolution of the natural configuration with the deformation of the material.

The notion of natural configurations is regularly used alongside with the principle of maximization of rate of dissipation. In this approach, a functional form is assumed for the Helmholtz potential that involves the relationships between the natural configuration, the current configuration, and the reference configuration. The rate of dissipation is also given a functional form involving the time-dependent changes to the natural configuration. The constitutive equations are obtained by maximizing the rate of dissipation over all allowable processes, with a reduced form of the second law of thermodynamics as a constraint.

This framework was extended by de Souza Mendes *et al.* (2013) to include a structural parameter so that thixotropic behavior can be described. In their approach, the stored energy function was considered to be a function of both a stretch tensor and a structural parameter while the rate of dissipation function was considered to be functions of the time derivative of the structural parameter, in addition to other kinematic quantities. Constitutive equations can again be obtained by maximization of the rate of dissipation.

In summary, using the multiple natural configurations framework together with the maximum rate of dissipation criterion, three-dimensional rheological models that meet the requirements of thermodynamics can be developed. The possibility of using this approach for cementitious systems needs to be investigated.

2.3 Mixture design of 3D printable concrete

The various additives and admixtures used in the design of printable concrete are discussed in this section. Some of the earliest attempts to extrude cementitious materials were by using composites with high fiber content (Shao *et al.*, 1995; Shao and Shah, 1996). Rheological modifiers like methyl cellulose or calcined clay were found necessary for a successful extrusion (Srinivasan *et al.*, 1999; Kuder and Shah, 2007).

The load carrying capacity of cementitious materials in the fresh state is called the green strength. Tregger *et al.* (2010) studied the effect of calcined clay, fly ash and high-range water-reducing admixture (HRWA) on the green strength of cement paste. Green strength was determined from the load carrying capacity of cylindrical specimens of equivalent concrete derived from the cement paste. The loading was done by pouring sand on top of a bucket placed on top of the freshly demoulded cylindrical specimens until the failure of the specimen (see Figure 2.5). Calcined clay increased the green strength while both HRWA and fly ash caused a decrease in the green strength. Further, shear and compression yield stress were determined for each mix. The shear yield stress was determined by using a strain controlled shear rheometer fitted with a co-axial geometry while compression yield stress was determined by the centrifuge method (Buscall and White, 1987). Both the shear and compression yield stress increased with calcined clay addition while they decreased with fly ash and HRWA additions. Peled *et al.* (2000) studied the effect of fly ash on the rheology of extrudable fiber composites. The ram pressure vs piston movement was plotted for mixtures with varying levels of fly ash. For acrylic and polyvinyl alcohol fibers, the addition of fly ash led to a decrease in the extrusion pressure. For glass fibers, the extrusion pressure did not change with fly ash addition while for cellulose fibers, the fly ash addition increased the extrusion pressure. Voigt *et al.* (2010) studied the effect of fly ash and calcined clay on flowability and shape stability. Flowability was determined from flow table test while shape stability was assessed from green strength determined from load carrying capacity of cylindrical specimens. The addition of fly ash improved flowability, but reduced the shape stability of the fresh mixture. The addition of calcined clays, on the other hand, improved shape stability but caused a slight to moderate decrease in flowability, depending on the type of the calcined clay used. Hence, from a rheological point of view, the combined addition of fly ash and calcined clay was proven to be beneficial. It produced a mixture with good flowability and also with the required shape stability.

Another important aspect for printable mixtures is the structural build-up due to thixotropy and cement hydration. Compared to plain cement mixtures, the rate of rebuilding under shear induced breakdown was found to be higher in cement mixtures containing calcined clay. However, with longer resting time, this effect diminished due to hydration effects (Kawashima *et al.*, 2013). Quanji *et al.* (2014) studied the effect of attapulgite clay on thixotropy and the rate of cement hydration. The thixotropy was assessed as the area enclosed between 20-80 s^{-1} strain rate in a hysteresis loop test (see Figure 2.6). Isothermal calorimetry was used to determine the rate of cement hydration. Both rate of hydration and the area enclosed in the hysteresis loop increased with nanoclay addition. Similar effects on cement hydration were observed by Heikal and Ibrahim (2016), who showed that the initial and final setting times of cement paste reduce with the addition of nanoclay. Qian and De Schutter (2018) showed that the addition of attapulgite clay increased the dynamic yield stress, thixotropic index and the size of flocs formed in fresh cement paste. The dynamic yield stress was determined by fitting the equilibrium flow curve with a Bingham model. The thixotropic index was assessed based on the stress decay in a steady shear experiment (see Figure 2.7). The thixotropic index was defined as the ratio between the stress corresponding to the initial torque value divided by the stress corresponding to the equilibrium torque value. The chord length of the agglomerated cement particles was determined using the chord length distribution of particles/agglomerates in fresh cement paste are determined using focused beam reflectance measurement (FBRM). From Figure 2.8, it can be seen that the distribution curve of the chord length shifts towards the left with increasing attapulgite clay content. This indicates larger agglomerates are formed with an increase in the nanoclay content.

Figure 2.5: Green strength test (taken from Tregger *et al.* (2010))

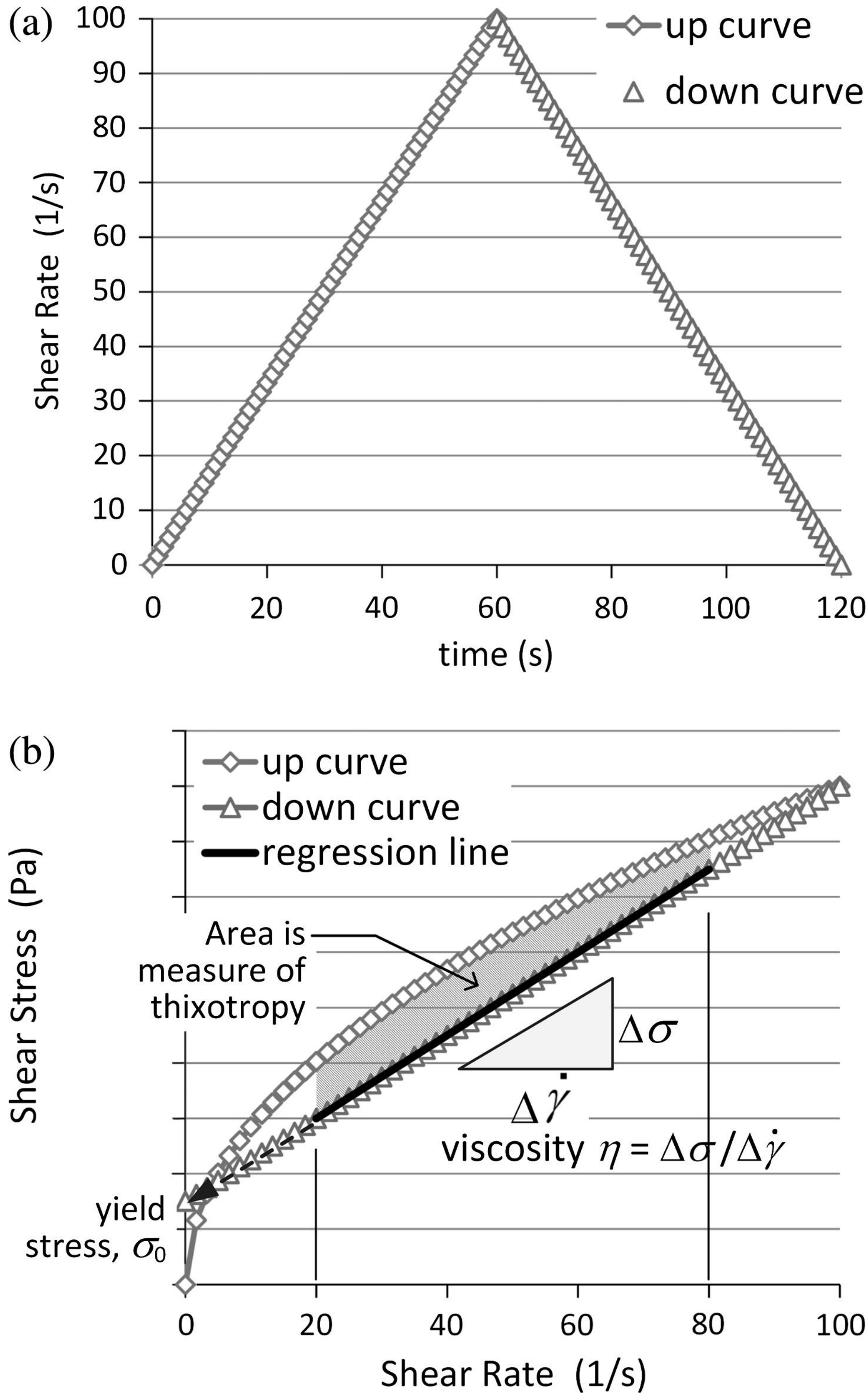

Figure 2.6: Assessment of thixotropy from the hysteresis loop test by Quanji *et al.* (2014)

There is only limited literature on the effect of viscosity modifying agents (such as cellulose based products) on thixotropy of cement paste. Assaad *et al.* (2003) showed that the addition of polysaccharide based polymers increased the thixotropy of SCC. To assess thixotropy, the concrete was tested at constant rotational speeds using a concrete rheometer. The torque was found to overshoot to reach an initial maximum value and then tended towards an equilibrium value. Two indices were used to assess the thixotropy. One of the indices was the difference between the initial and the equilibrium torque values divided by the equilibrium torque value. The initial and equilibrium torque values were determined for different constant rotational speeds to obtain initial and equilibrium torques versus rotational speed plots respectively. The area comprised between these plots was taken as another index for measuring thixotropy. Both indices were found to be higher in concrete containing polysaccharide. Knapen and Van Gemert (2009) used isothermal calorimetry and Fourier transform infrared spectroscopy to study the effect of different cellulose ether based polymers on cement hydration. It was found that the addition of these polymers increased the dormant period of cement hydration. A lower value of maximum heat and broader peaks were observed in the mixes containing these polymers.

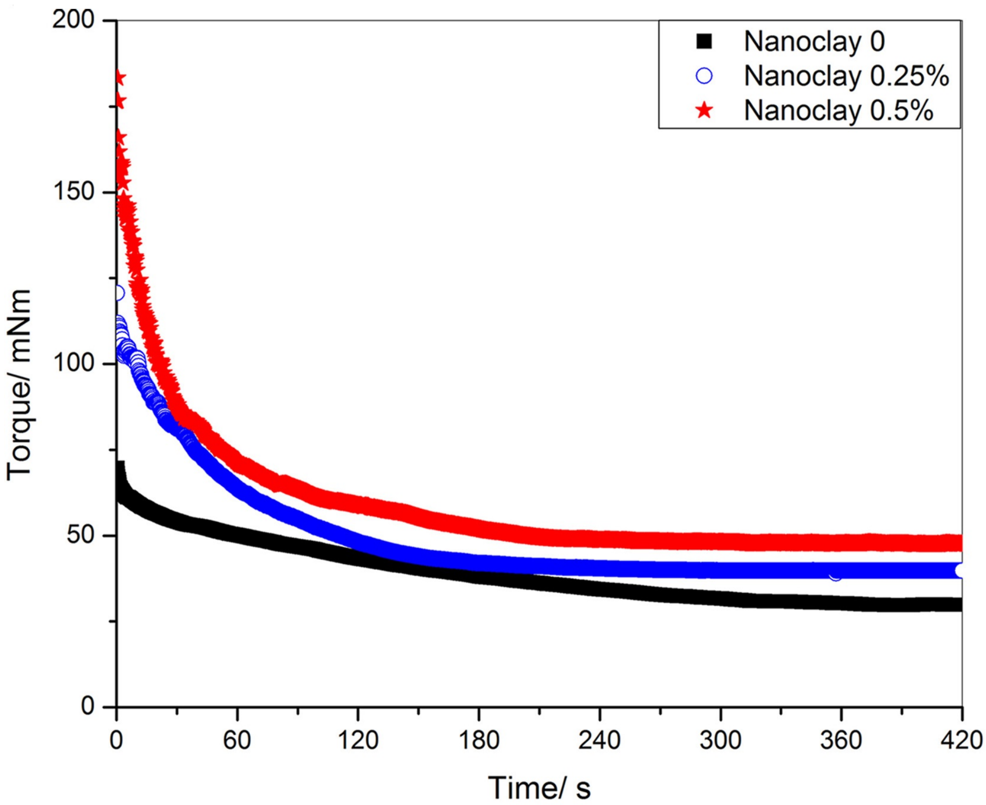

Figure 2.7: Stress decay in steady shear experiments with cement pastes having different attapulgite clay content (Qian and De Schutter, 2018)

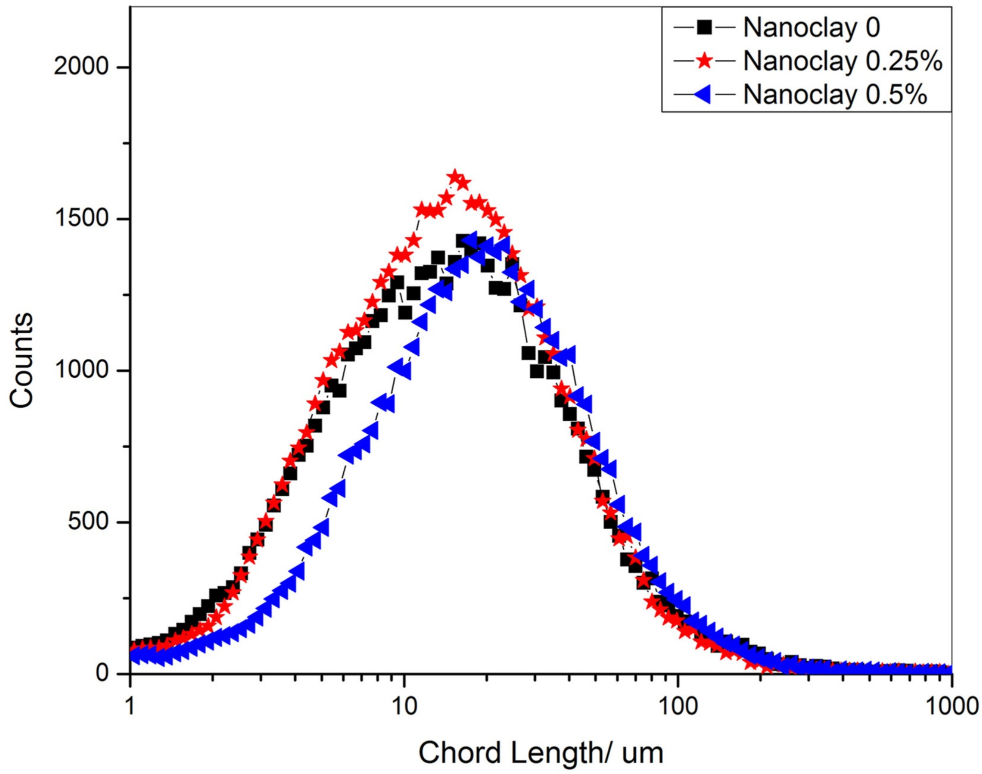

Figure 2.8: Chord length distribution of cement pastes having different attapulgite clay content determined by FBRM (Quanji *et al.*, 2014)

Researchers have proposed different parameters which can be used to assess the fresh properties of printable concrete. For instance in the work done by Le *et al.* (2012*a*), extrudability, workability, open time and buildability were identified as the four essential parameters for characterizing printable concrete. The ability to extrude through a 9 mm diameter nozzle was defined as extrudability. It was evaluated by extruding filaments of 300 mm length and visually checking for blockages and fractures (see Figure 2.9a). The workability was assessed by determining shear strength of the mixture using a vane shear apparatus. The duration of time for which the concrete had sufficient workability was called the open time, and this was assessed by determining the change in shear strength with respect to time. The ability to retain shape once extruded was called buildability. The number of concrete layers that could be built without noticeable deformation of the lower layers was used to assess the buildability of the mix (see Figure 2.9b).

Kazemian *et al.* (2017) used print quality, shape stability and printability window as the main parameters to evaluate the concrete mixtures. Print quality, in turn, was assessed in terms of surface quality, squared edges, dimensional conformity and dimensional consistency. Two test methods, layer settlement and cylinder stability, were proposed to assess the shape stability of the mixtures. In the first method, two concrete layers were printed. Photos taken before and after the printing of the second layer were analyzed in an image analysis software to determine the spread in the first layer. In the second method, fresh cylindrical specimens were subjected to a load of 5.5 kg, and the resulting change in height was determined. Finally, printability window was evaluated by determining (i) printability limit and (ii) blockage limit of the concrete mixtures. The printability limit is the time duration up to which a concrete mixture can be printed with acceptable print quality. Blockage limit, on the other hand, is the time duration up to which a concrete mixture can be extruded without causing blockage in the pump, or damage to the nozzle. From the study of various mixture combinations, it was concluded that the addition of silica fume and highly-purified attapulgite clay leads to improvement in the shape stability of the printed layers. The addition of polypropylene fiber was found to provide a slight enhancement in shape stability.

(a) (b)

Figure 2.9: (a) Extrudability and (b) buildability test for assessment of 3D printable concrete by Le *et al.* (2012*a*)

Using similar tests methods to that used by Le *et al.* (2012*a*) and Kazemian *et al.* (2017), other researchers (Paul *et al.*, 2018; Ma *et al.*, 2018) have also developed 3D printable concrete formulations from trials conducted using laboratory-scale test bed printers. Based on the rheological requirements for 3D printing, there is a need to develop a more systematic procedure for its mix design, i.e, the mix proportion parameters like the dosage of superplasticizer must be linked with the test methods such as extrudability and buildability.

2.4 Assessment of phase separation

With regard to the extrusion of cementitious materials, another aspect that warrants discussion is the occurrence of phase separation in cementitious systems when subjected to high extrusion pressure. Srinivasan *et al.* (1999) monitored the pressure versus time data during ram extrusion and found that when phase separation occurred, there was a sudden abrupt increase in the pressure. In such cases, the liquid phase separated out leaving behind a dry unextrudable mass in the extruder. Also, they showed that the addition of HPMC helped in reducing this sudden abrupt increase in pressure (see Figure 2.10a) while the addition of polyethylene glycol (PEG) resulted in reducing the die-wall stress, i.e., the resistance to flow at the junction between the die wall and the extruding material (Figure 2.10b). Later, Kuder and Shah (2007) used a similar approach and found that the addition of calcined clay was beneficial in controlling the liquid phase migration during extrusion. Although this method of monitoring the pressure in ram extruder helps to identify the occurrence or to determine the dosage of additives required to control phase migration, it does not provide any material parameter that characterizes the water retention capability of the mix.

Water retention characteristics of cement mortars are usually assessed by using various empirical test methods. For instance, in the ASTM method (ASTM C1741-18, 2018), a sample of mortar is placed in a bleed cell and then subjected to constant pressure. The amount of bleed water that separates out from the cell is used as a measure of its lack of water retention capability. Similar empirical methods based on the amount of bleed water have been used by various other researchers as well (Khayat *et al.*, 1999; Saric-Coric *et al.*, 2003; Patural *et al.*, 2011; Govin *et al.*, 2016). However, the problem with such methods is that they are single-point measurements that do not give any fundamental material parameters that can be related to water retention.

Realizing this, Green *et al.* (1999) adopting ideas from soil mechanics, suggested the use of desorptivity as a fundamental material parameter in characterizing water retention of lime mortars. They showed that when a constant pressure is applied to a column of wet mortar, the cumulative height of bleed water from the column is proportional to the square root of time for which the pressure is applied (see Figure 2.11a). This constant of proportionality is called the desorptivity. Green *et al.* (1999) also showed that the desorptivity at a given pressure can be decreased by the addition of methyl cellulose (see Figure 2.11b).

The beneficial effects of cellulose-based admixtures in improving water retention capability of cement-based materials have been pointed in many studies (Khayat *et al.*, 1999; Saric-Coric *et al.*, 2003; Zhou *et al.*, 2019). The addition of such admixtures causes an increase in the viscosity of the liquid phase (Khayat, 1998; Bülichen *et al.*, 2012; Brumaud *et al.*, 2013). The working mechanism of these admixtures depends on the dosage. At low dosages, it causes swelling by intramolecular sorption of water. But as the dosage increases above a certain level called the overlapping concentration, the molecules start to agglomerate in the pore solution and form networks of hydrocolloidal gels. These gels fill the pore spaces and provide less space for the water to migrate out from the granular skeleton (Bülichen *et al.*, 2012; Brumaud *et al.*, 2013). At this stage, the amount of colloidal gels that form has been found to depend on the amount of sulphate ions that are present in the pore solution (Bülichen and Plank, 2013). Pore solution with higher sulphate ion concentration hinders the gel formation thereby reducing water retention capacity of methyl cellulose. For instance, gypsum plaster has a relatively higher amount of sulphate ion concentration in the pore solution as compared to cement paste. As a result, gypsum plaster requires a much higher amount of methyl cellulose as compared to cement paste for achieving the same water retention (Bülichen and Plank, 2013).

In summary, the foregoing discussions suggest that the liquid phase migration can be critical in an extrusion process and there is a need to study the water retention capacity of cementitious materials to be used for such applications. Further, the study by Green *et al.* (1999) on lime mortars indicates that desorptivity can be a fundamental parameter for assessing water retention. The possibility of extending this approach for assessing the phase separation in extrudable mortars needs to be investigated.

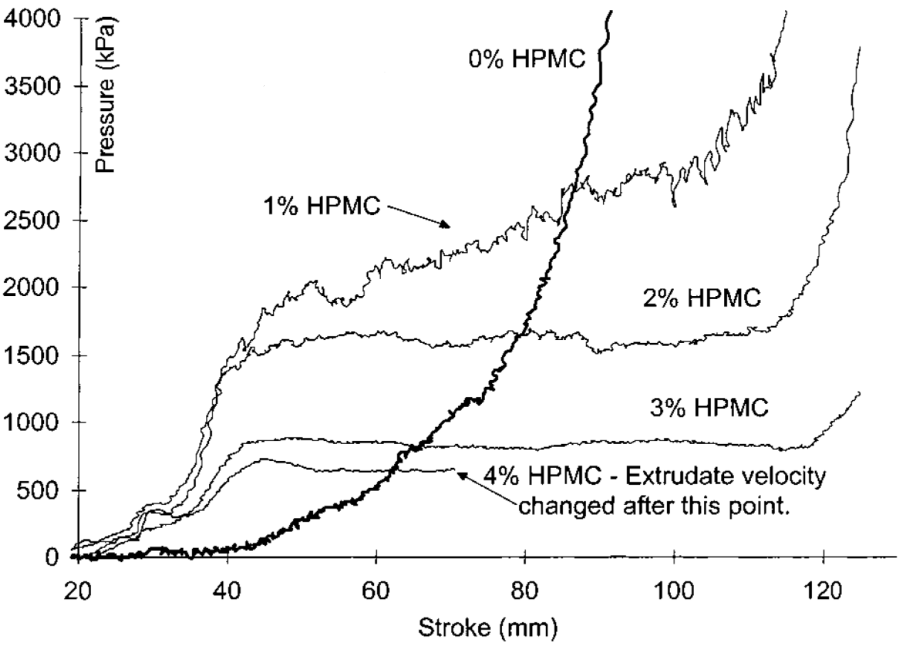

(a)

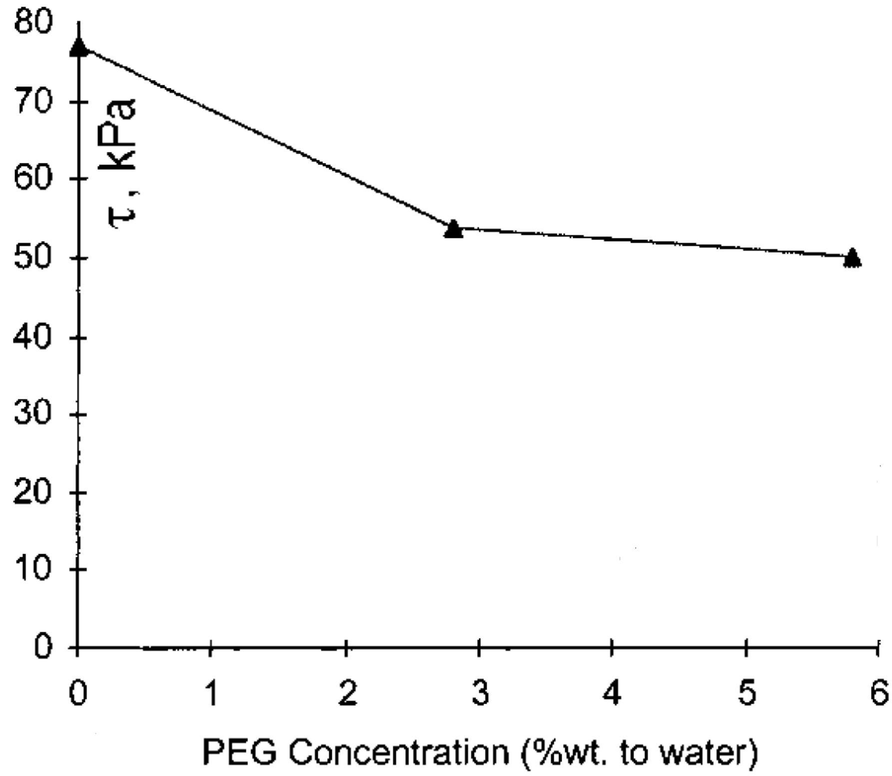

(b)

Figure 2.10: (a) Effect of HPMC in reducing the abrupt increase in extrusion pressure and (b) Effect of PEG in reducing the die-wall friction during extrusion pressure (taken from Srinivasan *et al.* (1999))

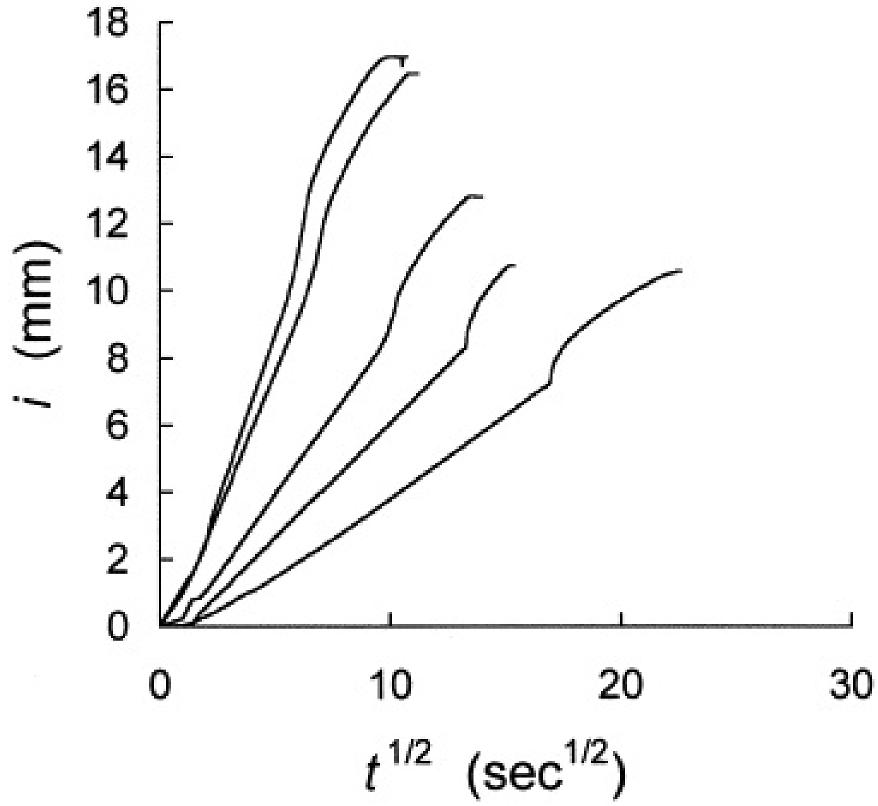

(a)

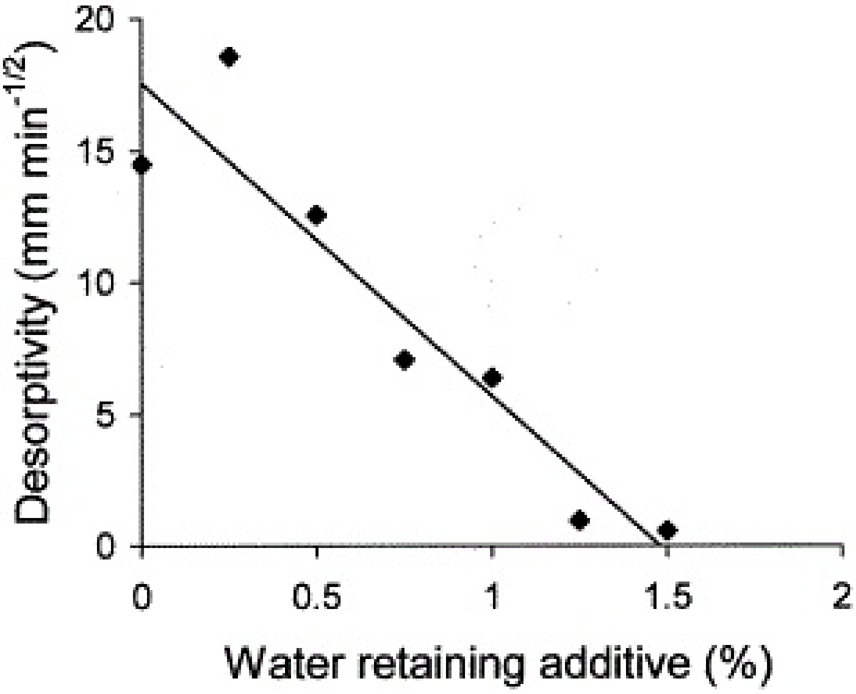

(b)

Figure 2.11: (a) Height of cumulative bleed water column versus the square root of time for pressure values of 0.03 (lower line), 0.07, 0.13, 0.33, and 0.5 (upper line) MPa (b) Effect of methylcellulose on desorptivity at a pressure of 0.33 MPa (taken from Green *et al.* (1999))

2.5 Mechanical properties of 3D printable concrete

Prior to the beginning of research on 3D printed concrete, there were studies on the mechanical behaviour of extruded cement-fiber composites. For instance, Takashima *et al.* (2003) showed that the flexural strength of cement composites with polypropylene fibers made by extrusion process was higher than that obtained when the same composite was made by conventional mould casting. The strength increase was attributed to two reasons. Firstly, it was observed though scanning electron microscope images that there is a higher alignment of the polypropylene fibers along the extruding direction. Secondly, the authors also reported that the extruded composites had a higher density as compared to the composites made by mould casting. Similar observations were also made in the study by Khelifi *et al.* (2016) on cement composites containing flax fibers. They determined the splitting tensile strength of the both cast and extruded composites (see Figure 2.12). The extruded composites showed higher splitting strength as compared to the composites made by conventional casting.

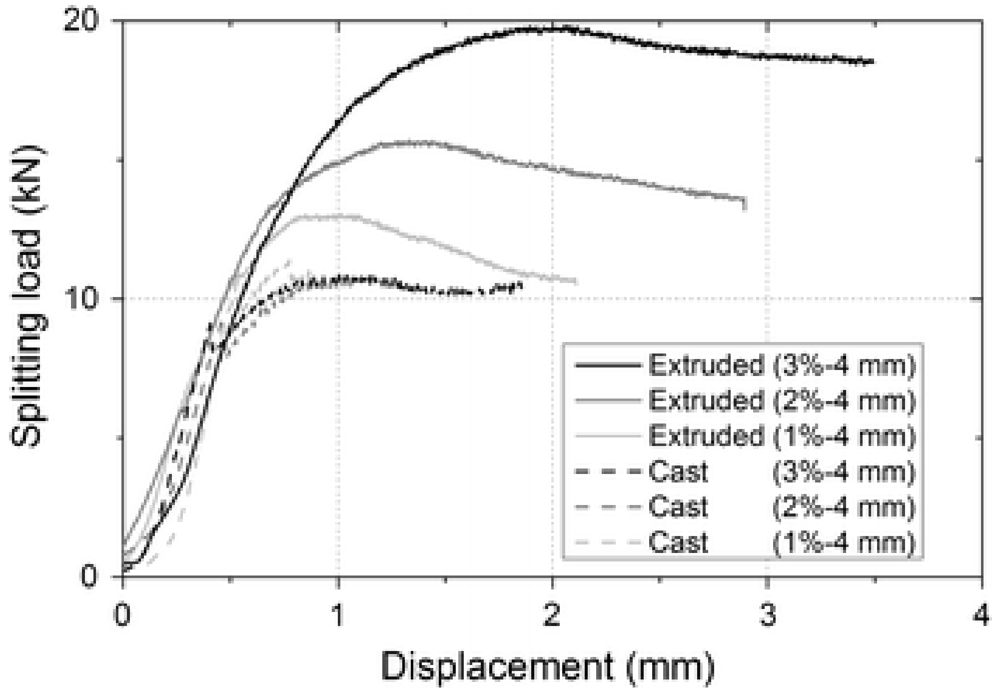

Figure 2.12: Split tensile strength of extruded and cast cement composites with flax fibers (taken from Khelifi *et al.* (2016))

One of earlier studies on the mechanical behaviour of 3D printable concrete was by Le *et al.* (2012*b*). They showed that 3D printable concrete elements can be anisotropic.

In the study, compressive and flexural strengths were evaluated in different loading directions and compared with that of the mould cast specimens. The specimens for testing were extracted from a 3D printed slab and a curve-shaped 3D printed bench. The mould cast specimens had high compressive and flexural strengths of about 107 N/mm^2 and 11 N/mm^2 respectively. On the other hand, the compressive and flexural strengths of printed specimens were lower and varied from 91 to 102 N/mm^2 and 6 to 17 N/mm^2 respectively, depending on the loading direction. Panda *et al.* (2017*a*) also observed similar results when comparing the compressive and flexural strengths of 3D printed and mould cast geopolymer concrete. A 15 $\times$ 7 mm rectangular nozzle was used in their study. Apart from this, a few other researchers have also reported anisotropic behaviour for printed concrete elements (Nerella *et al.*, 2016; Panda *et al.*, 2017*b*; Paul *et al.*, 2018). Le *et al.* (2012*b*) also observed the presence of voids at the junction between four filaments when circular nozzle was used (see Figure 2.13). The voids were more predominant in the case of poorly printed specimens. The number and size of the voids were considerably reduced in the case of well printed specimens having a higher dosage of superplasticizer. The well printed specimens were found to have a higher density as compared to mould cast specimens. The reason for this higher density is not well understood. It may because of the higher compaction and packing density achieved during the extrusion of the printed elements.

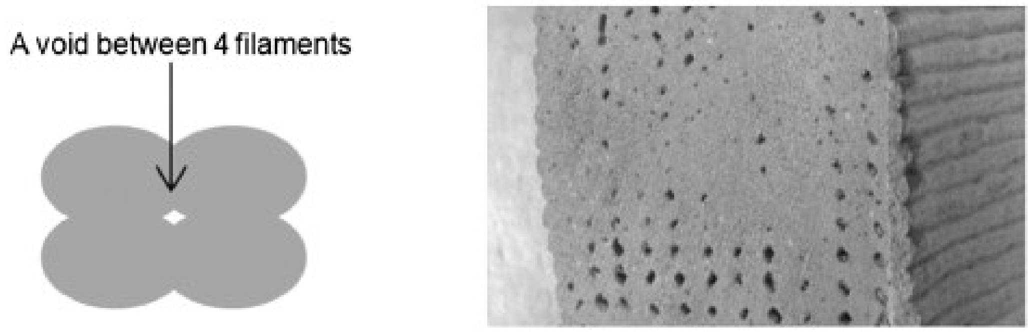

Figure 2.13: Presence of voids between the junction of four filaments when a circular nozzle is used for printing (taken from Le *et al.* (2012*b*))

Contrary to the results obtained by Le *et al.* (2012*b*), Nerella *et al.* (2016) found that the compressive strength of printed specimens was higher by about 10 % as compared to mould cast specimens when tested along certain directions. These contradictions in the results indicate that the mechanical properties would also be dependant on the type of mix used, the printer system and the print parameters used in a particular study. For instance, Panda *et al.* (2018) showed that the tensile bond strength can depend on the print parameters such as time gap between two successive layers, print speed and the height from which the nozzle is depositing the layer. It was found that the bond strength decreased with increasing time gap between layers. Further, the increase in print speed or the height of the nozzle from the deposited layer also led to the decrease in the tensile bond strength (see Figure 2.14). The decrease in tensile bond strength with increased time gap was also observed by a few other researchers (Le *et al.*, 2012*b*; Panda *et al.*, 2017*a*).

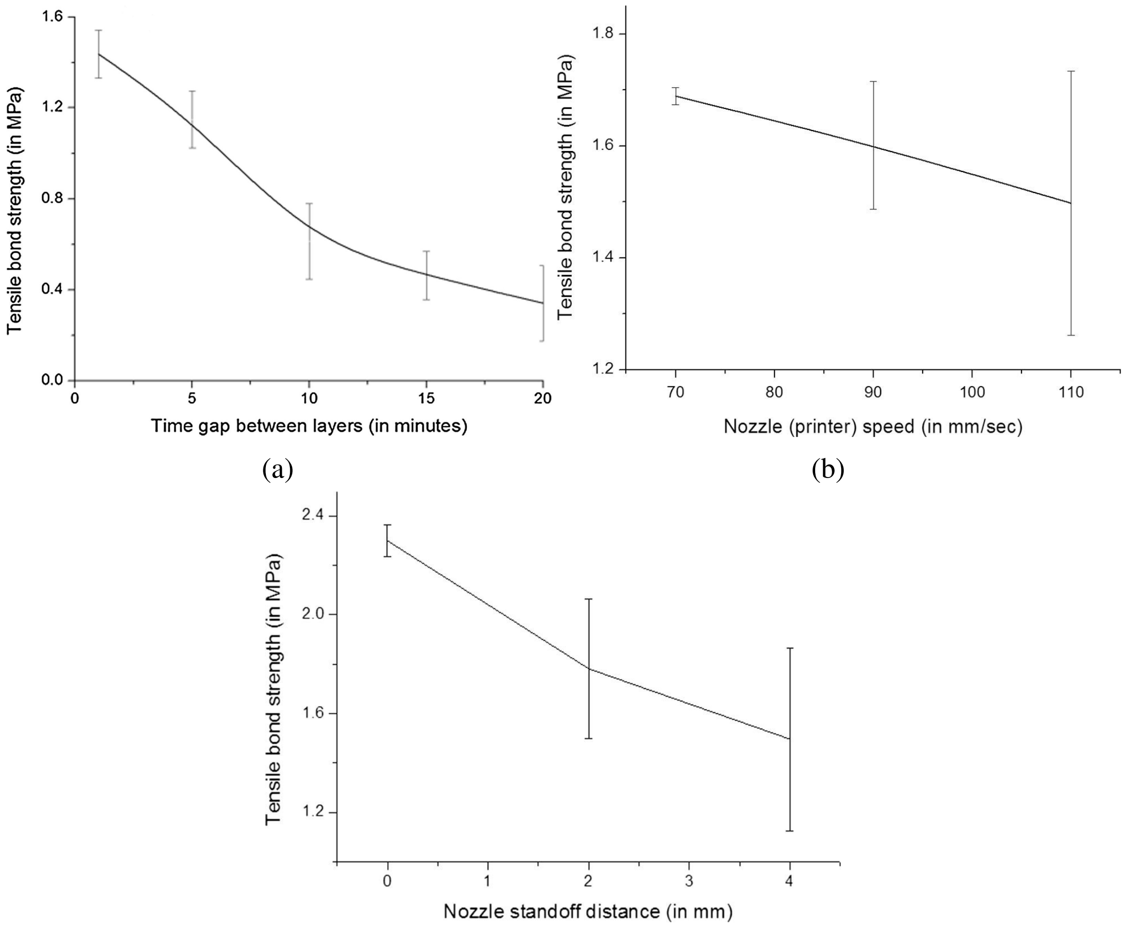

(a) (b) (c)

Figure 2.14: Effect of (a) time gap between layers (b) print speed and (b) height of the nozzle from top of first layer on tensile bond strength of 3D printed elements (taken from Panda *et al.* (2018))

Some of the recent studies have shown that the ambient conditions during printing can also have an effect on the bond strength between layers. For instance, Roussel (2018*a*) measured the interface strength when the layers were protected from drying and also when exposed to drying. It was found that the interface strength reduced by even up to 50 % when the printed layers were exposed to drying. Similar observations were also made in the study by Sanjayan *et al.* (2018). They showed that the bond strength was found to depend on the surface moisture content at the interface between the layers. The removal of surface moisture due to evaporation caused a reduction in the bond strength.

2.6 Need for research

As seen in the literature review on the mixture proportioning of 3D printable concrete, its mixture design has been mostly based on a trial and error method. Also, many studies refer to the use of special additives like nanoclay, viscosity modifying agents (VMA) and micro-silica. Based on a more fundamental understanding, a systematic procedure has to be developed for the mixture design of 3D printable concrete. The test methods for extrudability and buildability must be linked with the mixture proportion parameters such as the dosage of superplasticizer. Further, the influence of special additives such as nanoclay, VMA and micro-silica need to be examined in detail.

Most of the studies on extrusion-based 3D printing found in the literature have been based on small laboratory-based printer systems. The issues that may arise in scaling-up to larger 3D printer system need to be studied. The high pressure applied in larger printer systems may cause the concrete mix to become unstable, i.e., the high pressure may cause the liquid phase in it to separate out, leading to blockages during extrusion. There is a need to gain a fundamental understanding on how water drainage occurs during such high pressure extrusion process.

Further, 3D printable concrete in the existing literature are mortars having only fine aggregates with nominal size usually less than 2.36 mm. Therefore, there is a need to develop 3D printable concrete with coarse aggregates. For this, an understanding is required on how the coarse aggregate may affect the extrudability as well as the stability of the printed layers.

The mechanical properties of 3D printed specimens are quite different when compared to that of mould cast specimens. These differences may be attributed to two reasons. First, the introduction of interfaces due to layer-wise extrusion. Secondly, the properties of the bulk concrete itself may vary. For instance, there are studies that suggest a comparatively higher density for concretes cast through the extrusion process. Therefore, a less porous and stronger bulk concrete may exist in 3D printed elements. But to validate this hypothesis, a detailed study on the mechanical response as well the porosity assessment of the 3D printed concrete elements is required.

Although the mixture development of 3D printable concrete is carried out based on empirical methods, the importance of rheological studies cannot be overlooked. Using rheological models, prediction of failure height and the deformation of layers during printing can be carried out. However, the existing rheological models have many shortcomings which were discussed in Section 2.2.3. On the other hand, the robust thermodynamics-based approach presented in Section 2.2.4 has been useful in developing models for a wide range of materials. The possibility of using this approach in developing a complete three-dimensional model suitable for cementitious systems needs to be examined.

CHAPTER 3

MIX DEVELOPMENT FOR SMALL-SCALE 3D PRINTER SYSTEM

3.1 Introduction

For a successful extrusion process, the material must be flowable enough so that it can be extruded through the nozzle. But once the layer is extruded, it must have sufficient shear strength to resist deformation due to its self weight and the weight of the layers printed above it. From a rheological perspective, the material must be liquid-like with a low viscosity while inside the pump and nozzle, but once extruded out it must undergo a transition to a solid-like behaviour with enough strength to resist deformation. Based on the material, different strategies can be used for achieving this. For instance, in 3D printing of polymers (e.g. polylactic acid), this is achieved by a sudden change in temperature. While inside the nozzle, the polymer filament is heated to above its melting point, allowing it to flow through the nozzle. But once extruded, it is rapidly cooled causing a transition to a solid-like behaviour (Kirchmajer and Gorkin III, 2015). For concrete and other yield stress fluids, the underlying principle is quite different. The pump exerts enough pressure to exceed the yield stress of the material, causing it to flow and extrude through the nozzle. Once extruded, the high yield stress (which should be higher than the stress due to self weight) allows the material to resist deformation and prevent flow in the material. Further, as pointed out in Chapter 2, the yield stress of the cementitious systems increases with time due to the structural build-up associated with thixotropy and cement hydration. This increase in yield stress allows more layers to be deposited over time.

Therefore, yield stress becomes the most important parameter for mixture design. A high yield stress is essential to prevent deformation of extruded layers. On the other hand, if the yield stress and plastic viscosity become too high such that they exceed the capability of the pump, then extrusion of the material becomes difficult. Therefore, there is an optimum range of yield stress in which the material is both extrudable and buildable. In this chapter, a yield stress-based mixture design approach is developed for 3D printable concrete based on the experiments conducted on a small laboratory-scale concrete 3D printer. Further, tests methods for extrudability, buildability, robustness and the assessment of structural build-up are discussed.

3.2 Materials and methods

For the current study, portland cement (conforming to IS 12269 (2013)), Class F fly ash (conforming to ASTM C618-17a (2017)) and silica fume (conforming to ASTM C1240-15 (2017)) were used as the binders. Their specific gravities are 3.15, 2.6 and 2.2 respectively and their oxide composition is shown in Table 3.1. The chemical admixtures used were PCE based superplasticizer and methylcellulose-based VMA. The superplasticizer was used in the liquid form (solids content of 34 %) and the VMA was used in a powder form. In addition, polypropylene fibers having length of 12 mm and thickness of 40 microns were used. The use of nanoclay has proven to beneficial in terms of imparting shape stability for the extruded elements (Voigt *et al.*, 2010; Kazemian *et al.*, 2017). A commercial form of purified palygorskite was used as a rheological modifier. The clay particles in this material have an average size of 1.5-2 μm and specific gravity of 2.29. Its oxide composition is shown in Table 3.1. The fine aggregate used consisted of quartz powder and two grades of quartz sand (designated as sand 1 and sand 2). The specific gravities of the aggregates were 2.76, 2.68 and 2.64 respectively. The particle size distributions of all the granular materials are shown in Figure 3.1. The particle size distributions for portland cement, fly ash and quartz powder were determined by laser diffraction. Since it was not possible to disperse the densified silica fume by ultrasonication done prior to laser diffraction, the particle size distribution for silica fume was taken as that given by the manufacturer. The particle size distributions for the two quartz sands were determined by sieve analysis.

3.2.1 Mixing procedure

The mixing was done by using a Hobart planetary type mixer. At first, the water along with the superplasticizer was added to the mixing bowl. With the blade rotating at a low speed, the pre-blended dry ingredients were slowly added in about 2-3 minutes time. For mixtures containing VMA, the mixing was stopped after 5 minutes, VMA in the powder form was slowly sprinkled over the mixture, then mixing was resumed. For nanoclay mixtures, a part of the mixing water, (about 15 %) was held back. The nanoclay was then dispersed in this water by using a hand held high shear blender. The suspension was introduced into the mixer after 5 minutes. Thereafter, the blades were rotated at a speed of 365 rotations per minute (RPM) for a duration of 25 minutes. The approximate volume of concrete prepared in each batch was 6 litres.

Table 3.1: Chemical composition of cement, fly ash, silica fume and nanoclay (purified palygorskite) used in the study

Chemical composition	Quanitiy (% by mass)			
	portland cement	Fly ash	Silica fume	nanoclay
CaO	64.59	1.28	0.4	1.98
SiO_2	19.01	59.32	96.8	55.2
Al_2O_3	4.17	29.95	-	12.2
Fe_2O_3	3.89	4.32	-	4.05
$(Na_2O)_e$	0.16	0.16	-	0.98
MgO	0.88	0.61	-	8.56
TiO_2	-	-	-	0.49
P_2O_5	-	-	-	0.65
LOI	1.40	-	-	15.66

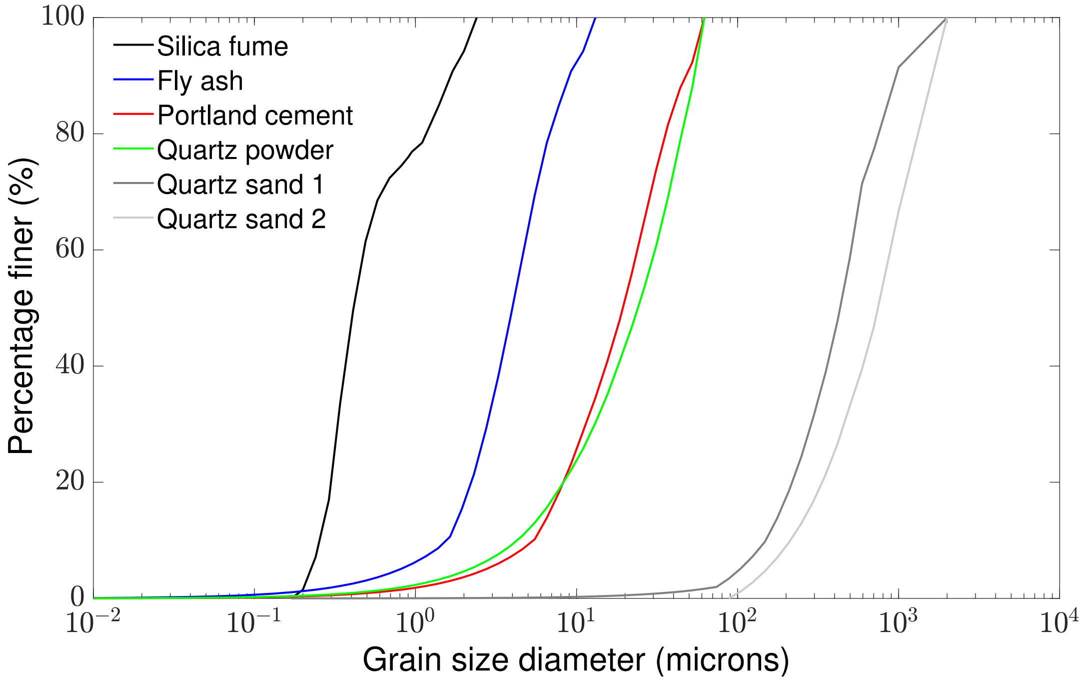

Figure 3.1: Particle size distributions of the materials

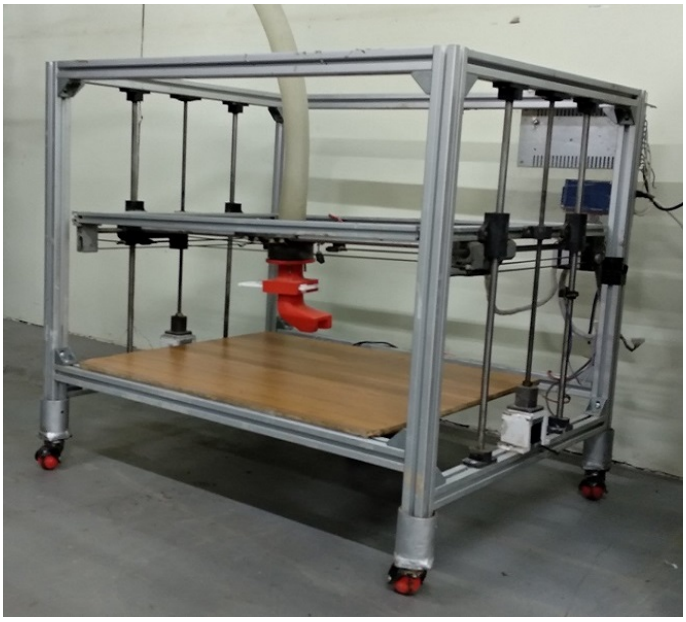

Figure 3.2: Test bed printer

3.2.2 Test bed printer and its calibration

Figure 3.2 shows the small laboratory-scale 3D printer manufactured by the company, Tvasta (Tvasta – Industrial 3D Printing, 2019). The printer has a bed size of 400 × 300 mm, and can print up to a maximum height of 300 mm. Figure 3.3 shows some printed elements made using the printer.

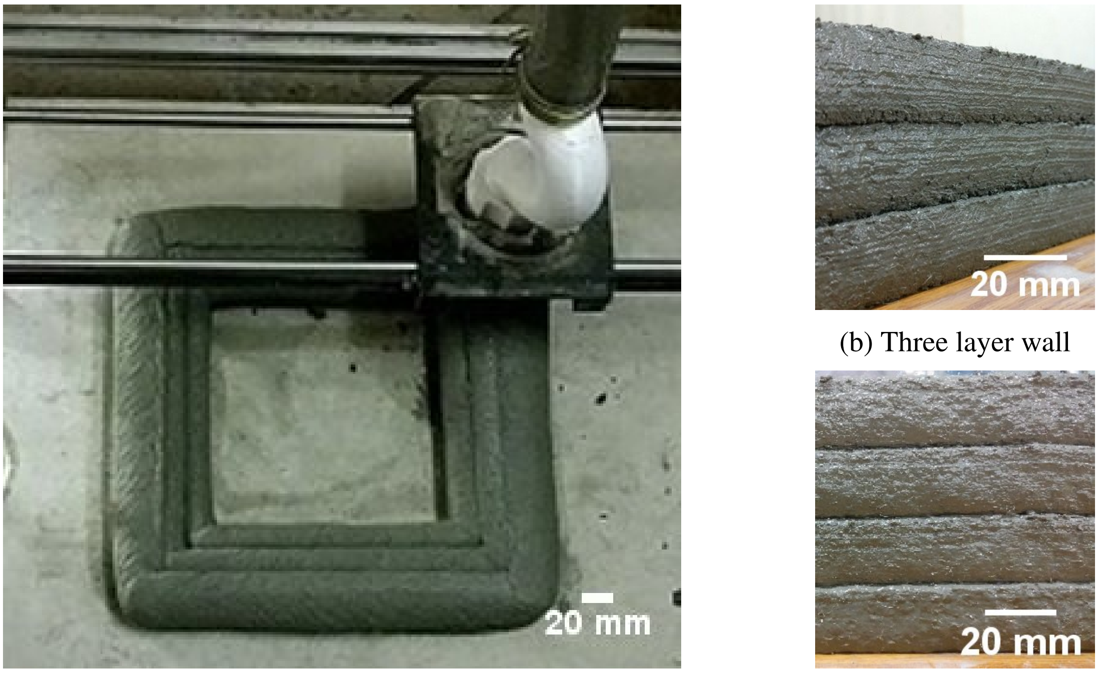

(a) Printing of a square element

(b) Three layer wall

(c) Four layer wall

Figure 3.3: Elements printed using the test bed printer

A schematic diagram showing the different steps in the printing process is shown in Figure 3.4. After the completion of batching and mixing, the material is manually loaded in the feeder system attached to a screw pump. The pump draws the material from the feeder, and transports it to the print head through a flexible hose pipe. The hose pipe has a diameter of 32 mm and length of 1500 mm. The pump is driven by a stepper motor which causes the material to move at a constant displacement rate. Both the pump and the printer are connected to the control system which dictates the printer motion and extrusion speed at the print head. The material is finally extruded through a rectangular nozzle of 30 $\times$ 20 mm size at the print head.

If Q is the discharge rate of the pump, $V1$ is the speed with which the material exits the nozzle (see Figure 3.5), and cross sectional area of the nozzle is $A1$, then the discharge Q is given by

$$Q = V1 \times A1. \tag{3.1}$$

If $V2$ is the print speed, i.e. the speed with which nozzle moves along the print bed (see Figure 3.5), and $A2$ is the cross sectional area of an extruded layer, then the speed $V2$ is given by

$$V2 = \frac{Q}{A2}. \tag{3.2}$$

Substituting from Equation (3.1) in Equation (3.2), it follows

$$V2 = V1\left(\frac{A1}{A2}\right). \tag{3.3}$$

Now, if the extruded element is assumed to have shape stability, then the cross-section of the extruded element will be the same as that of the nozzle ($A1 = A2$). Therefore, Equation (3.1) becomes

$$V2 = V1. \tag{3.4}$$

Therefore, the printer was calibrated such that the print speed ($V1$) was the same as the extrusion speed ($V2$).

For the current study, all the experiments were performed with an extrusion velocity of 44 mm/s. However, it is to be noted that the mixture design is also dependent on the print parameters such as the pump type, extrusion speed, print speed and the shape and dimensions of the nozzle used. Such dependencies are not examined in the current study.

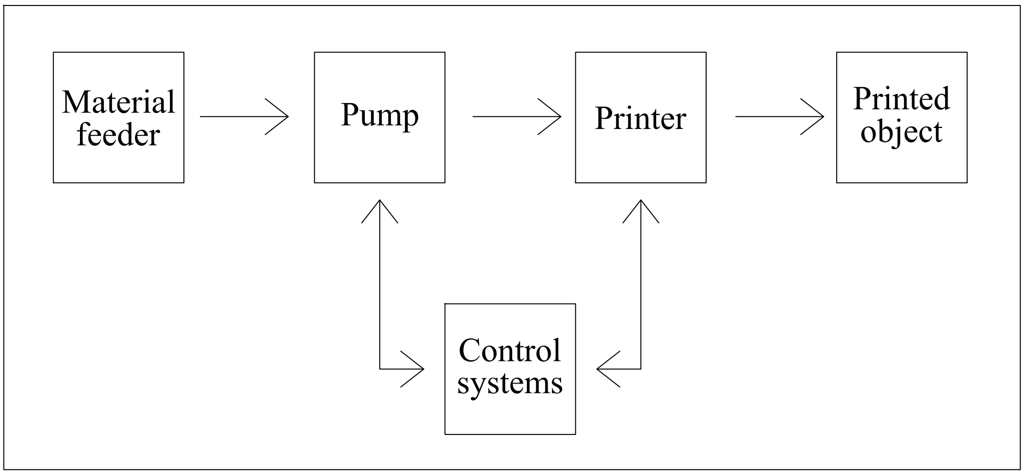

Figure 3.4: Schematic diagram showing the printing process

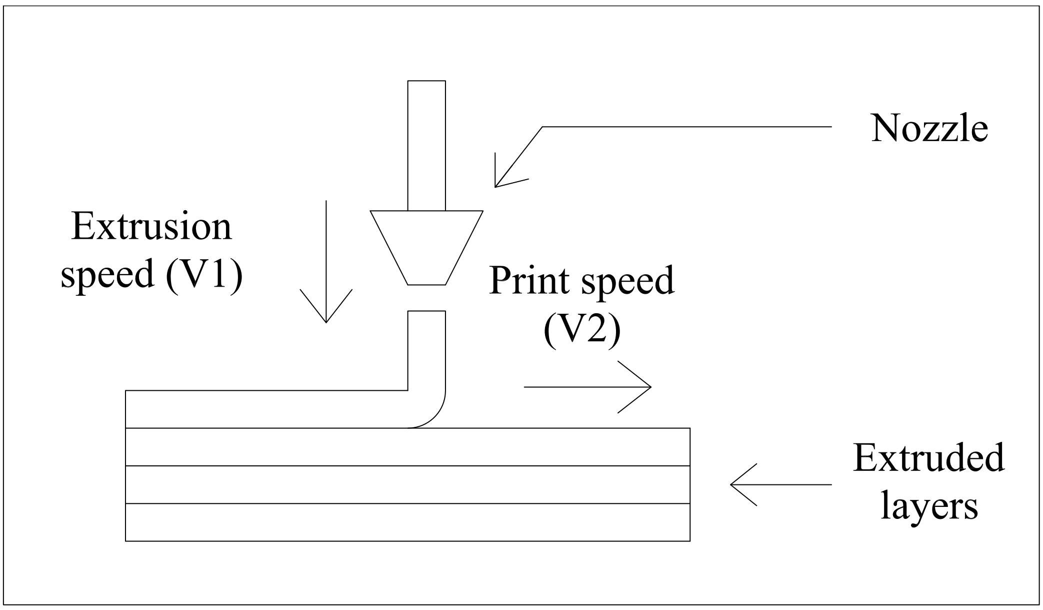

Figure 3.5: Extrusion speed ($V1$) and print speed ($V2$)

3.3 Experimental program

In this section, the test methods used for assessing the mixtures are presented in detail.

3.3.1 Test methods

Extrudability test

Extrudability was defined as the ability to continuously extrude through the nozzle of the printer with the required dimensional conformity and to form layers with good print quality. By good print quality, it is meant that the extruded elements are free of defects such as voids and discontinuity. The print quality of the line was evaluated by visual observation. To perform the test, a 30 cm long single layer was extruded by using the test bed printer. The dimensions of the extruded layer were measured at every 10 cm along the length of the printed line. The test was qualified as 'pass' if (i) the measurements made at all of these locations confirmed to the dimensions of the rectangular nozzle (30 $\times$ 20 mm) within a tolerance of 0.5 mm and, (ii) the printed line was completely free of surface defects such as voids and discontinuity.

Yield stress by vane shear apparatus

Direct measurement of yield stress was done by performing a stress growth experiment using a soil vane shear apparatus. A four-bladed vane with 12 mm diameter and 24 mm height was used. A schematic diagram of the vane apparatus is shown in Figure 3.6. In a stress growth experiment, the material is subjected to a constant strain rate. The maximum torque value was recorded and converted to yield stress by using the equation proposed by Dzuy and Boger (1983) presented below.

$$M = \frac{\pi}{2} D^3 Y \left(\frac{H}{D} + \frac{1}{3} \right), \tag{3.5}$$

where M is the measured maximum torque and Y is the yield stress. H and D are the height and diameter of the vane. To perform the test, the concrete after mixing was immediately transferred to a cylindrical container. The container was 5 cm in diameter and 7.5 cm in height. The vane was inserted into the container such that $H1$ = 3 cm and $H2$ = 2.1 cm (see Figure 3.6). To have the same pre-history, all samples were subjected to a rest duration of 3 minutes before starting the test. The sample was then subjected to a low constant angular velocity of 0.1 RPM and the maximum torque was measured. The choice of a low RPM was made as the conversion equation is valid only for low RPM. At higher RPM, it leads to overestimation of the yield stress (Dzuy and Boger, 1983). Also, it should be noted that the concrete samples are thixotropic and their response is shear-history dependent. Hence, it was important to follow the same protocol for all samples. In each case, the test was repeated with a new sample to ensure reproducibility.

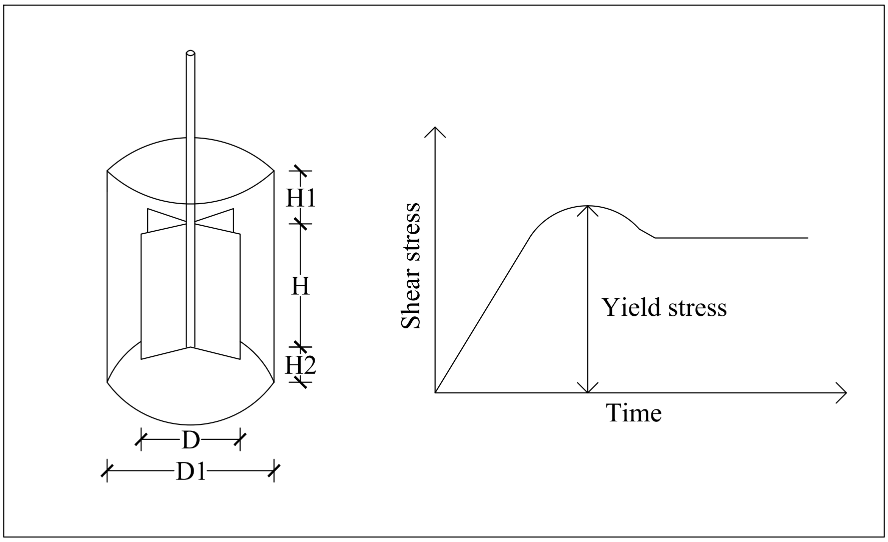

Figure 3.6: Vane shear test

Buildability test

The method proposed by Kazemian *et al.* (2017) was used to assess the buildability of the deposited layers. For performing the tests, two layers of concrete were printed (see Figure 3.7) with a time gap. The compression of the bottom layer after the printing of the second layer was determined. The time gap was decided based on the element to be printed. The objective of the research program at IIT Madras was to develop a layer-wise extrudable mixture for the additive manufacturing of a 1.52 x 1.13 m toilet module. In this case, since there are four horizontal layers with a time gap of two minutes, the time gap for each vertical layer was calculated as eight minutes for a horizontal print speed of 44 mm/s. Hence, the buildability tests were performed with a time gap of eight minutes.

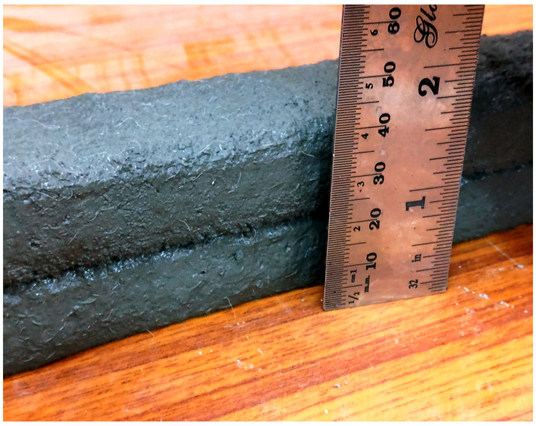

Figure 3.7: Buildability test

Robustness test

For industrial applications, it is important to obtain stable and robust mixture proportions with less variability in yield stress. To quantify robustness, the superplasticizer dosage corresponding to the required yield stress was changed by $\pm 0.01\%$ and $\pm 0.02\%$. The deviation of yield stress from the reference value was expressed by a variability factor, V given by the following equation:-

$$V = \sqrt{\frac{\sum (Y - Y_{ref})^2}{N}}. \tag{3.6}$$

In the above equation, Y_{ref} is the yield stress of the reference mixture. Y is the corresponding yield stress obtained for each variation in superplasticizer dosage, $N = 5$ is the number of samples (reference superplasticizer dosage, $\pm 0.01\%$ and $\pm 0.02\%$ change from the reference dosage). The factor, V gives a measure of the departure of yield stress from its required value with respect to change in superplasticizer dosage. A lower value of V indicates a less sensitive and stable mixture proportion.

Flow table test

The flow values of mixtures were determined by performing the flow table test in accordance with ASTM C1437-15 (2015).

Assessment of structural build-up and workability retention

As previously explained, concrete mixtures undergo both reversible and irreversible changes due to thixotropy and hydration respectively. This structural build-up causes the yield stress to evolve with respect to time. To characterize this build-up, the vane shear test was performed on samples at regular intervals of 15 minutes to study the evolution of yield stress.

Alternatively, the structural build-up was also assessed through penetration test (in accordance with ASTM C403/C403M-16 (2016)) and by assessing the rate of cement hydration, using semi-adiabatic calorimetry. The apparatus used (see Figure 3.8) was in accordance with EN 196-9 (2010). It consisted of a box of size 102.5 × 102.5 × 62.5 cm made with thermocol, having 20 numbers of sample holders and a lid made with plywood. To perform the test, about 1575 grams of the concrete sample was placed in a cylindrical container of 80 mm internal diameter and 165 mm height. Prior to mixing, all materials were preconditioned at 25 °C for at least 24 hours. To compensate for the heat generated during the long mixing process (25 minutes), chilled water was used in preparing the samples for the calorimetry studies. After mixing, the sample was placed in the calorimeter and the rise in temperature was monitored over a period of 72 hours.

Figure 3.8: Semi-adiabatic calorimeter used in the study

The maximum time up to which the material was able to pass the extrudability test was defined as the time limit of printability. This is calculated exclusive of the time required for mixing the materials.

3.4 Results and discussions

3.4.1 Reference mixture design

Granular packing

The reference mixture design had a combination of portland cement and fly ash as binder. The proportions of all dry ingredients were optimized by using the particle packing method (Fennis and Walraven, 2012) using the commercial particle packing software, EMMA supplied by Elkem (2017). The modified Andreassen model (Funk and Dinger, 2013) with a distribution modulus (q) of 0.25 was used. The comparison of the combined particle size distribution of all solid dry ingredients for the final mixture proportion (shown in Table 3.2) and that suggested by the model is shown in Figure 3.9. A reasonable match can be seen between the actual and optimum particle size distributions. To achieve high strength, a low water to binder ratio of 0.32 was used. Polypropylene fibers were used at a nominal dosage of 1.8 kg/m^3 to control plastic shrinkage cracks.

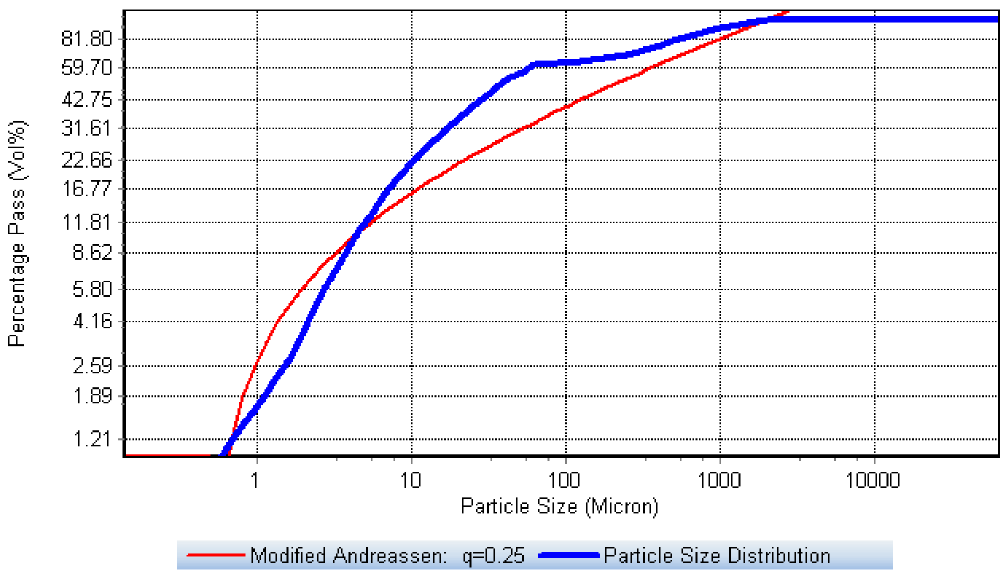

Figure 3.9: Comparison of the combined particle size distribution of all dry ingredients and the optimum distribution suggested by the modified Andreassen model

Table 3.2: Proportioning of materials for reference mix

Material	Quantity (kg/m^3)
Cement	663
Fly ash	166
Quartz powder	497
Quartz sand 1	373
Quartz sand 2	373
Water	265
Polypropylene fiber	1.8
Superplasticizer	0.83 (0.10 % of binder)

Superplasticizer dosage

The mixture design for layer-wise extrudable mixtures can be quite complex. The extrudability and buildability can depend on numerous factors. For instance, an increase in fiber amount can improve the buildability of the mixture (Kazemian *et al.*, 2017; Rushing *et al.*, 2017). But to reduce the complexity in the mixture design, the consistency of the mixture was changed only by adjusting the superplasticizer dosage. All other mixture proportion parameters were kept fixed. Table 3.3 shows the results of extrudability tests with different superplasticizer dosages. Up to a superplasticizer dosage of 0.08 %, the material was very stiff and did not extrude out of nozzle. Therefore, all trials up to 0.08 % of superplasticizer dosage failed due to material blockage in the nozzle itself. Figure 3.10a shows the results of extrudability test for 0.09 % of superplasticizer dosage. The material was extruded as a thin layer for a short length after which the pump started to stall. The extruded layer also did not conform to the required dimensions, and thus failed the extrudability test. On the other hand, Figure 3.10b shows the layer extruded when the superplasticizer dosage was further increased to 0.10 %. At this dosage, a continuous extrusion of the material was possible without blockages. The width and thickness of the extruded layer conformed with the dimensions of the nozzle. Hence, it was qualified as ‘pass’ in the extrudability test.

(a) Distorted layer

(b) Well-printed layer

Figure 3.10: Extrudability test

Table 3.3: Extrudability test for the reference mix

SP dosage (%)	Extrudability test
0	Fail
0.02	Fail
0.04	Fail
0.06	Fail
0.08	Fail
0.09	Fail
0.10	Pass

To obtain the upper limit of superplasticizer dosage, the buildability test was performed. This is shown in Table 3.4. There was no deformation of the bottom layer in the buildability test for the superplasticizer dosage of 0.10 %. However, on further increasing the superplasticizer dosage to 0.11 %, there was a 2 mm compression of the bottom layer. Hence, the buildability test was qualified as 'pass' only for the superplasticizer dosage of 0.10 %. From the two tables, it can be seen that the reference mixture passes both extrudability and buildability tests only at the superplasticizer dosage of 0.10 %. With a lower superplasticizer dosage, the yield stress and viscosity were too high to allow extrudability, whereas at a higher superplasticizer dosage, the yield stress was too low and mixture did not have the required shear strength for buildability.

The yield stress corresponding to this optimum superplasticizer dosage (0.10 %) was obtained as 1.6 kPa by using the vane shear test. Earlier, Le *et al.* (2012*a*) had used a similar approach to determine the shear strength of 3D printable concrete. The obtained shear strength values were in the range of 0.3 to 0.9 kPa. This difference may be because the former had used a smaller nozzle size (9 mm diameter circular nozzle) as compared to the current study (30 $\times$ 20 mm rectangular nozzle). For a smaller nozzle size, the weight to be sustained for each layer is lower. Hence, the former may have been able to obtain buildability with mixtures having comparatively lower yield stress. Figure 3.11 shows results of the robustness test for the reference mixture. There is a high variability in the yield stress indicated by a high value of the variability factor ($V = 4.5$ kPa). This explains the narrow working range obtained for the reference mixture.

The time limit of printability for the reference mix was only 15 minutes. Thereafter, the structural build-up was too high to allow extrudability.

Table 3.4: Buildability test for the reference mix

SP dosage (%)	Bottom layer compression (mm)
0.10	0
0.11	Collapse

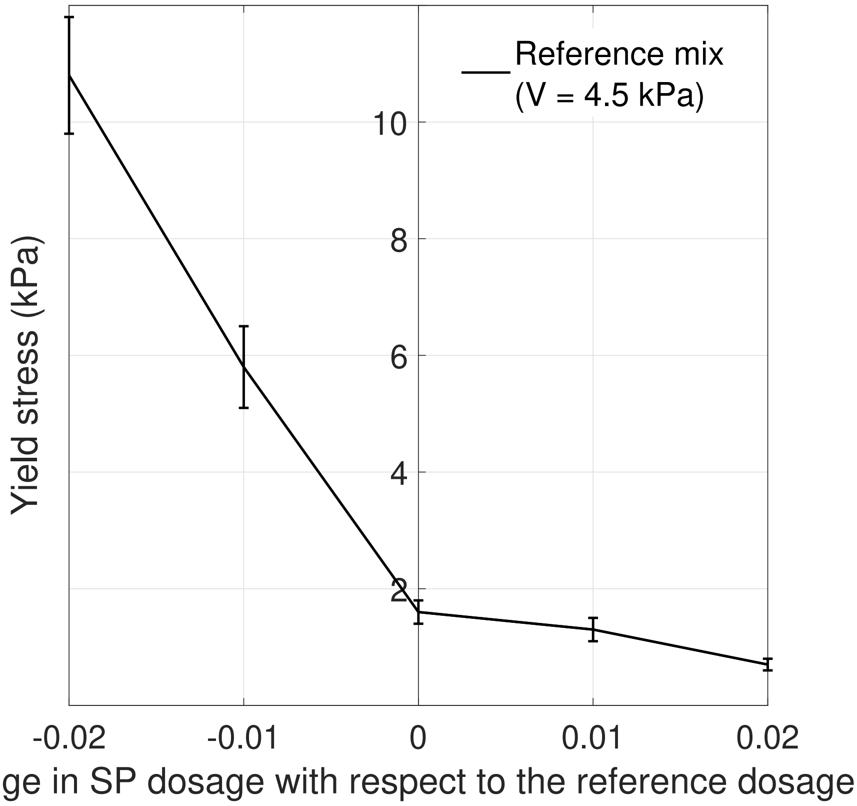

Figure 3.11: Robustness test for the reference mix

3.4.2 Additions to improve robustness

A recent study by Van Der Vurst *et al.* (2017) showed that the robustness of SCC was improved by the addition of VMA and nanoclay. Also, studies have shown that incorporating surplus fines having a larger specific surface area allows for fine adjustments in the consistency of SCC mixtures (Ramge and Lohaus, 2010). In this regard, the addition of silica fume may be beneficial. Therefore, the next phase of this study was to investigate the influence of nanoclay, VMA and silica fume on increasing the robustness.

Mixtures with nanoclay

Attapulgite clay is a relatively new material in concrete science and there is limited literature to decide on its dosage. Therefore, three dosages of 0.1, 0.2 and 0.3 % of binder content were investigated. Since it was used in very small amounts, the addition of nanoclay did not cause any change in the combined particle size distribution of the dry ingredients. For each dosage of nanoclay, the superplasticizer dosage was adjusted to obtain the same yield stress as that of the reference mixture (1.6 kPa). For 0.1, 0.2 and 0.3 % of nanoclay, the superplasticizer dosage had to be increased to 0.11, 0.12 and 0.13 % respectively to obtain the same reference yield stress. This suggests that the yield stress was increased with the nanoclay addition. Figure 3.12a shows the robustness test results of the nanoclay mixes. The nanoclay addition imparted considerable robustness. The value of variability factor, V decreased from 4.5 to 1.2 kPa with 0.1 % nanoclay addition. The value of V decreased further with increasing nanoclay dosage, but less predominantly (1.0 kPa and 0.7 kPa for 0.2 % and 0.3 % respectively).

Mixtures with VMA and silica fume

The mixtures with VMA dosage of 0.1 % of binder content and silica fume content of 10 % replacement of binder content were also investigated. The addition of fine particles of silica fume caused an change in the combined particle size distribution (shown in Figure 3.13). In comparison to Figure 3.9, a closer match can be seen between the actual and ideal particle size distribution as described by the modified Andreassen model with distribution coefficient of 0.27 (Elkem, 2017) after the addition of silica fume.

The addition of both VMA and silica fume increased the yield stress. For attaining the same reference yield stress (1.6 kPa), the superplasticizer dosage was increased to 0.18 % and 0.17 % respectively. The results of robustness tests are shown in Figure 3.12b. Silica fume addition lowered the value of V from 4.5 to 0.9 kPa whereas for VMA, it was lowered to 0.5 kPa. Therefore, VMA addition of 0.10 % of binder content resulted in the maximum robustness.

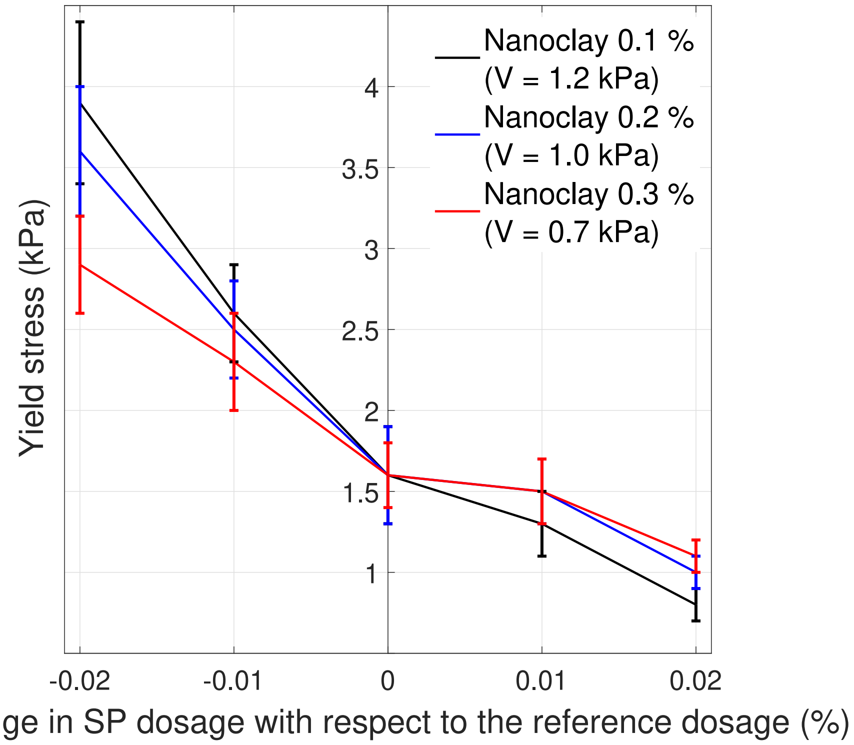

(a)

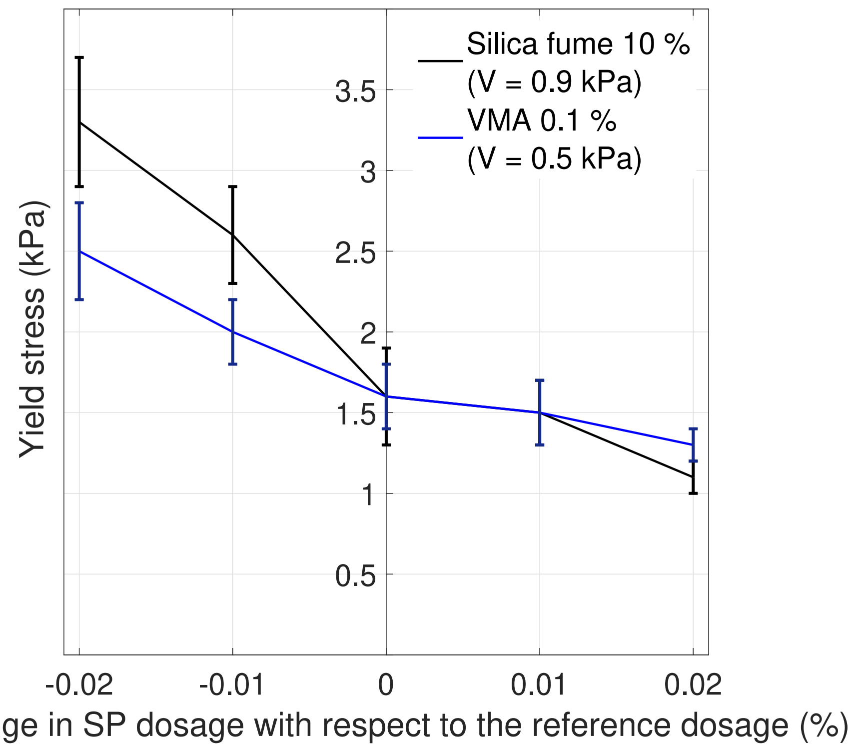

(b)

Figure 3.12: Robustness test for (a) nanoclay mixes and (b) mixes with VMA and silica fume

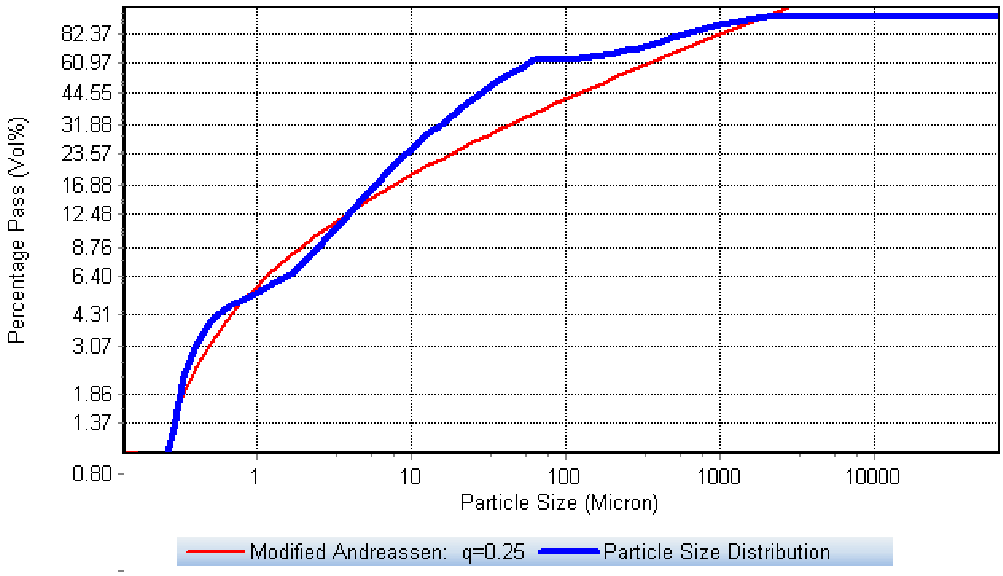

Figure 3.13: Comparison of the combined particle size distribution of all dry ingredients after adding silica fume and the optimum distribution suggested by the modified Andreassen model

3.4.3 Final mixture proportion

Since mixtures with 0.3 % nanoclay (mix NC), 10 % of silica fume (mix SF) and 0.10 % VMA (mix VM) were more stable and robust, these mixtures were subjected to further investigation. Table 3.5 summarizes the final mixture proportions.

Extrudability and buildability tests

Extrudability and buildability test results for SF, NC and VM mixes are summarized in Table 3.6. As expected, the VM mix with a lower value for the variability factor was less sensitive to change in superplasticizer dosage. It had a working range of 0.16 to 0.19 % superplasticizer dosages, for which the mixture passed both extrudability and buildability tests. The mixtures NC and SF (with V values of 0.7 and 0.9 kPa respectively) were comparatively more sensitive, and had a working range of 0.12 to 0.14 % and 0.17 to 0.18 % respectively. Also, it can be seen that all the working mixtures have a yield stress in the range of 1.5 - 2.5 kPa.

Table 3.5: Final mixture proportions

Material	Quantity (kg/m^3)		
	Mix SF	mix NC	mix VM
Cement	574	663	663
Fly ash	164	166	166
Quartz powder	492	497	497
Quartz sand 1	369	373	373
Quartz sand 2	369	373	373
Water	262	265	265
Polypropylene fiber	1.8	1.8	1.8
Superplasticizer	1.39 (0.17 %)	1.08 (0.13 %)	1.49 (0.18 %)
Additive type	Silica fume	Nanoclay	VMA
Additive dosage	81.9 (10 %)	2.47 (0.3 %)	0.82 (0.1 %)

Table 3.6: Buildability and extrudability tests for SF, NC and VM mixes

Mix name	SP dosage	Buildability (comp. of bottom layer in mm)	Extrudability	Yield stress (kPa)	Flow value (%)
SF	0.19	2 ± 0.5	Pass	1.1 ± 0.1	97 ± 10
	0.18	0	Pass	1.5 ± 0.2	89 ± 10
	0.17	0	Pass	1.6 ± 0.3	80 ± 5
	0.16	0	Fail	2.6 ± 0.3	55 ± 5
NC	0.15	2 ± 0.5	Pass	1.1 ± 0.1	115 ± 15
	0.14	0	Pass	1.5 ± 0.2	100 ± 10
	0.13	0	Pass	1.6 ± 0.2	95 ± 10
	0.12	0	Pass	2.3 ± 0.3	90 ± 10
	0.11	0	Fail	2.9 ± 0.3	60 ± 5
VM	0.20	2 ± 0.5	Pass	1.3 ± 0.1	100 ± 10
	0.19	0	Pass	1.5 ± 0.2	88 ± 10
	0.18	0	Pass	1.6 ± 0.2	80 ± 5
	0.17	0	Pass	2.0 ± 0.2	70 ± 5
	0.16	0	Pass	2.5 ± 0.3	65 ± 5
	0.15	0	Fail	3.0 ± 0.4	40 ± 5

Assessment of structural build-up

As previously explained, concrete mixtures undergo both reversible and irreversible changes due to thixotropy and hydration respectively. This structural build-up causes the yield stress to evolve with respect to time. To characterize this build-up, the vane shear test was performed on samples at regular intervals of 15 minutes. Figure 3.14a shows the evolution of yield stress with respect to time. For short duration of elapsed time, the yield stress increased linearly with time while for longer duration, the response was found to be exponential. This type of a response has been previously confirmed by other researchers (Perrot *et al.*, 2015, 2016). Perrot *et al.* (2015) proposed a model to describe the growth of yield stress with time. The model is given by

$$Y(t) = A_{thix} t_c \left(e^{\frac{t}{t_c}} - 1 \right) + Y(t = 0). \tag{3.7}$$

In the above equation, $Y(t)$ represents the yield stress at a time t, A_{thix} is the flocculation rate and t_c is the characteristic time. Note that the first order Taylor polynomial for $e^{\frac{t}{t_c}}$ at $t = 0$ is equal to $\frac{t}{t_c} + 1$. Hence for short times, the model approximates to a linear form. Figure 3.14a shows a comparison of the experimental data with the values predicted by the model. All mixes had the same initial yield stress ($Y(t = 0)$ = 1.6 kPa). The characteristic time, t_c was found to be higher for VM mix (46 min), followed by NC (41.5 min) and SF mixes (34.5 min). The flocculation rate, A_{thix} was the highest for SF (29.4 Pa/min), followed by NC (23.5 Pa/min) and VM (17.7 Pa/min). In the study by Perrot *et al.* (2016), the model parameters obtained for a 3D printable concrete were 26 min and 28 Pa/min for t_c and A_{thix} respectively. Earlier, Roussel (2006) classified self compacting concrete based on the flocculation rate, A_{thix}. The mixtures were categorized as non-thixotropic (A_{thix} less than 6 Pa/min), thixotropic (A_{thix} between 6 Pa/min and 30 Pa/min)and highly thixotropic (A_{thix} higher than 30 Pa/min). However, the classification by Roussel (2006) was based on a linear model of yield stress with time ($Y(t) = A_{thix}t + Y(t = 0)$), which as observed in this study and earlier by Perrot *et al.* (2015), is valid only for short time duration. Therefore, at present, there is only a limited knowledge on the use of this model and the range of values for A_{thix} and t_c suitable for layer-wise extrudable mixtures. To gain further understanding, more studies are needed in this regard.

Penetration resistance and semi-adiabatic heat curves

Penetration resistance and semi-adiabatic heat curves were also determined to describe the structural build-up with time. Figure 3.14b shows the penetration curves for the VM, NC and SF mixes. The initial and final set times are shown in Table 3.7. The SF mix took the minimum time to attain initial and final set while the VM mix took the maximum time. This indicates that the structural build-up is higher in the SF and the least in VM mix. This is in agreement with trend observed in the evolution of yield stress with time plots as shown in Figure 3.14a.

Figure 3.14c shows the rise in temperature plotted against elapsed time after mixing. It can be seen that mixes SF and NC show a similar rate of hydration while the curve for VM was to the right and below the curves for NC and SF. The values of peak temperature rise and the time taken to reach the peak are shown in Table 3.8. VM took the maximum time to reach the peak temperature rise as compared to the other two mixes. This indicates that the the structural build-up due to cement hydration is slower in the VM mix. The reason for this may be attributed to the higher dosage of chemical admixtures in VM as compared to the other two mixtures, which results in retardation.

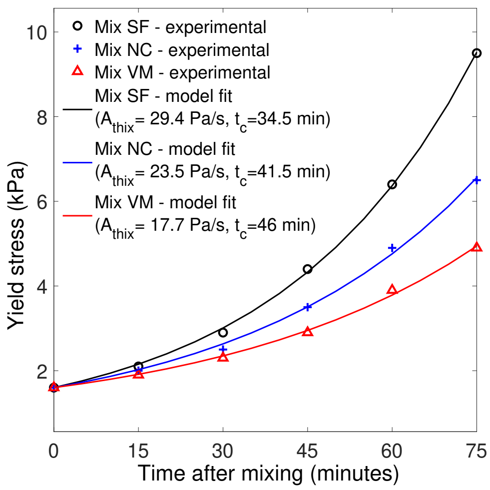

(a) Yield stress with time

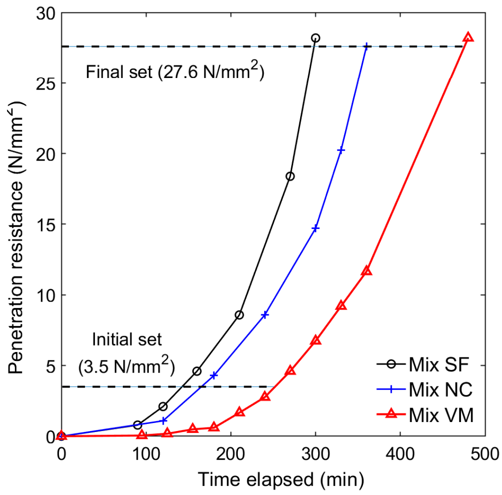

(b) Penetration resistance with time

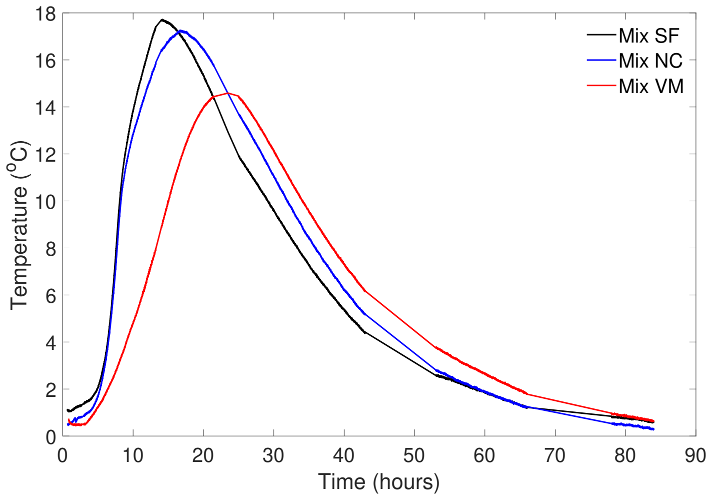

(c) Rise in temperature by semi-adiabatic calorimetry

Figure 3.14: Assessment of structural build-up in SF, NC and VM mixes

Table 3.7: Initial and final setting times

Mix name	Initial set time (min)	Final set time (min)
SF	142	298
NC	165	360
VM	252	476

Table 3.8: Time taken to reach peak temperature rise in semi-adiabatic calorimetry

Mix name	Peak temperature rise (°C)	Time taken to reach peak temperature (hours)
SF	17.7	14
NC	17.3	16.7
VM	14.5	23.5

Time limit of printability

The time limits of printability for SF, NC and VM were 30, 30 and 45 minutes respectively. The higher time limit of printability for VM mix may be because of its slow structural build-up as seen in the evolution of yield stress with time plot (Figure 3.14a). The slow structural build-up was also reflected in the higher initial setting times (Table 3.7) and the lower peak temperature (Table 3.8) attained in semi-adiabatic calorimetry for the VM mix.

3.5 Summary

Based on the experiments conducted using a laboratory-scale test bed printer, a yield stress based mix design approach for 3D printable concrete was presented. It was found that layer-wise buildability is possible only when the yield stress is within a certain range (1.5 to 2.5 kPa). Below this range, the mix is too flowable to have shape retention wheras above this range, the mix is too stiff to allow extrudability. The effect of special additives like micro-silica, nanoclay and VMA was also examined. The addition of VMA resulted in the maximum robustness and the addition of micro-silica provided the maximum rate of structural build-up. The understanding gained from this study on the small-scale laboratory printer can now be used as a basis for developing printable formulations for large-scale printer systems.

CHAPTER 4

SCALING-UP TO A LARGER 3D PRINTER SYSTEM

4.1 Introduction

In this chapter, the mix development for a large-scale concrete 3D printer system, and the challenges associated with scaling-up are discussed. An important aspect in this regard is assessing the stability of the concrete when subjected to the higher extrusion pressure applied in the larger 3D printer system. The tendency for phase separation to occur during the extrusion process is quantified by using desorptivity as a fundamental material parameter. Based on desorptivity, an index is developed to evaluate the occurrence of phase separation. This study is then extended to develop mixes with the inclusion of coarse aggregates.

4.2 Materials and methods

4.2.1 Mix proportion

The VM mix developed using the small-scale 3D printer was used the basis for developing the control mix for the large-scale 3D printer. The reason to choose this mix was because the special additive used in the mix is a methylcellulose-based VMA, which, as discussed in the preceding section, can improve the water retention capacity of the mix. In the VM mix, the aggregates consisted of quartz powder and two types of quartz sand designated as quartz sand 1 and quartz sand 2. However, since quartz powder and quartz sand 2 are expensive and not suitable for large-scale 3D printing, the control mix was developed using only quartz sand 1 as the fine aggregate. The water-cement ratio (0.32) and the dosage of polypropylene fibers (1.8 kg/m^3) were maintained the same as that in the VM mix. The proportioning of the all dry materials, as before, was done by the particle packing method (Fennis and Walraven, 2012) using the EMMA software. The final proportion of the dry materials and the water content used in the control mix is shown in the Table 4.1. The determination of dosage of chemical admixtures (superplasticizer and methylcellulose) will be explained later in section 4.3.1.

In addition to the control mix, mixes with inclusion of coarse aggregate of maximum nominal size 10 mm were also developed. Light weight expanded clay aggregate (LECA) was used as the coarse aggregate. LECA (Figure 4.1) is manufactured by heating natural clay in a rotary kiln at about 1200 °C. The physical properties of LECA used are summarized in Table 4.2 and the particle size distribution (PSD) of the dry materials used are shown in Figure 4.2. In the control mix, the fine aggregates were replaced by 15 %, 30 % and 45 % by volume with LECA to obtain the mixes CA15, CA30 and CA45 respectively. Prior to mixing, both quartz sand 1 and LECA were prewetted to saturated surface dry condition. The proportion of all the dry materials for all the mixes used are summarized in Table 4.1. It should be noted since the aggregate to binder weight ratio is maintained the same for all the mixes, the weight of cement, fly ash and water are lower in CA15, CA30 and CA45 mixes due to replacement with low density aggregates. For all the mixes containing LECA, the dosage of polypropylene fibers and the chemical admixture dosages were kept the same as that used in the control mix.

Table 4.1: Mixes proportion for studies with the large-scale 3D printer

Material	Quantity (kg/m^3)			
	Control mix	CA15	CA30	CA45
LECA	-	101	210	329
Quartz sand 1	1237	1093	938	769
portland cement	660	637	612	585
Fly ash	165	159	153	146
Water	264	255	245	234
Density	2326	2245	2158	2063

Table 4.2: Properties of the aggregates used in the study

Property	Quartz sand 1	LECA
Water absorption (%)	2.10	12.0
Specific gravity in saturated surface dry condition	2.68	1.40
Bulk density (kg/m^3)	1416	634

Figure 4.1: LECA used in the study

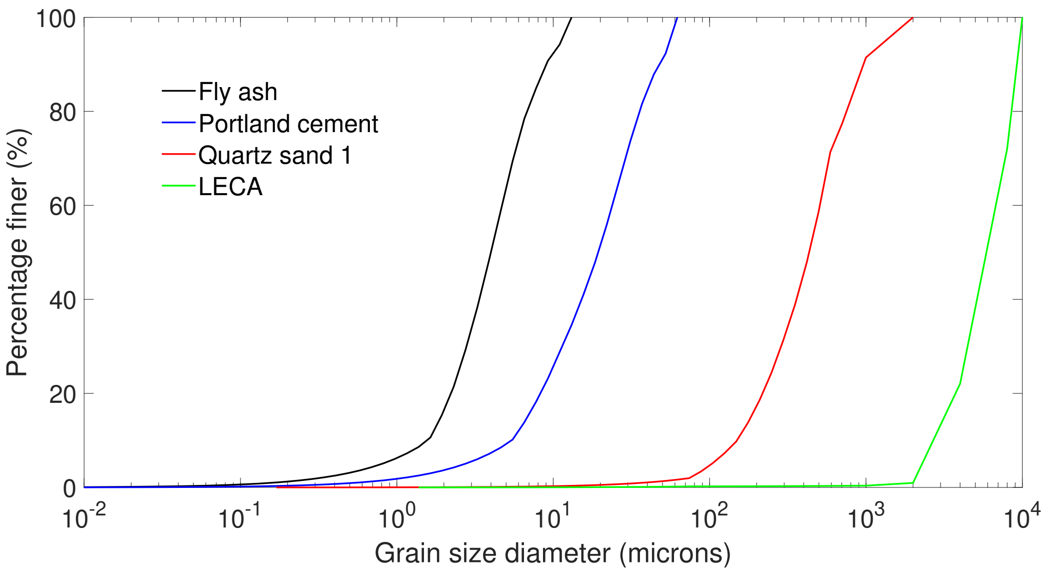

Figure 4.2: Particle size distributions of materials used

4.2.2 Mixing procedure

For conducting trials with the large-scale 3D printer, the mixing was done by using a pan type mixer. At first, all the dry materials including the coarse aggregates were pre-blended in the mixer for 2-3 minutes. The water mixed with the liquid superplasticizer was then slowly added to the dry blend. After mixing for about 5 minutes, the mixing was stopped and the VMA in the powder form was sprinkled over the mix. Then mixing was resumed for another five minutes. After this, fibers were sprinkled over the mix in a similar manner. The total mixing time was 20 minutes and in each batch, about 35 litres of concrete were prepared.

4.2.3 Assessment of phase separation

Theory

As pointed out earlier in section 2.4, the pressure applied during the extrusion process may cause the liquid phase in the concrete to separate out from the matrix leaving behind a dewatered and unextrudable mass. The dewatering tendency of the concrete may be characterized based on the Terzaghi's law for one-dimensional filtration (Terzaghi, 1965). The law states that the cumulative height of the water column that bleeds out from a filtrate of suspension when subjected to a constant pressure is proportional to the square root of the time for which the pressure is applied. The constant of proportionality is a fundamental material parameter of the filtrate for a given pressure and is called desorptivity. Mathematically, Terzaghi's law can be expressed as (Terzaghi, 1965) as given by

$$i = Rt^{\frac{1}{2}}. \tag{4.1}$$

In the above equation, i denotes the cumulative height of bleed water column (mm). It is obtained by dividing the cumulative volume of bleed water obtained at any time, t by the cross-sectional area of the filter.

Filtration cell

The desorptivity measurements were made using a filtration cell which consisted of a cylinder having an opening in the top and bottom cap (see Figure 4.3). The opening in the top was connected to a pressure line of Argon gas. Just before the opening in the bottom cap, a Whatman filter paper of 2.6 μm pore size was placed. From Figure 4.2, it can be seen that more than 80 % of all the granular materials used have size greater than 2.6 μm. Hence, only the pore solution passes through the filter paper which then drains out through the opening in the bottom cap. Similar arrangement for assessing phase separation has been used by various other researchers as well (Khayat *et al.*, 1999; Green *et al.*, 1999).

(a)

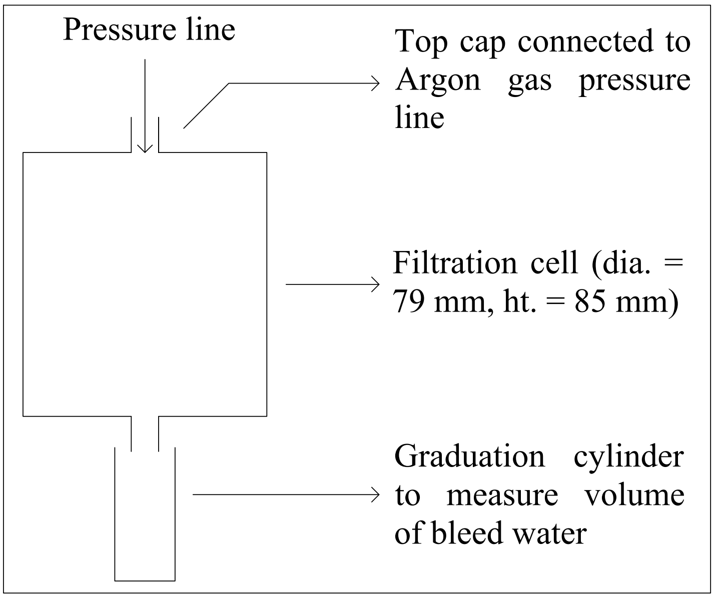

(b)

Figure 4.3: (a) A photo along with the (b) schematic diagram of the filtration cell used in the study

To perform the test, the concrete after mixing was transferred to the filtration cell in two layers, and with each layer given 25 numbers of blows with a tamping rod. The top cap is then attached and connected to the Argon gas pressure line. A constant pressure of 4 kg/cm^2 is then applied in the cell. The volume of bleed water that drains out from the cell after different intervals of time, up to of a total duration of 400 seconds is noted. Desorptivity is then determined from the Terzaghi's law (Terzaghi, 1965) using Equation (4.1).

Loss of workability

To assess the loss of workability in the mix due to liquid phase migration, the flow table test (ASTM C1437-15, 2015) was performed before and after the application of pressure in the filtration cell. The loss of workability was expressed by the percentage reduction in the flow value given by

$$\text{Reduction in flow } (\%) = \frac{\text{Initial flow value - Final flow value}}{\text{Initial flow value}} \text{ x } 100. \tag{4.2}$$

4.2.4 Packing density

The packing density of the different mixes was measured by using the wet packing method suggested by **?**. In this method, to determine the packing density of a concrete mix, its solid concentration is determined at different w/c. At relatively low and high w/c, the solid concentration reduces due to the presence of air voids and the loosening effect respectively. However, at an intermediate w/c ratio called the optimum w/c, the particles become closely packed, and the measured solid concentration becomes maximum. This value obtained at the optimum w/c is taken as the packing density of the granular skeleton.

For determining the solid concentration at a given w/c, the concrete was filled in a cylindrical mould of 3 liters capacity. The filling was done in three layers, with each layer followed by 25 blows with a tamping rod. The solid concentration, ϕ is then given by

$$\phi = \frac{V_s}{V}. \tag{4.3}$$

In the above equation, V_s represents the total volume of all granular materials present in the mix and V represents the volume of the container. V_s can be determined from the volume proportion and specific gravity of each material used in the mix. For each mix, three tests were conducted and the average value is reported.

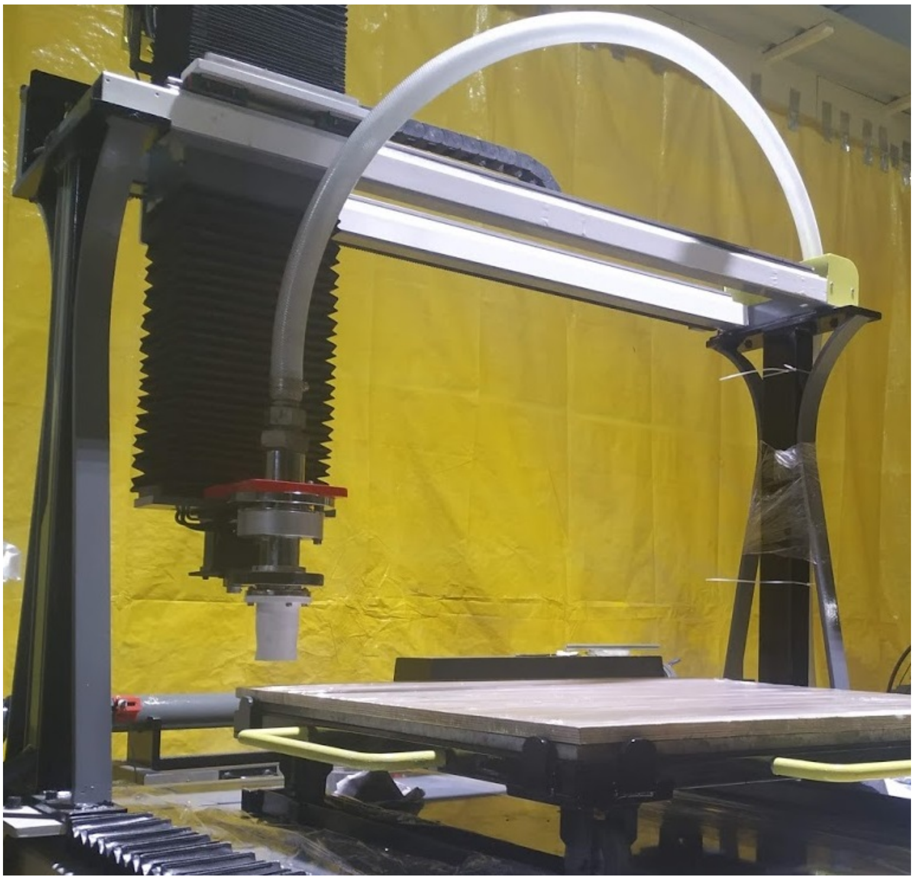

(a)

(b)

Figure 4.4: (a) Large-scale 3D printer and (b) a module printed using it

4.2.5 Large-scale 3D printer

The large-scale 3D printer used in the study is shown in Figure 4.4 and its different components are shown in the schematic sketch in Figure 4.5. To allow printing even with mixes containing coarse aggregates, a piston pump was used as the extruder as compared to the screw pump used in the small-scale 3D printer. The other components of the large-scale system include the material accumulator or primer, the piston pump and the 3D printer along with the nozzle assembly. To perform a printing job, the material after mixing is manually transferred into the large cylinder of the primer. A ram extruder is then used to push the material in the primer into the piston pump. From the piston pump, the material is extruded out at a constant displacement rate though the print head consisting of a square nozzle of 30 $\times$ 30 mm. The transfer of the material from the primer to the piston pump and extrusion from the pump through the print head is fully automated using a control system. The bed size of the printer is 750 $\times$ 750 mm and the maximum possible print height is 500 mm.

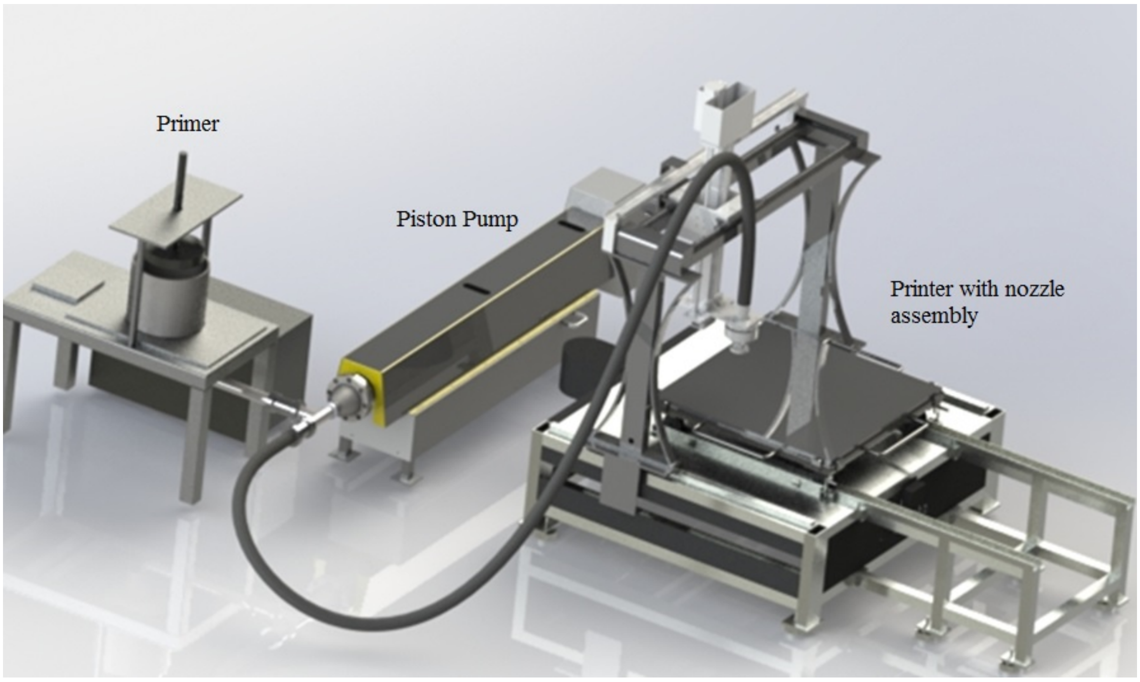

Figure 4.5: Schematic sketch showing the different components in the large-scale 3D printer system (taken from the user manual provided by the manufacturer (Tvasta – Industrial 3D Printing, 2019))

4.2.6 Extrudability tests using the large-scale 3D printer

To perform the extrudability test, about 6 litres of material is used to fill the cylindrical piston. The material is then extruded out at a constant displacement rate of 44 mm/s. For the extrusion of the complete material from the pump, a total time of 330 seconds is required. If there is phase separation of the concrete mix during extrusion, then there will be a sudden build-up of pressure, causing the piston pump to stall. The mix is categorized as 'fail' in the extrudability test in such cases. On the other, if the mix is able to continuously extrude for the total duration of 330 seconds, then it is categorized as 'pass' in the extrudability test.

4.2.7 Uniaxial compression tests to assess buildability

For the small-scale test bed printer, buildability was assessed based on having the required yield stress to prevent plastic collapse. However, for large-scale additive manufacturing, when tall slender elements are to be printed, the elastic modulus of the fresh concrete also becomes an important material parameter (Roussel, 2018*b*). The importance of elastic modulus is in providing resistance against buckling failure. A few recent literature have suggested the use of uniaxial compression test of fresh concrete for assessing buildability (Wolfs *et al.*, 2018; Panda *et al.*, 2019). In such studies, the stress-strain response of fresh concrete at different early ages is determined. The compressive strength as well as the elastic modulus measured from the initial elastic region of stress-strain plot are then used to assess the occurrence of plastic and buckling type collapse respectively.

Therefore, for assessing the buildability of the mixes developed for the large-scale printer, uniaxial compression tests were performed on cylindrical specimens of size 2.5×5 in. (63×126 mm). To cast the specimens, the concrete after mixing was extruded through the test bed printer. The extruded concrete was collected and filled in the cylinder in three layers, with each layer compacted by 25 blows with a tamping rod. After this, the specimen was demoulded from the cylinder. For materials like fresh cement paste and concrete, the stress-strain response can depend on the rest duration of the specimen prior to testing (Wolfs *et al.*, 2018). To characterize the evolution in the stress-strain response with rest time, the uniaxial compression tests were performed on specimens with different rest durations (0, 60, 120, 180, 240, 300, 360 and 420 minutes). For each case, a total of three specimens were tested and the average value is reported.

(a)

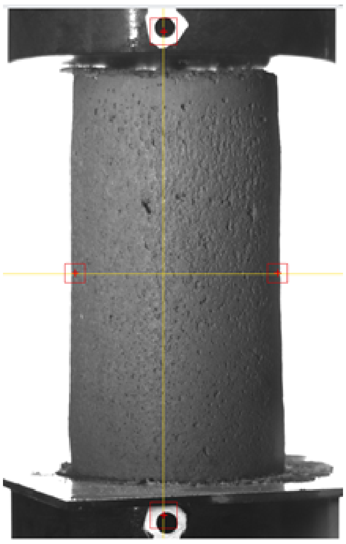

(b)

Figure 4.6: (a) Uniaxial compression test setup with the video extensometer system (b) gauge point detection in the video extensometer system

The testing was done using the Zwick Roell machine fitted with a 5 kN load cell (Figure 4.6a). The rate of loading was 30 mm/min. Both longitudinal and transverse displacement were measured by the use of a video extensometer system. Figure 4.6b shows the gauge points for the displacement measurements. It should be noted that the gauge points are chosen along the edges of the specimen, i.e., both the longitudinal and transverse displacements are measured globally. This procedure was adopted as local displacement measurements were not possible since it was difficult to attach detection marker on the fresh concrete specimens without causing any rupture to it. By choosing the gauge points along the boundary, it was possible to obtain sufficient contrast with the background to facilitate the detection in the video extensometer system. Prior to testing, the loading plates were applied with lubricating oil to reduce the effect of the biaxial stress that may occur due to the friction between the specimen and the loading plates.

4.3 Results and discussions

4.3.1 Effect of methylcellulose on desorptivity

In the mixture development illustrated in Chapter 1, all mixes were adjusted to have a yield of 1.6 kPa. This yield stress value was based on experiments conducted using the small-scale test bed printer fitted with 30×20 mm rectangular nozzle. For the large-scale printer, the nozzle size is 30×30 mm. To ensure buildability with the increased nozzle size, the superplasticizer dosage for the control mix was adjusted such as have a higher yield stress of 1.9 kPa. This yield stress value was determined based on the same experiments illustrated in Chapter 3 but by using a 30×30 mm square nozzle in the small-scale test bed printer.

For the control mix, the desorptivity of the mixes having different amounts of methylcellulose were examined. The addition of methylcellulose causes an increase in the yield stress of the mix. However, to maintain the yield stress of 1.9 kPa for all mixes, the superplasticizer dosage was also increased for the mixes with higher methyl cellulose content. The dosages of methylcellulose and superplasticizer used for the control mix are summarized in Table 4.3. The control mix was tested with two different methylcellulose contents. The maximum methylcellulose content used was 0.25 %. This was because beyond 0.25 %, the desorptivity of the mix was too low and no measurable bleed water was obtained, particularly at low pressure values. This maximum dosage of 0.25 % as well the 50 % of this dosage (0.125 %) were assessed.

Table 4.3: Dosages of superplasticizer and methylcellulose as a percentage of binder content of the control mix

Trial no.	Superplasticizer (%)	methylcellulose (%)
Trial 1	0.01	0
Trial 2	0.05	0.125
Trial 3	0.08	0.25

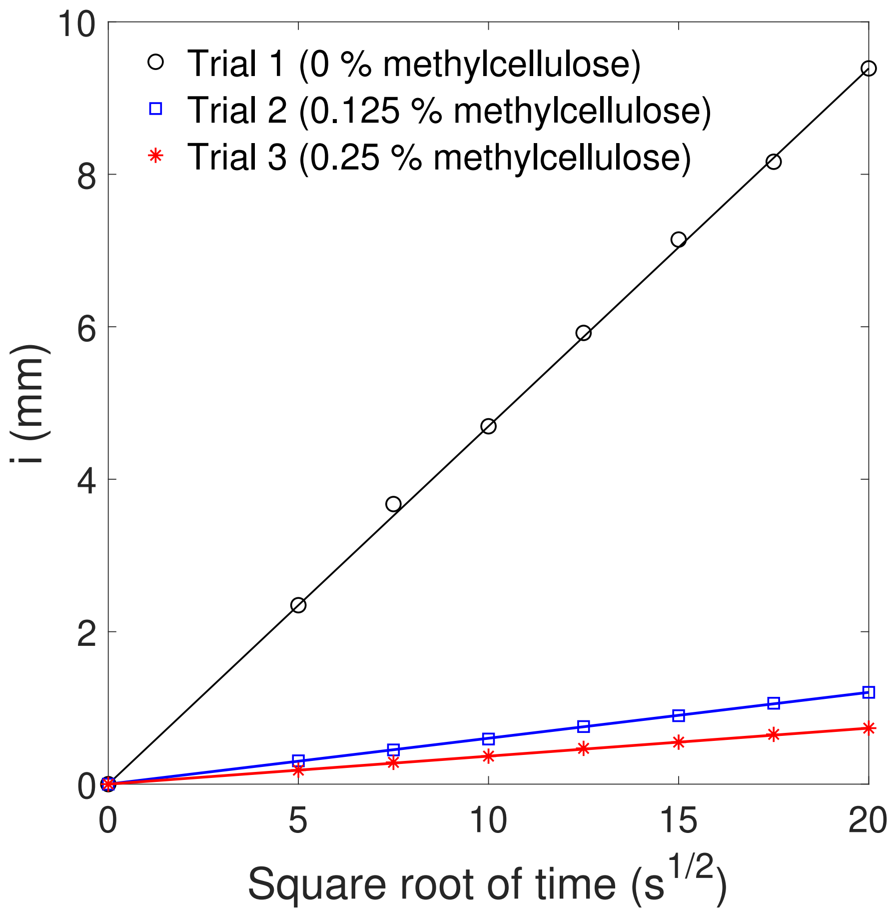

Figure 4.7: Height of bleed water column (i) vs square root of time for the control mix with different methylcellulose content

Figure 4.7 show the cumulative height of bleed water column (i, in Equation (4.1)) plotted against the square root of time for mixes with different methylcellulose content. The slope of the graph denotes the desorptivity (R) which gives a measure of water retaining capacity of the mix. The increase in methylcellulose content decreased the value of the desorptivity. These results are in agreement with previous studies that point out the beneficial effect of methylcellulose in reducing phase separation (Saric-Coric *et al.*, 2003; Patural *et al.*, 2011; Zhou *et al.*, 2019). This improvement is due to the intermolecular sorption of water at low dosages and the formation of hydrocolloidal gels at higher dosages (Bülichen *et al.*, 2012; Brumaud *et al.*, 2013).

4.3.2 Extrudability tests for mixes with different binder types

The results of the extrudability tests for the control mix with different methylcellulose content are shown in Table 4.4. Only the mix with highest methylcellulose content (0.25 %) was able to pass the extrudability test. Conventionally, the percentage amount of bleed water obtained from the tests such as ASTM C1741-18 (2018) is used to evaluate the phase separation tendency of mixes. However, such methods are single-point measurements, i.e. bleed water computed after a fixed amount of time. An index based on desorptivity can be used to better evaluate the phase separation of printable mortars. As explained in section 4.2.6, the extrudability tests were performed with 4 kg/cm^2 of maximum possible pressure and the time required for complete extrusion of the material in the piston was 330 seconds. The desorptivity values of the different mixes at 4 kg/cm^2 pressure, and the volume of bleed water column (mm) calculated using Equation (4.2) with t as 330 seconds are also shown in Table 4.4. Now, this value (denoted as index, I) was normalized with respect to the original height of water column in the filtration cell. The original height is obtained by dividing the volume of water contained in the mix added to the filtration cell by the cross-sectional area of the cell. This normalized index value, denoted as I_{norm} is shown in column 6 of Table 4.4. A distinction can be seen between the I_{norm} values of mixes categorized as 'fail' and those categorized as 'pass' in the extrudability tests.

Table 4.4: Results of extrudability tests for different control mix with varing with methylcellulose content

Mix	Desorptivity (mm/s$^{\frac{1}{2}}$)	Index (I)	Normalized index I_{norm}	Extrudability
Trial 1	0.470	8.54	0.43	Fail
Trial 2	0.060	1.09	0.06	Fail
Trial 3	0.037	0.67	0.03	Pass

To validate the index, I_{norm} for over a wide range of mixes, extrudability tests were carried out on mixes with varying desorptivity values. The mixes used were adopted from the work of Sharma (2019) and were formulated using different binders, water to cement ratio and chemical admixture dosages. Sharma (2019) proportioned mixes using mineral admixtures like ground granulated blast furnace slag (conforming to ASTM C989 / C989M-18a (2018)) and limestone calcined clay (LC2) blend (with limestone to calcined clay ratio of 1:2, and kaolinite content in the original clay of 70 %). The aggregate type, the aggregate to binder ratio and the chemical admixtures (methylcellulose and PCE) used were the same as that used in the current study. Mixes with water to cement ratio of 0.28 and 0.32 were investigated in his study. All the mixes were formulated to have a yield stress in the range of 1.5 to 2 kPa by adjusting the superplasticizer dosage. The binder type and the chemical admixture dosages used in the different mixes are shown in Table 4.5. The major findings of the study by Sharma (2019) were that the desorptivity and hence, the tendency for phase separation for the different mixes decreases with an increase in the content of water retaining admixtures like methyl cellulose, decrease in packing density and water/cement ratio.

Table 4.5: Results of extrudability tests for mixes with different binder types and water to cement ratio (desorptivity values for the mixes taken from Sharma (2019))

W/C	Binder type	SP (%)	methylcellulose (%)	Desorptivity (mm/s$^{\frac{1}{2}}$)	I_{norm}	Extrudability
0.32	OPC (50 %) + Slag (50 %)	0.08	0	0.282	0.26	Fail
	OPC (50 %) + Slag (50 %)	0.11	0.075	0.037	0.03	Pass
	OPC (50 %) + Slag (50 %)	0.14	0.150	0.020	0.02	Pass
	OPC (70 %) + LC2 (30 %)	0.25	0	0.086	0.08	Fail
	OPC (70 %) + LC2 (30 %)	0.30	0.035	0.030	0.03	Pass
	OPC (70 %) + LC2 (30 %)	0.34	0.070	0.028	0.03	Pass
0.28	OPC (80 %) + FA (20 %)	0.05	0	0.224	0.23	Fail
	OPC (50 %) + Slag (50 %)	0.15	0	0.099	0.10	Fail

The results of the extrudability tests and values of I_{norm} for the different mixes adopted from Sharma (2019) are shown in Table 4.5. From both Tables 4.4 and 4.5, it can be seen that mixes with the values of I_{norm} greater than or equal to 0.06 failed the extrudability test. Unlike the conventional approach of expressing the water retention capacity in terms of the percentage of bleed water, the determination of I_{norm} depends on the amount of time required for the extrusion of complete material in the piston, which in turn depends on the extrusion speed. Also, it should be noted that the maximum possible pressure of 4 kg/cm^2 was used in computing the value of I_{norm}. This is a conservative approach, as in the actual case, the pressure may be lower during the initial stages of the extrusion process. As phase separation starts to occur, the pressure starts to increase and may reach the value of maximum pressure of 4 kg/cm^2. Therefore, pressure versus time data may be used for a more detailed and accurate analysis.

4.3.3 Effect of coarse aggregate addition on desorptivity and extrudability

From Table 4.4, it can be seen that Trial 3 containing 0.08 % superplasticizer and 0.25 % methylcellulose passed the extrudability test. Therefore, this was taken as the chemical admixture dosage for the control mix as well for the mixes containing coarse aggregates (CA15, CA30 and CA45). Figure 4.8 shows the cumulative height of bleed water column (i, in Equation (4.1)) plotted against the square root of time for mixes with different levels of coarse aggregate content. It can be seen that the desorptivity value increases and hence, the water retention capacity decreases with an increase in the coarse aggregate content. Since the amount of chemical admixtures were kept the same in all the mixes, the increase in desorptivity may be attributed to change in packing density. As seen in Table 4.6, the addition of coarse aggregate causes a reduction in the packing density. Therefore, the increase in desorptivity may be attributed to this reduced packing density. This is because as packing density increases, it becomes more difficult for the pore solution to drain out through the granular skeleton, thereby decreasing the desorptivity.

Due to presence of the larger size coarse aggregates, the yield stress measurement by vane shear apparatus could not be performed on mixes containing coarse aggregates. The workability of the mixes was assessed using the flow table test. The results of the flow table tests are shown in Table 4.7. The initial flow value is the same for the different mixes indicating that the addition of coarse aggregate does not cause much change in the initial workability. The column 3 of Table 4.7 indicates the flow value after the application of pressure in the filtration cell, and column 4 shows the reduction in flow value with respect to the initial flow value. It can be seen that there is a greater reduction in the flow value with an increase in the coarse aggregate content of the mix. This again can be attributed to the fact that more dewatering occurs in the mixes with higher coarse aggregate content due to its higher desorptivity value, which in turn, leads to an increased loss of workability. The results of extrudability tests and the I_{norm} values computed for the mixes with coarse aggregate are shown in Table 4.8. The mix CA45 pass had a high I_{norm} and therefore failed the extrudability test.

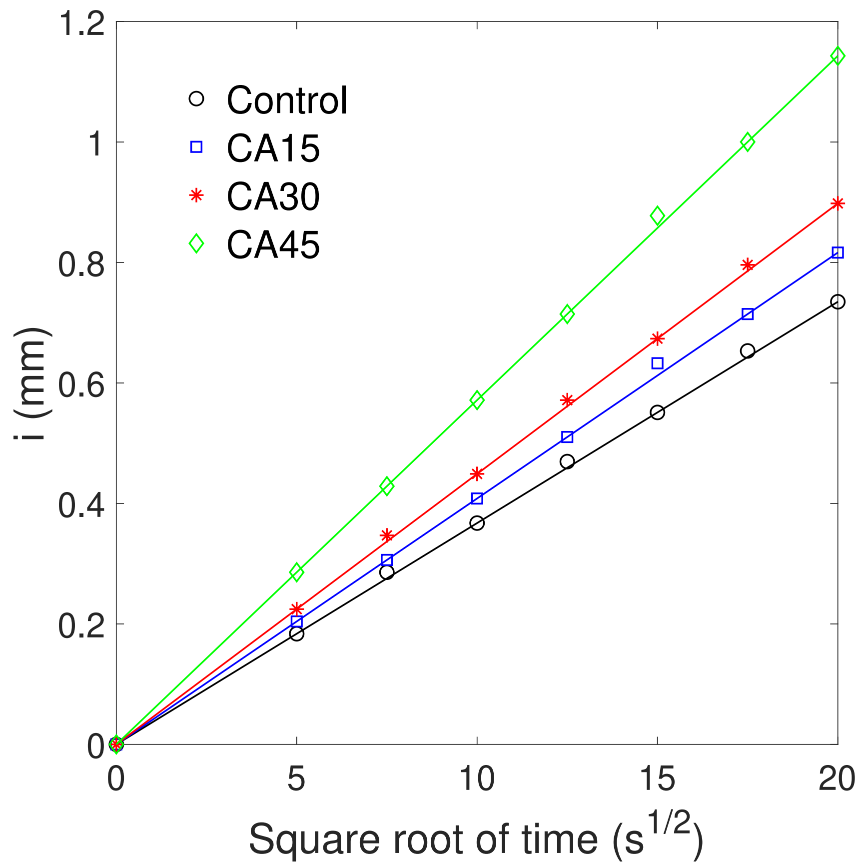

Figure 4.8: Height of bleed water column (i) vs square root of time for the mixes with different coarse aggregate content

Also, it should be noted that the differences in the pressure required to pump can also be a factor that affects the extrudability of mixes. For instance, Choi *et al.* (2014) studied the effect of increasing the aggregate size on concrete pumping. They measured the pumping pressure for different concretes having aggregate sizes varying from 10 to 25 mm. They found that the pressure required increases with an increase in the aggregate size. However, unlike conventional pumping operations where pipe lengths can be several hundreds of meters in length, for the 3D printer system used in the current study, the length of hose pipe connecting piston to the nozzle is only 5 m. Further, the hose pipe material is a polymer with a low coefficient of friction. Also, prior to the beginning of the printing operation, the inside of the pipe is lubricated with oil to further reduce the effect of pipe friction. Due to these factors, the effect of differences in the pressure required to pump is less dominant. However, for large scale 3D printer systems involving longer lengths of pipes, it is also important to consider this factor in the analysis.

Table 4.6: Packing density of different mixes

Mix name	Packing density (%)
Control	68.5
CA15	67.5
CA30	66.8
CA45	65.3

Table 4.7: Results of flow table tests

Mix name	Initial flow value (cm)	Final flow vaue (cm)	Reduction in flow value (%)
Control	18.5	18.3	1.1
CA15	18.4	17.6	4.3
CA30	18.7	17.0	9.1
CA45	18.3	15.6	14.8

Table 4.8: Results of extrudability tests for mixes containing coarse aggregates

Mix	Desorptivity (mm/s$^{\frac{1}{2}}$)	I_{norm}	Extrudability
Control	0.037	0.03	Pass
CA15	0.041	0.04	Pass
CA30	0.045	0.04	Pass
CA45	0.057	0.06	Fail

4.3.4 Uniaxial compression tests to assess buildability

The results of the preceding section indicate that the maximum coarse aggregate (LECA) content which can be introduced without affecting extrudability was 30 % by volume of total aggregates (CA30 mix). To examine the effect on buildability, CA30 and the control mix were subjected to uniaxial compression tests. The load vs displacement graph for the control mix obtained at different ages is shown in Figure 4.9. For relatively younger specimens, i.e., for specimens with ages from 0 to 180 min (see Figure 4.9a), the load value is found to increase linearly with the displacement until it reaches a certain plateau, and thereafter the load nearly remains constant or increases at a much slower rate. On the other hand, for the older specimens with ages from 240 to 420 min (see Figure 4.9b), the load value is found to decrease beyond this plateau indicating a softening type behaviour. These results have also been observed by other researchers (Voigt *et al.*, 2006; Wolfs *et al.*, 2018; Panda *et al.*, 2019). Using the transverse displacement measured at each point, an area correction was applied to convert the load-displacement to the corresponding stress-displacement graphs as shown in Figure 4.10. It can be seen that the stress response of the younger specimens (Figure 4.10a) exhibits an elasto-plastic type behaviour. The stress increases to a certain yield point and thereafter, there is an onset of continuous plastic deformation. On the other hand, older specimens (Figure 4.10b) exhibit a strain-softening type response, more typical of hardened concrete. This difference in the material behaviour is also evident in the type of failure modes observed in the younger and older specimens. For instance, Figures 4.11a and 4.11b show the failure modes of specimens at age of 0 min and 420 min respectively. In can be seen that in the former, there is a continuous plastic deformation exhibiting a barrelling type failure. No shear cracks could be observed during the failure. On the contrary, for the latter case, the specimen fails by the formation of shear cracks similar to the behaviour of hardened concrete.

The load displacement and the corresponding stress-strain graphs for the CA30 mix are shown in Figures 4.12 and 4.13 respectively. The trends are similar to that of the control mix, i.e., the stress-displacement response changes from am elasto-plastic to the strain-softening type response as the material ages. The compressive strength obtained at different ages and the modulus of elasticity calculated at 2.5 % strain (which is within the the linear elastic regime of stress-displacement curve) are shown in Figures 4.14

and 4.15 respectively. Clearly, it can be seen that for both the younger (Figures 4.14a and 4.15a) and the older (Figures 4.14b and 4.15b) specimens, the compressive strength and elastic modulus values are higher for CA30 by about 45-60 % and 25-50 % respectively. The reason for this can be attributed to the more amount of dewatering that happens in the CA30 as compared to the control mix. As seen in the flow values presented in Table 4.7, the dewatering resulted in a relatively stiffer mix after the extrusion process. Therefore, although the dewatering and the subsequent loss of workability can be detrimental to the extrusion process, this results in the improvement of the buildability of concrete.

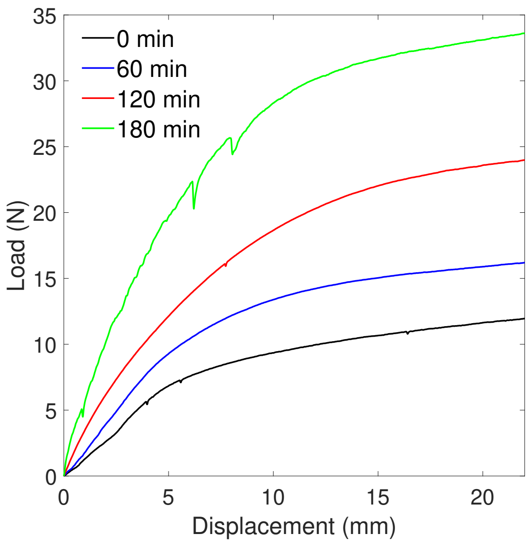

(a)

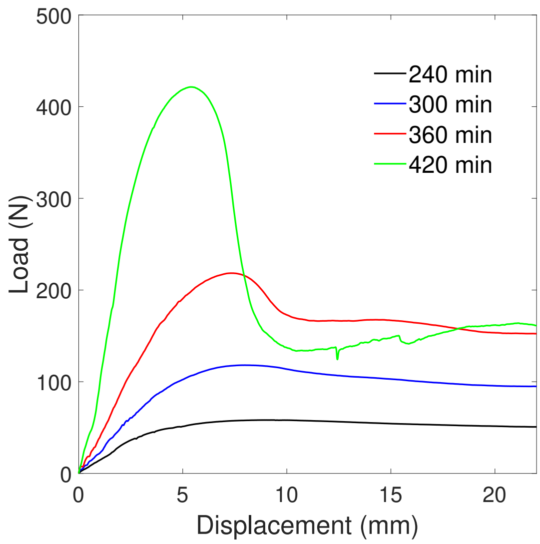

(b)

Figure 4.9: Load vs displacement graph for control mix at different ages from (a) 0 to 180 min (b) 240 to 420 min

Another aspect that needs to be brought to attention is the evolution rate of compressive strength and elastic modulus. For both the mixes, the strength and modulus evolve slowly and linearly for the younger specimens, whereas a more rapid evolution can be observed in the older specimens. These results are similar to the previous study by Voigt *et al.* (2006) on extrudable cement composites. This trend can be explained based on the microstructural development in cementitious systems. At early ages, most of the hydrates formed are the needle-shaped ettringite crystals. Its formation do not contribute much towards increasing the compressive strength of the concrete. At later ages, C–S–H gel starts to form, connecting the particles together and resulting in a more rigid framework (Mehta and Monteiro, 2006). Therefore at later ages, there is a more rapid increase in strength due to the formation of C–S–H gel. This difference can also be observed in the failure modes of the younger and older specimens (Figures 4.11a and 4.11b respectively). The younger specimens showed a barrelling type failure without the formation of any shear cracks. On the other hand, for the older specimens, shear cracks can be clearly seen indicating the breakage of a more rigid connection of particles.

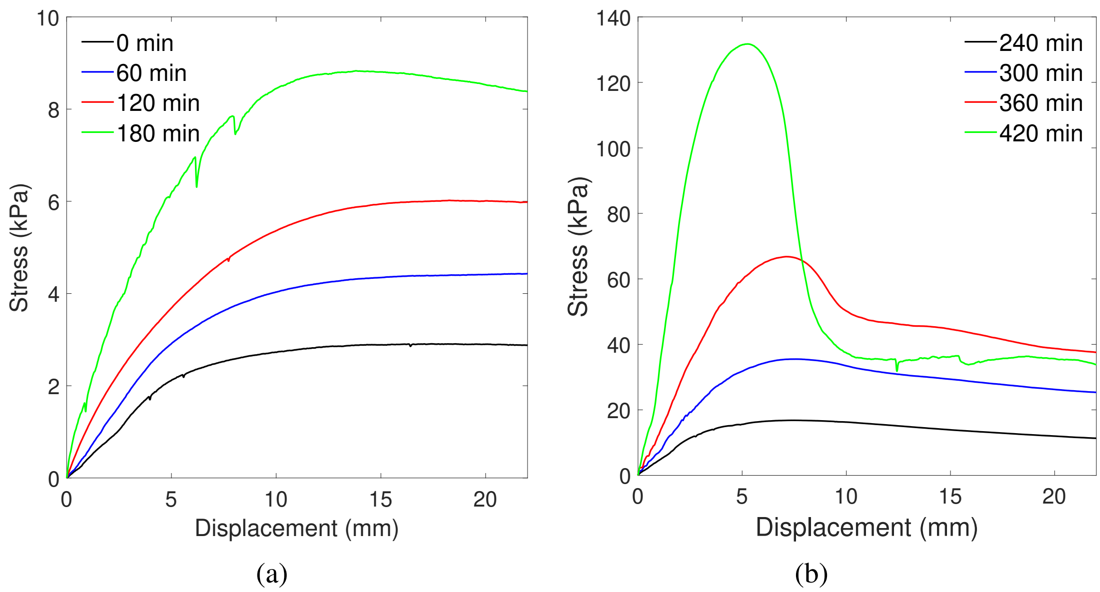

Figure 4.10: Stress vs displacement graph for control mix at different ages from (a) 0 to 180 min (b) 240 to 420 min

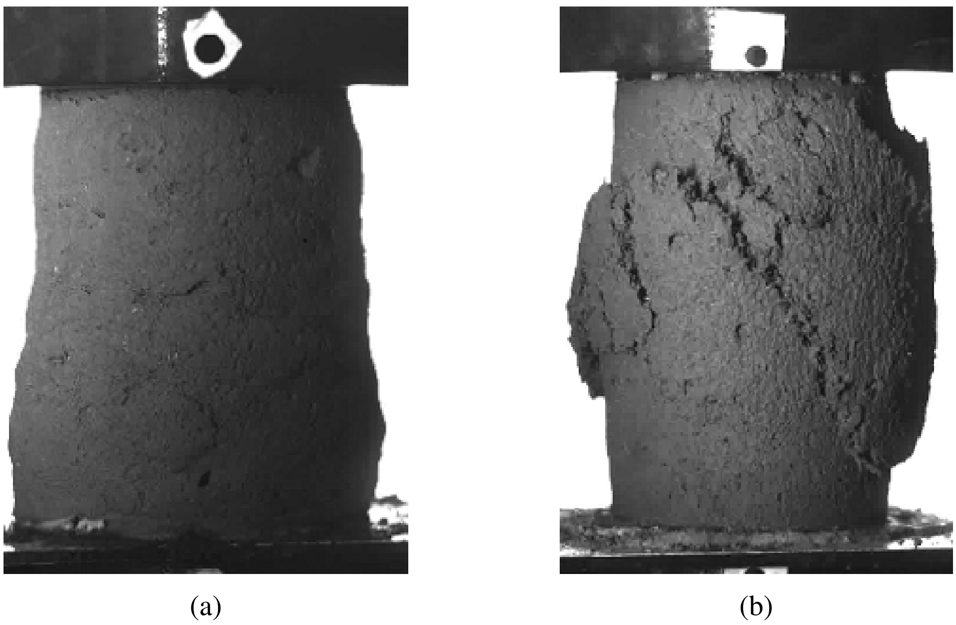

Figure 4.11: Failure modes of control mix specimen at the age of (a) 0 min (b) 420 min

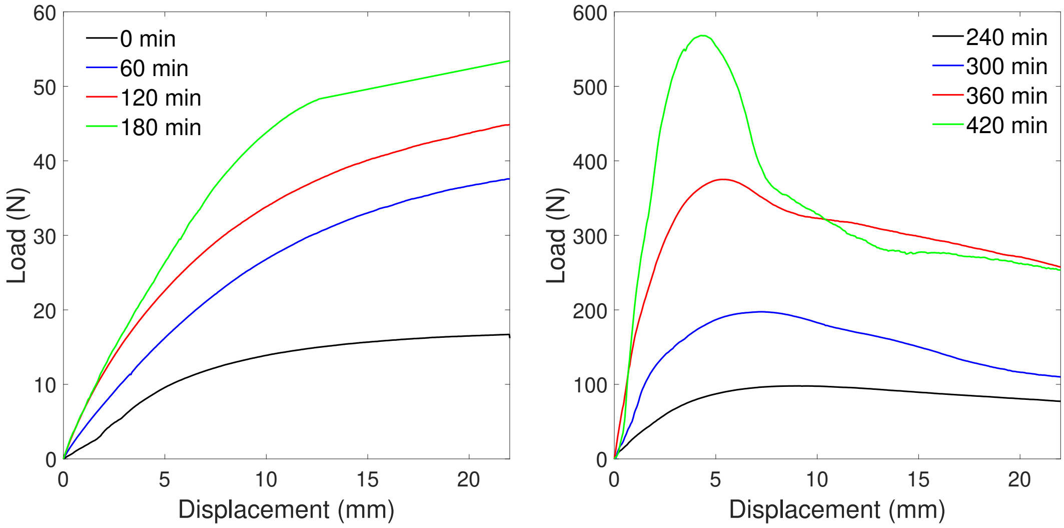

(a) (b)

Figure 4.12: Load vs displacement graph for CA30 at different ages from (a) 0 to 180 min (b) 240 to 420 min

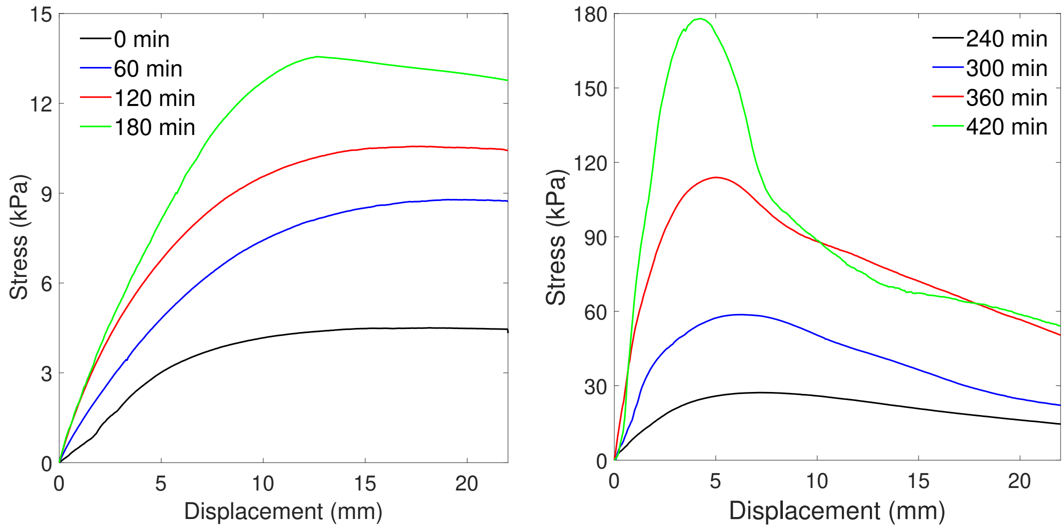

(a) (b)

Figure 4.13: Stress vs displacement graph for CA30 mix at different ages from (a) 0 to 180 min (b) 240 to 420 min

To describe the transition from the linear to exponential evolution for strength and elastic modulus, a model with a similar form to that proposed by Perrot *et al.* (2016) can be used. The model is given by

$$\tau_c(t) = A_1 t_1 \left(e^{\frac{t}{t_1}} - 1\right) + \tau_c(t=0) \tag{4.4}$$

$$E(t) = A_2 t_1 \left(e^{\frac{t}{t_2}} - 1\right) + E(t=0). \tag{4.5}$$

In the above expression, $\tau_c(t)$ and $E(t)$ represent the compressive strength and elastic modulus respectively at any time t. A_1, t_1, A_2 and t_2 are the model parameters.

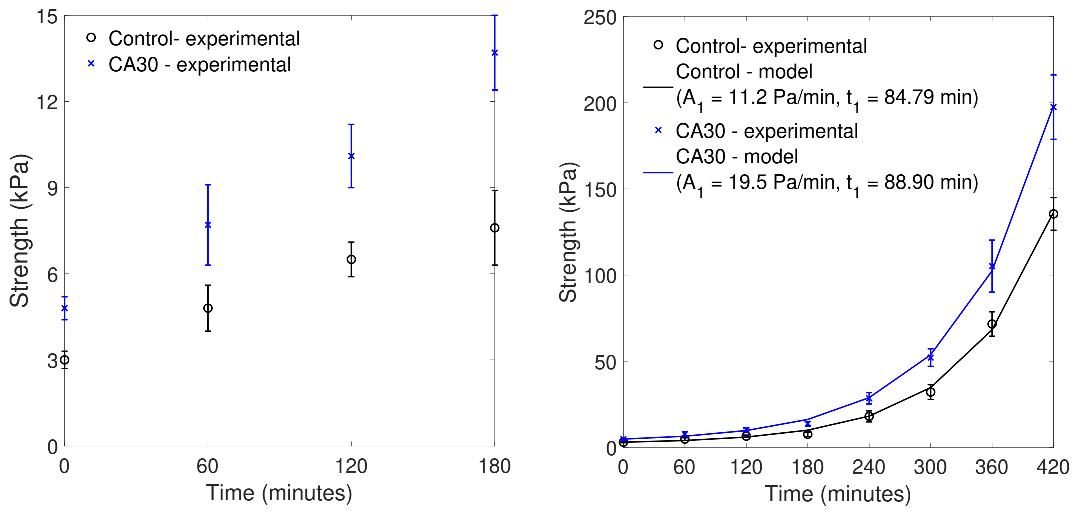

(a) (b)

Figure 4.14: Evolution of $\tau_c(t)$ for ages from (a) 0 to 180 min (b) 0 to 420 min

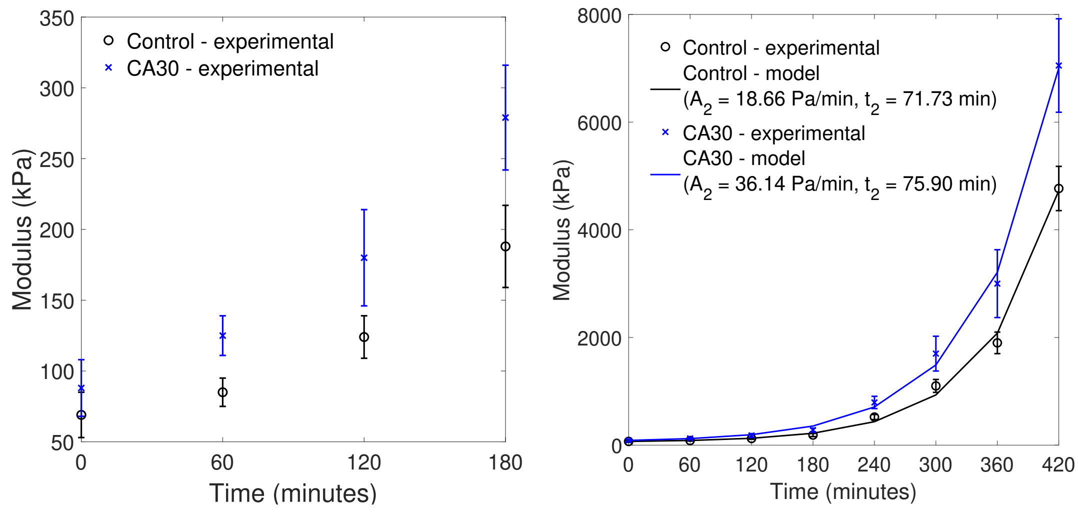

(a) (b)

Figure 4.15: Evolution of $E(t)$ for ages from (a) 0 to 180 min (b) 0 to 420 min

Finally, the results from the uniaxial compression tests can be used to predict the occurrence of both plastic and buckling type failure during the printing process. A plastic collapse occurs if the vertical stress in the bottom layer at any time t exceeds the compressive strength of the material. The vertical stress in the bottom layer, $\tau_v(t)$ can be given by

$$\tau_v(t) = \rho g h. \tag{4.6}$$

In the above equation, ρ represents the density of concrete, g is the acceleration due to gravity and h is the total print height of the element. If the strength of the material in the bottom layer is given by $\tau_c(t)$, then the critical height, H_c at which plastic collapse may occur is given by

$$H_c = \frac{\tau_c(t)}{\rho g}. \tag{4.7}$$

The form of the above expression suggests that the critical height is directly proportional to the strength of the material in the bottom layer at the given time and inversely proportional to the density of the concrete. For CA30 mix, the compressive strength is higher by 45-60 % (as seen in Figure 4.14). Further, as seen in Table 4.1, the density of CA30 is lower by 7 % as compared to the control mix. Hence, from Equation (4.7), it can be found that the critical height increases by 56-72 % for CA30 mix as compared to the control mix.

To assess the occurrence of buckling type failure, the equation proposed by Roussel (2018*b*) can be used. The critical height for buckling failure to occur is given by

$$H_c = \left(\frac{8E(t)I}{\rho g A}\right)^{\frac{1}{3}}. \tag{4.8}$$

In the above equation, $E(t)$ represents the elastic modulus at any time t. Moment of inertia (I) and cross-sectional area (A) are the section properties. It can be seen that the critical height is proportional to $\left(\frac{E(t)}{\rho}\right)^{\frac{1}{3}}$. Since, E(t) for CA30 is higher by 25-50 % (as seen in Figure 4.15), and the density is lower by 7 %, it can be found that the critical height increases marginally by 10–17 % for CA30 mix as compared to the control mix.

Although Equations (4.7) and (4.8) provide a rough estimate of the critical height for plastic and buckling type failure, a more accurate analysis can be made by using numerical modelling. Further, experimental studies of the printing process with digital image correlation can give further insights about the failure modes. Such prediction models can be particularly useful in large-scale additive manufacturing operations. In such cases, evaluating failure by performing printing trials becomes difficult due to the large amount of material, time and effort required. In the current study, uniaxial compression tests were conducted for ages from 0 to 420 min. This large timescale of 0–420 min was decided keeping in mind the relatively larger timescale involved in executing such projects. For experimental validation of the failure models, the printing must be performed with a large-scale 3D printer having a longer time-gap between layer depositions. Since this was not possible using the laboratory-scale 3D printer system, print failure was not experimental assessed.

4.4 Summary

In this chapter, the concerns associated with scaling-up to a larger 3D printer system were addressed. A desorptivity based approach was introduced for assessing the phase separation of printable mortars to be used in high pressure extrusion systems. The dosage of methylcellulose decreased the desorptivity and therefore, increased the resistance to phase separation. Further, printable mixes were developed with the inclusion of LECA as coarse aggregates. The effect of LECA addition on extrudability and buildability of printable concrete were examined. It was found that increasing the coarse aggregate content increased the desorptivity, thereby decreasing the water retention capacity. Mixes with up to 30 % volume substitution with coarse aggregate were extruded successfully. To assess the effect of coarse aggregate on buildability, uniaxial compression tests were carried out on concretes after different ages of casting. For both the mixes with and without coarse aggregates, the material behaviour changed from an elasto-plastic type response at early ages to a strain-softening type response (typical of hardened concrete) at later ages. At any given age, it is found that the addition of LECA increased both the strength and elastic modulus of the concrete. The reason for this can be attributed to a higher amount of dewatering that occurs during the extrusion process for the mixes with the coarse aggregate. Finally, discussions were provided on the effect of using low density aggregates like LECA in improving the resistance to both plastic and buckling type collapse that may occur during printing.

A modular demo structure and concrete furniture elements were 3D printed by using the control mix developed in this chapter. The details of the construction are illustrated in Appendix A.

CHAPTER 5

MECHANICAL PROPERTIES OF 3D PRINTABLE CONCRETE

5.1 Introduction

In Chapters 3 and 4, the discussions were made only with respect to fresh properties of 3D printable concrete. This chapter focuses on developing test methods which can be used for the characterization of the mechanical behaviour of 3D printed elements. Based on the strength values obtained from the different tests conducted, a procedure is suggested for its structural design. The study comprises of two stages. In the first stage, the interface of printed concrete is examined. The porosity of the printed concrete is determined at the bulk, vertical and horizontal interfaces, and compared with that of mould cast concrete. The strength at the vertical and horizontal interface is further characterized by conducting a bond shear test. The bond strength is compared to the shear strength of mould cast concrete. In the second stage of study, the anisotropy of the printed specimens and its reasons are examined by testing cubes and beams cut out from a 3D printed wall prototype. Comparisons are made with respect to the strength values of mould cast concrete. Finally, based on the results obtained from the study, perspectives on the structural design of a 3D printed wall element are provided.

5.2 Materials and methods

5.2.1 Mixes used

The mixture formulations made for small-scale test bed printer, SF, NC and VM mixes (see Table 3.5) were used in the studies for mechanical characterization. These mixture formulations were designed to have buildability when printed with a rectangular nozzle of 30 $\times$ 20 mm. However, an increased nozzle size of 30 $\times$ 30 mm was used for the printing of elements for mechanical characterization. To ensure buildability with the increased nozzle size, the superplasticizer dosage was adjusted based on the procedure illustrated in Chapter 3. The new dosages of superplasticizers were 1.35, 0.99 and 1.41 kg/m^3 for SF, NC and VM respectively.

5.2.2 Preparation of test specimens

The mould cast cube and beam specimens were prepared in accordance with ASTM C109 / C109M-16a (2016) and ASTM C348-14 (2014) respectively. For the testing of printed concrete, specimens were cut out from a 3D printed wall prototype (the details on the extraction of specimens for the different tests are explained in Sections 5.2.3 to 5.2.6). It should be noted that cutting may induce additional microcracks in the specimens which may adversely affect the strength. To keep such effects to a minimum, a diamond saw cutter suitable for cutting thin sections was used in extracting the specimens. The wall prototype consisted of two horizontal and six vertical layers. The bond strength between the layers of a printed concrete element can depend on time gap between the deposition of the layers (Panda *et al.*, 2018; Le *et al.*, 2012*b*; Panda *et al.*, 2017*a*). As explained previously in Chapter 3, the long-term objective of the research program at IIT Madras was to develop a layer- wise extrudable mixture for the additive manufacturing of a 1.52 x 1.13 m toilet module that is to be fabricated using a printer that can manufacture full-scale structures. Considering a horizontal print speed of 44 mm/s and assuming that there are two horizontal layers for the wall, the time gap between two successive horizontal and vertical layers will be 2 and 8 minutes respectively. Therefore, the wall prototype was also printed maintaining this same time gap between the layers.

The different stages in the printing process of the wall prototype are schematically shown in Figure 5.1. At first, a single filament of length 240 mm was extruded (Figure 5.1a). After this the nozzle was moved horizontally by 30 mm (width of the nozzle) and an adjacent horizontal layer was printed next to the first layer (Figure 5.1b) after a time gap of two minutes. Following this, the nozzle was raised by 30 mm (height of the nozzle) and horizontally moved to align on top of the first layer. A vertical layer was deposited on top of first layer after a total time gap of eight minutes after the deposition of the first layer (Figure 5.1c). This process was continued until the entire specimen comprising of six vertical and two horizontal layers was printed (Figure 5.1d). Since the height of the nozzle was 30 mm, the expected height of the wall prototype having six vertical layers was 180 mm. But 2-3 % compression was observed in the wall prototype for all the mixes. The average heights of wall prototype were 176.3 $\pm$ 1.1, 175.8 $\pm$ 1.3 and 175.1 $\pm$ 1.4 mm for SF, NC and VM mix respectively.

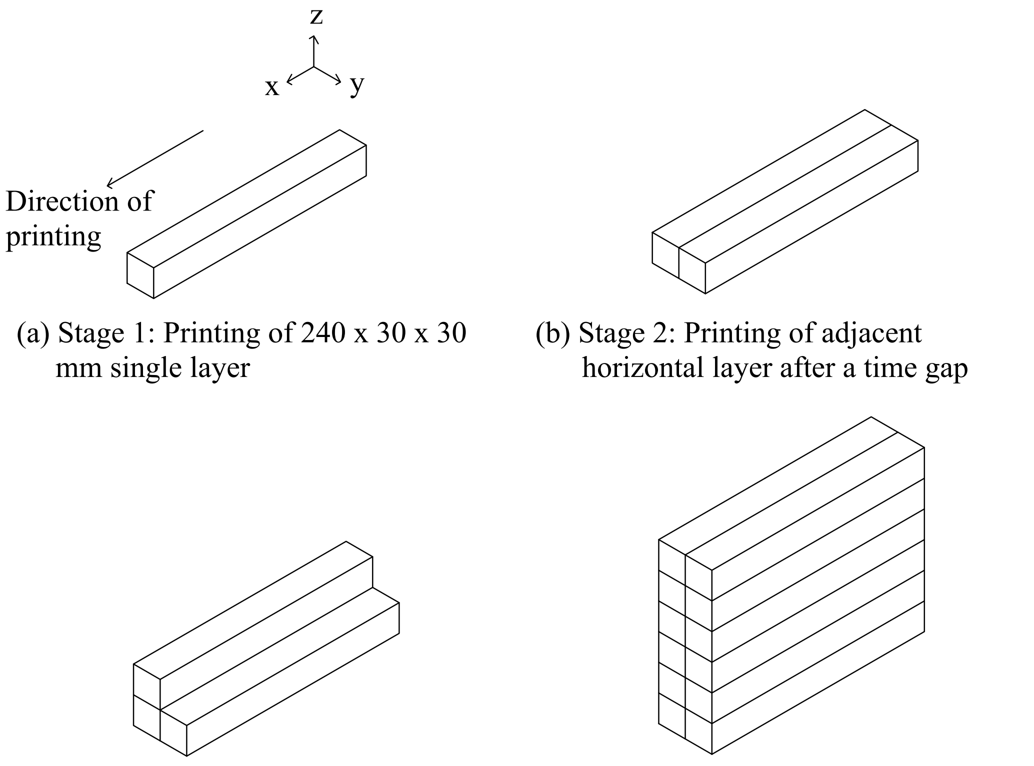

(a) Stage 1: Printing of 240 x 30 x 30 mm single layer

(b) Stage 2: Printing of adjacent horizontal layer after a time gap

(c) Stage 3: Printing of vertical layer on top of the first layer after a time gap

(d) Wall element comprising of six vertical and two horizontal layers

Figure 5.1: Different stages in the printing of the wall element

5.2.3 Determination of porosity

For both mould cast and printed concrete, porosity was determined by using 20 $\times$ 10 $\times$ 10 mm specimens. For the mould cast concrete, the specimens were cut out from 50 $\times$ 50 $\times$ 50 mm cubes. Four specimens were assessed and the average value was reported. For the printed concrete, a total of two wall prototypes were printed to obtain two specimens each from locations 1 to 6 (shown in Figure 5.2). The assessment of porosity was made at the bulk, horizontal and vertical interfaces of the wall element. For the assessment of porosity in the bulk concrete, the specimens cut out vertically from the location 3 and 4 were used. For the interface between two horizontal layers, the specimens extracted vertically from the locations 1 and 2 were used. For the interface between two vertical layers, specimens extracted horizontally from the locations 5 and 6 were assessed.

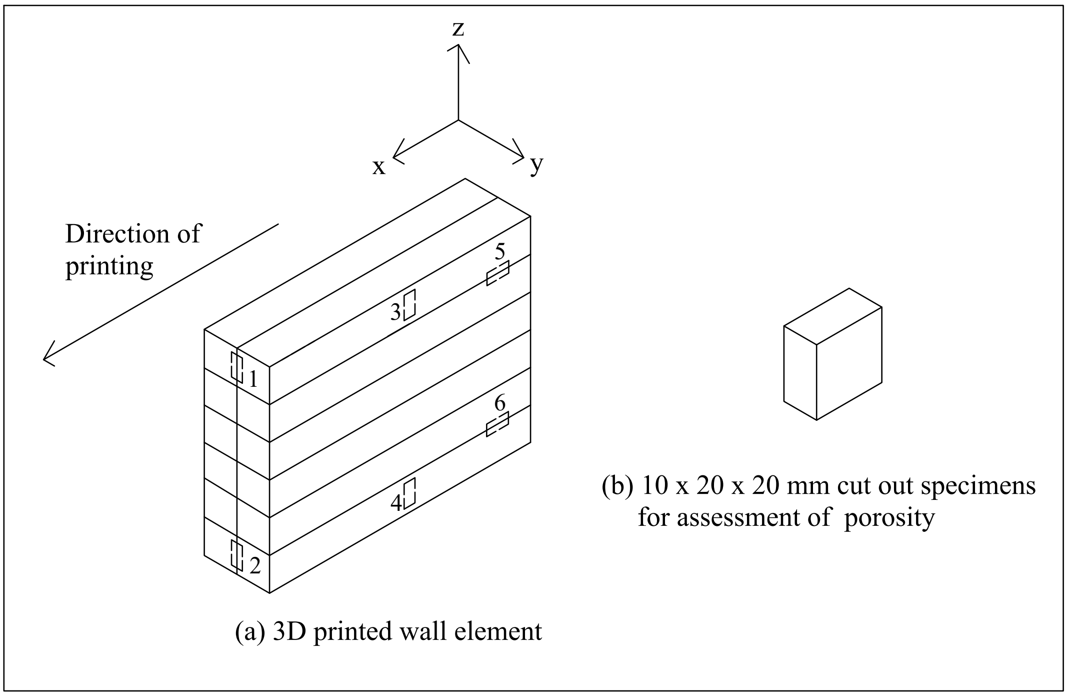

Figure 5.2: Extracting specimens from the wall element for the assessment of porosity

The determination of porosity was by the vacuum saturation method. The specimens were first oven-dried at 50 °C for seven days. After this, they were placed in a vacuum desiccator for 3 hours to remove any excess moisture and also to allow the specimens to cool to the room temperature (25 - 30 °C). Following this, the specimens were kept immersed in the desiccator filled with calcium hydroxide solution and maintained under vacuum. After one hour the vacuum was released and the specimens were kept immersed in the solution for another duration of 18 hours. The vacuum saturated porosity (ρ) is given by

$$\rho = \frac{M_1 - M_2}{M_1 - M_3} \times 100. \tag{5.1}$$

In the above equation, M_1 is the mass of the saturated specimen in air, M_2 is the mass of the dried specimen in air and M_3 is the mass of the saturated specimen in water. Similar methods has been previously used by other researchers to determine the porosity of cementitious materials (Bu *et al.*, 2014; Dhandapani and Santhanam, 2017).

5.2.4 Determination of bond strength

Cylindrical specimens having 25 mm diameter and 40 mm height were used for the bond shear test. The locations from which specimens were extracted by coring from the wall element are shown in Figure 5.3. For characterizing the interface between horizontal layers, six cylindrical specimens each were cut out horizontally from location 1 and 2. Similarly for the vertical layers, six specimens each were cut out vertically from location 3 and 4. Cylindrical specimens were also cut out from $50 \times 50 \times 50$ mm mould cast cube specimens to assess the shear strength of mould cast concrete.

Direct bond shear test methods are used to determine the strength of overlay materials (Leutner, 1979). For the current study, a direct bond shear test was performed on the cut out specimens by using a Zwick Roell testing machine fitted with a 5 kN load cell. The fixture for bond shear test is shown in Figure 5.4. With the interface at the centre, the cylindrical specimen is placed horizontally in the grooves of upper and lower jaws of the fixture. The jaws are then pulled apart at a constant displacement rate of 0.1 mm/minute. The failure load is divided by the cross-sectional area of the cylinder to obtain the bond shear strength. The cylindrical specimens cut out from mould cast cubes were also tested in a similar manner to obtain the shear strength of mould cast concrete.

5.2.5 Determination of compressive strength

The compressive strength was determined by using $50 \times 50 \times 50$ mm cubes. For printed concrete, six cubes were cut out from the wall element and tested in three different loading direction (D1, D2 and D3) as shown in Figure 5.5. The locations from where the cubes were extracted are shown in Figure 5.6. Since the width of wall element was 60 mm and the required width of cube was 50 mm, a slice of 5 mm was removed from both sides to cut out the cubes from the locations shown in Figure 5.6. The locations 1 and 2 were used to obtain cubes for loading along D1 direction while locations 3 and 4, and locations 5 and 6 were used for loading along D2 and D3 directions respectively. Six wall prototype elements were printed such as to obtain a total of twelve cubes each for the three loading directions. Twelve cubes of 50 × 50 × 50 mm size were also prepared in standard moulds. For both the printed and mould cast cubes, the loading rate and testing procedure was in accordance with ASTM C109 / C109M-16a (2016).

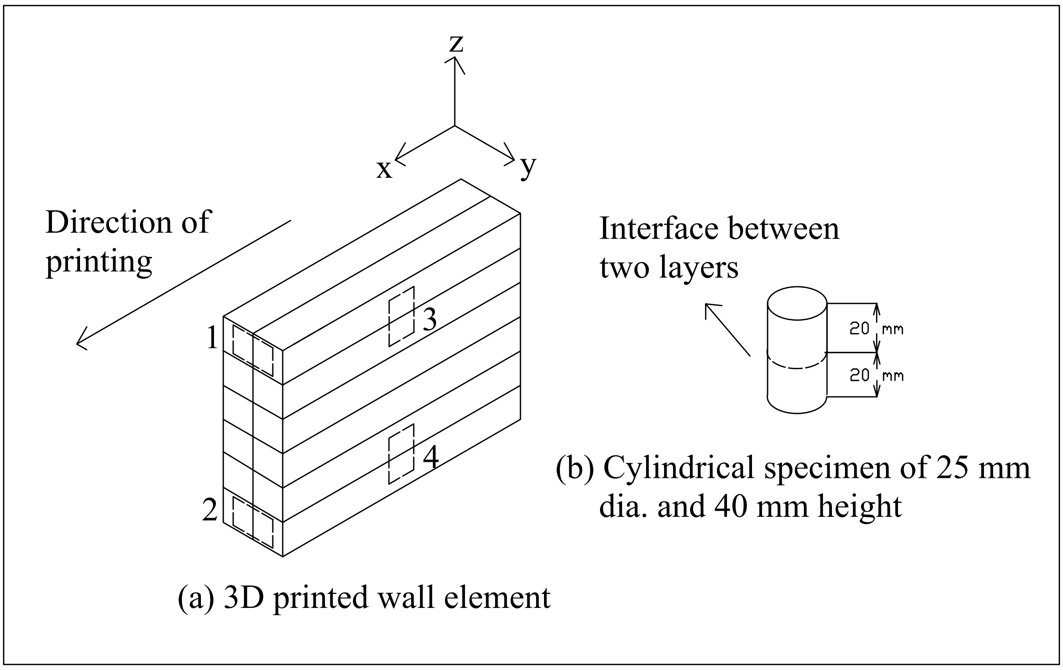

Figure 5.3: Extracting specimens from the wall element for bond shear test

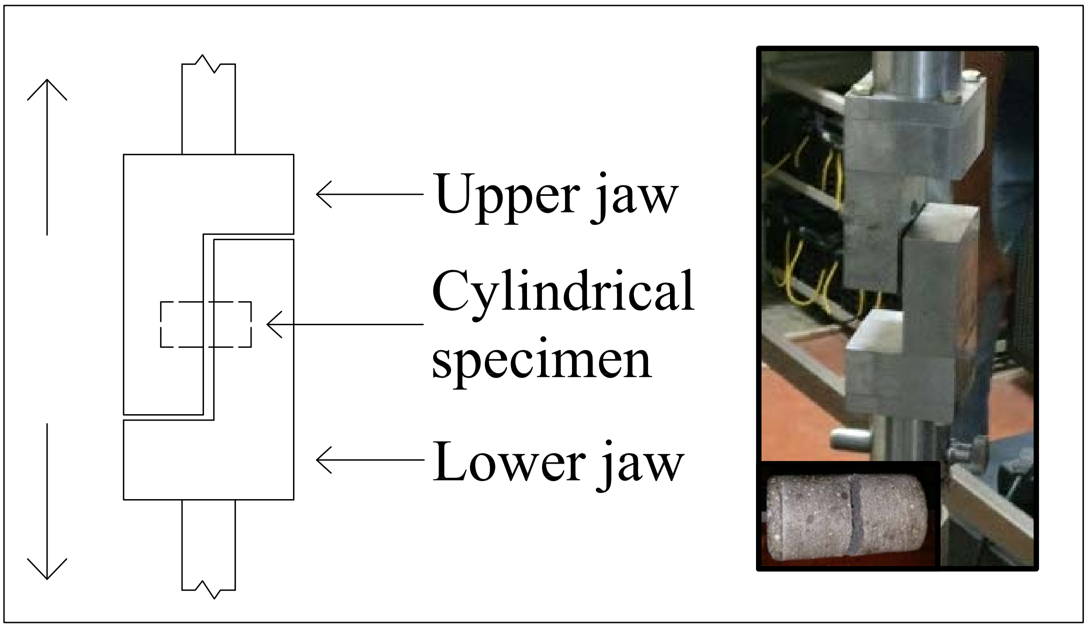

Figure 5.4: Fixture for bond shear test

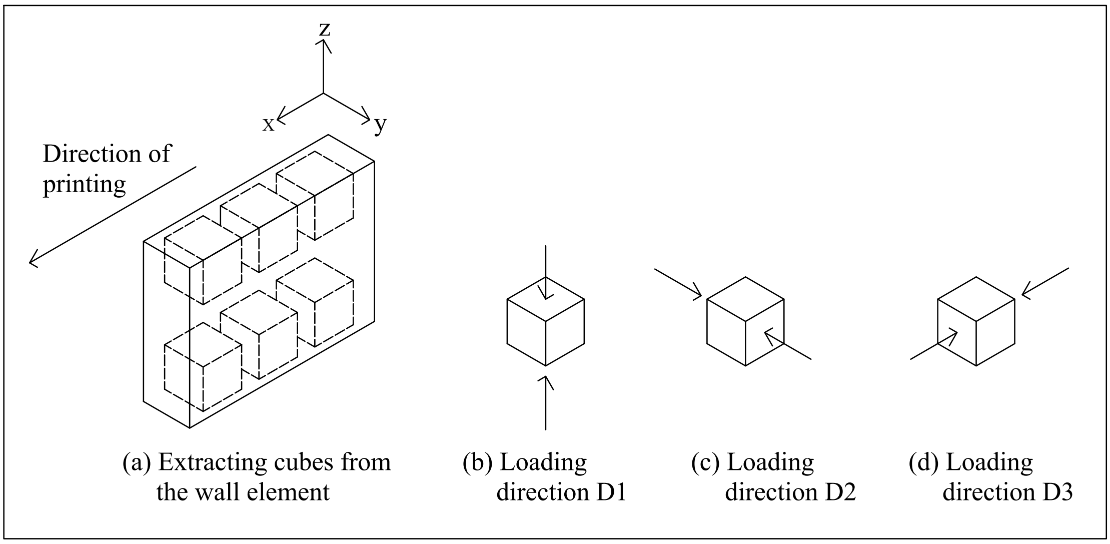

Figure 5.5: Different loading directions for compression test

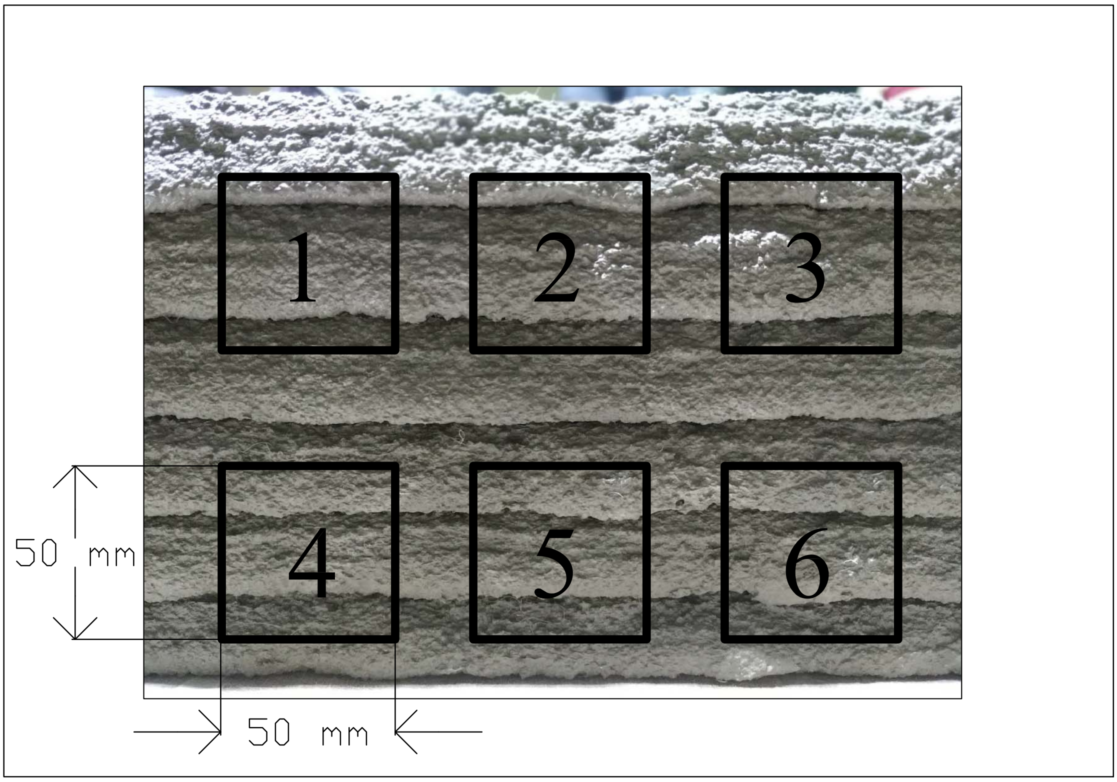

Figure 5.6: Extracting cubes from the wall element for compression test

5.2.6 Determination of flexural strength

The flexural strength was determined by a three-point bending test using 160 $\times$ 40 $\times$ 40 mm beams. The mould cast beams were prepared in standard moulds. For printed concrete, beams were cut out from three different locations as shown in Figure 5.7. Since the width of wall element was 60 mm and the required width of beams was 40 mm, a slice of 10 mm was removed from both sides to cut out the beams from locations indicated in Figure 5.7. When subjected to a horizontal load, a vertical wall can undergo bending in a vertical plane as shown in Figure 5.8b. For reference, the bending in this direction will be denoted by E1. The bending along E1 direction was assessed by using the vertically cut out beams from location 1. Under a horizontal load, a vertical wall can also bend in a horizontal plane as indicated in Figure 5.9b. The bending along this direction (E2 direction) was assessed by using beams extracted from locations 2 and 3. In addition to directions E1 and E2, the beams extracted from location 2 and 3 were also tested along E3 direction as shown in Figure 5.9c. A total of twelve wall elements were printed and three beams were extracted from each of them (Figure 5.7). The twelve vertically cut out beams were used for the loading along E1 direction. Twelve beams (comprising of 6 from location 2 and six from location 3) each were used for the testing along E2 and E3 directions. The test procedure and the loading rate were in accordance with ASTM C348 ASTM C348-14 (2014).

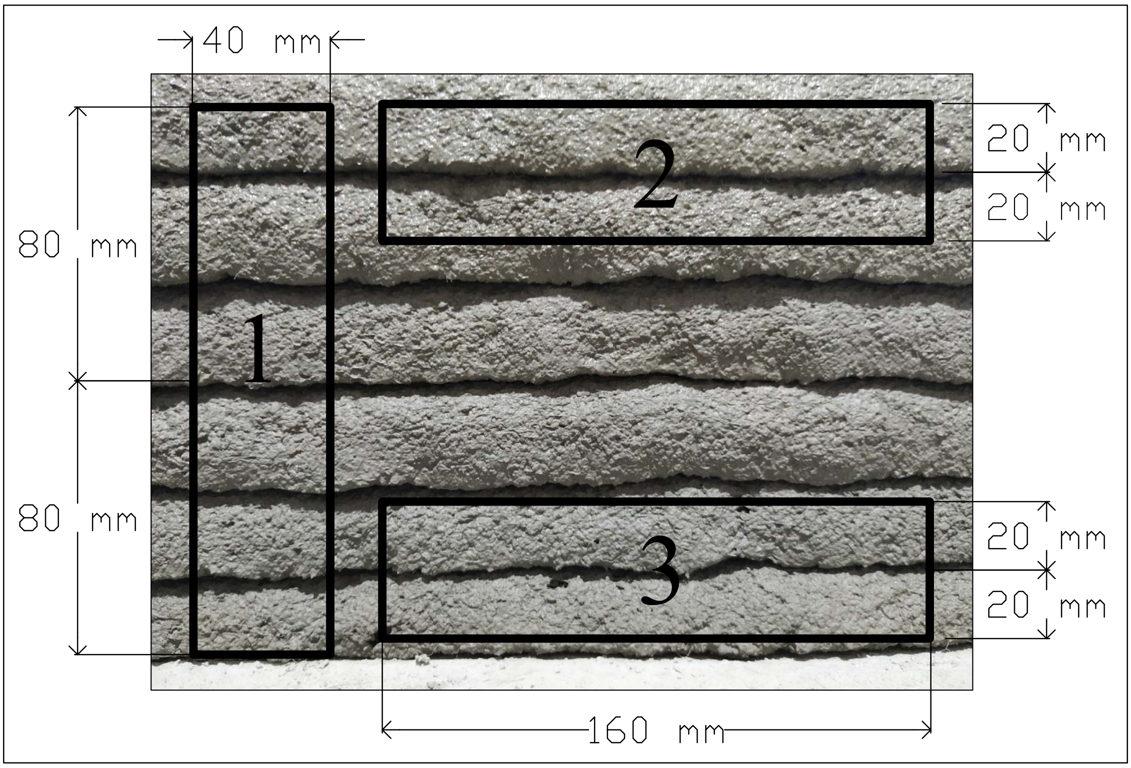

Figure 5.7: Extracting beams from the wall element for flexural test

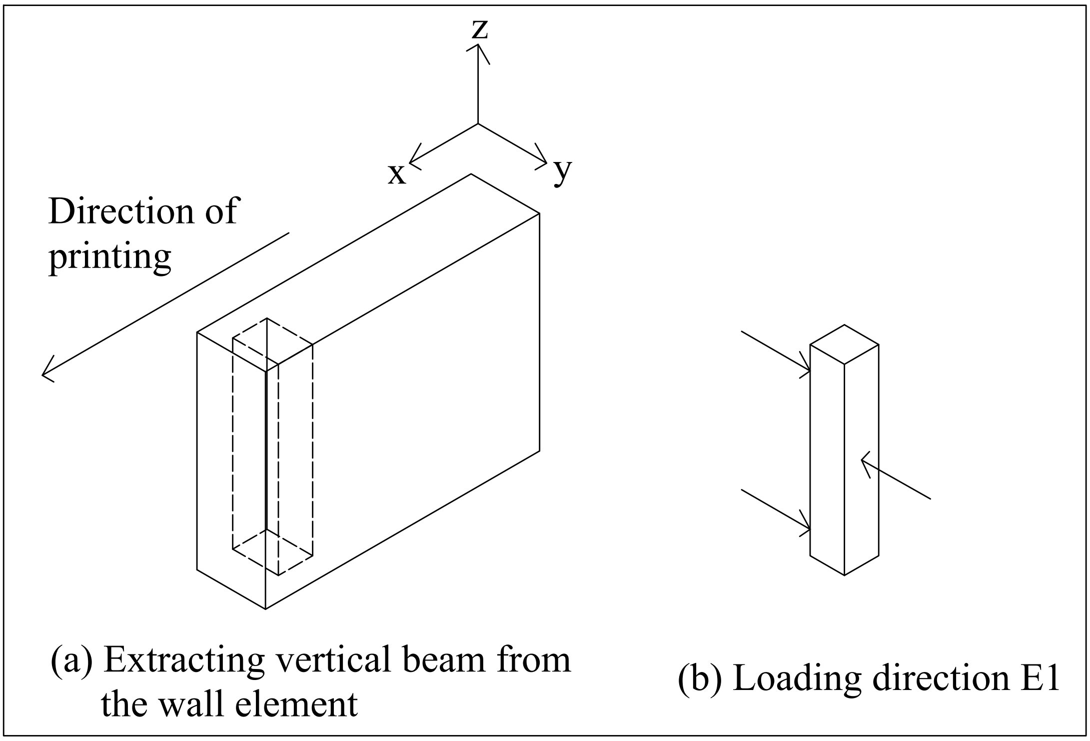

Figure 5.8: Loading direction for vertically cut out beams

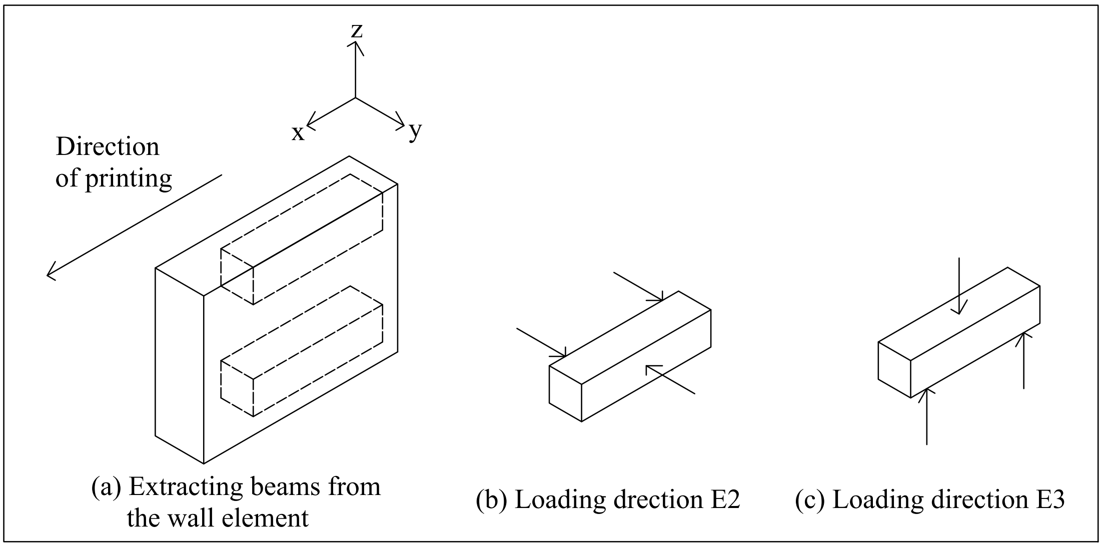

Figure 5.9: Loading direction for horizontally cut out beams

5.3 Results and discussions

5.3.1 Porosity

The porosities determined for the three mixes are shown in Figure 5.10. Compared to the mould cast concrete, the porosity of the specimens extracted from the interface between horizontal layers was found to be higher by 13.3, 12.9 and 11.5 % for SF, NC and VM mixes respectively. Likewise, for the specimens extracted from the interface between vertical layers, the porosity was higher by 15.3, 11.9 and 10.6 % respectively. Also, as seen in Figure 5.10, the porosity was found to be similar for both vertical and horizontal interfaces. The higher porosities indicate weak joints being formed at the interface of the printed concrete specimen. Contrary to this, for the specimens extracted from the bulk of the printed concrete, the porosity was found be lower by 7.1, 6.9 and 7.3 % as compared to mould cast concrete for SF, NC and VM respectively. This reduced porosity observed in the bulk concrete may be because of a higher compaction and packing achieved during the extrusion process.

Therefore, for the time gap and other print parameters used in the current study, a 3D printed element has a more densified bulk but a more porous interface compared to a monolithic element made with the same concrete. This higher porosity at the interfaces may result in a relatively lower compressive and flexural strength for printed elements as will be seen in the subsequent sections.

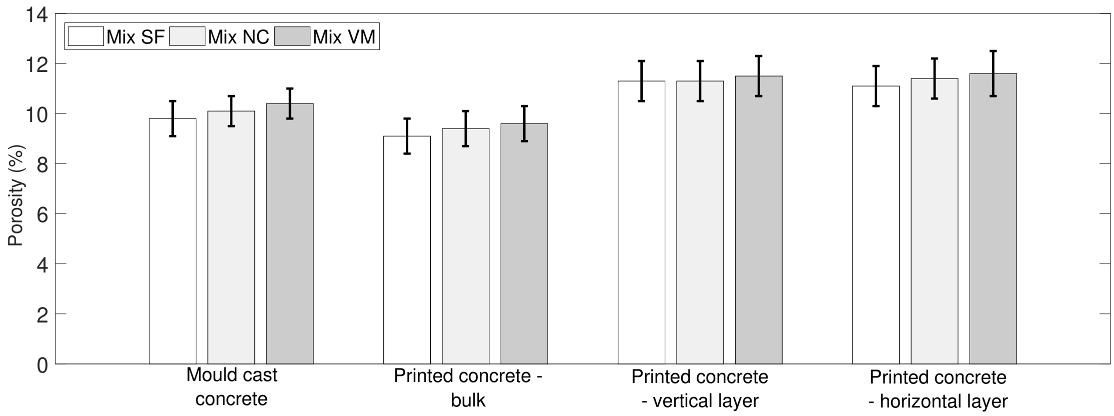

Figure 5.10: Comparison of porosities in the bulk and interfaces of printed concrete with that of mould cast concrete

5.3.2 Bond shear test

The results of the bond shear tests are shown in Figure 5.11. Compared to the shear strength of the respective mould cast concrete, the bond shear strength between vertical layers were found to be lower by 29.2, 26.4 and 22.5 % for SF, NC and VM mix. For the interface between horizontal layers, the reduction in strength was 24.3, 24.1 and 24.1 % respectively. This further indicates a weaker joint formed at the vertical and horizontal interfaces. These results are in agreement with the trends observed in the porosity measurements.

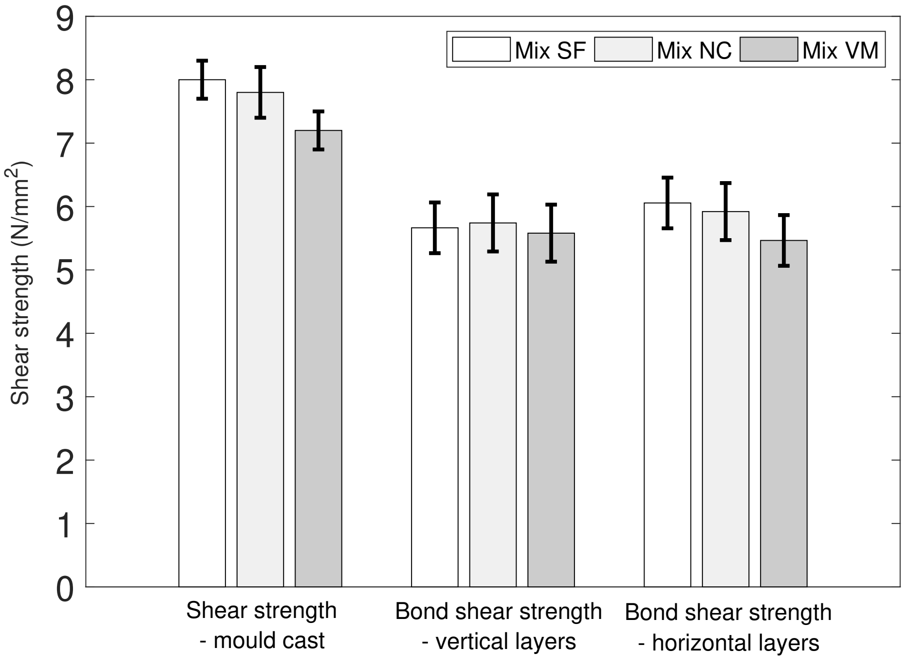

Figure 5.11: Comparison of bond shear strength with shear strength of mould cast concrete

It is to be noted that the bond strength can depend on the print parameters, especially the time gap between the deposition of layers (Panda *et al.*, 2018; Le *et al.*, 2012*b*; Panda *et al.*, 2017*a*). For the current study, the time gap between two horizontal layers was two minutes while it was eight minutes for the vertical layers. In an earlier study, Le *et al.* (2012*b*) conducted tensile bond tests on printed concrete elements and found a strength reduction of about 23 % for time gaps of 0 and 15 minutes. This reduction is similar to the values observed in the current study. Also, it is to be noted that preventing drying can reduce the strength reduction at the interface (Roussel, 2018*a*; Sanjayan *et al.*, 2018). However, for the current study no specific care was taken to control drying of the layers.

All experiments were conducted at the ambient conditions of 30 °C and 70 % relative humidity.

5.3.3 Compressive strength

The results of the compressive strength tests are shown in Figure 5.12. For all the loading directions (D1, D2 and D3), the compressive strength of the printed concrete was lower as compared to the mould cast concrete. For the loading direction D1, the strength was lower by 16.5, 14.2 and 12.8 % for SF, NC and VM mix respectively. The strength decrease along D2 direction was 19.3, 18.6 and 15.5 % while along D3 direction, it was 21.3, 19.6 and 16.5 %.

The decreased compressive strength observed for the printed specimens can be explained as being due to presence of weaker interfaces with increased porosities existing between layers. Under a compression load, cracks may initiate from these weaker interfaces causing the printed concrete to fail at relatively low stress levels as compared to mould cast concrete specimens. As seen in Figure 5.12, the compressive strength values obtained along D1, D2 and D3 are similar. Hence, no anisotropic behaviour was seen in the printed concrete when subjected to compression.

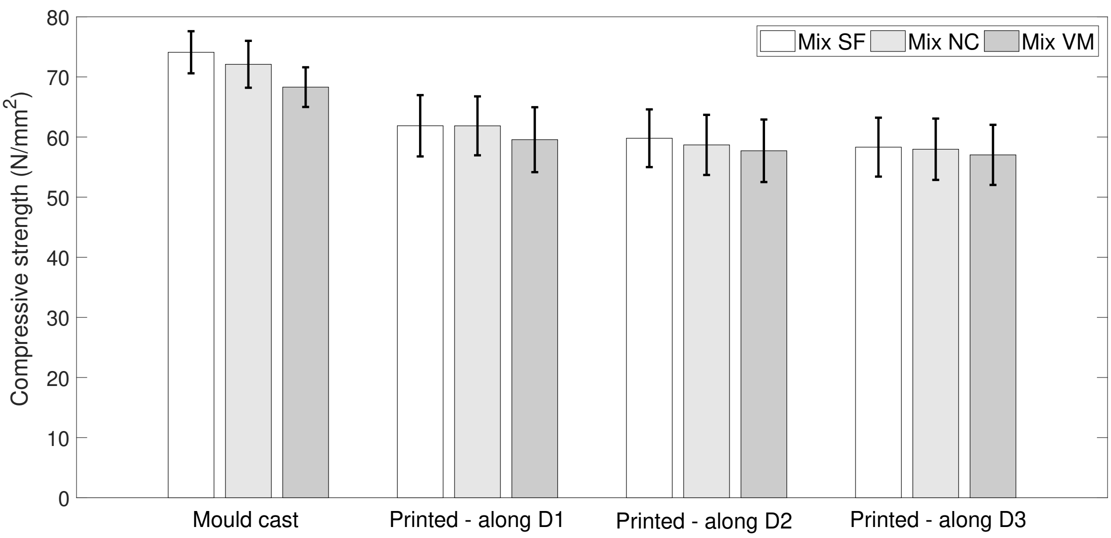

Figure 5.12: Comparison of compressive strength of printed concrete with that of mould cast concrete

5.3.4 Flexural strength

The results of flexural strength tests are shown in Figure 5.13. The flexural strength was found to decrease only when tested along E1 direction. The strength decreased by 40, 35.8 and 32.9 % for SF, VM and NC mix respectively. On the other hand, when tested along E2 and E3 directions, the flexural strength was found to increase. The increase when tested along E1 direction was 13.1, 14.2 and 15.5 % and when tested along E3 direction, it was 18.1, 18.8 and 19.5 % respectively for SF, VM and NC mix. These results indicate that printed concrete elements exhibit anisotropic behaviour in flexure.

The reason for this anisotropic behaviour can be explained based on region that is subjected to maximum bending moment in the three-point bending test. The flexural tests along the E1 direction are performed with vertical beams extracted from the location 1 in Figure 5.7. In this case, the maximum bending moment and therefore the maximum bending stress develops across the interface existing at the center of the beam. Since the interface is weak and has a higher porosity, the beam fails at a low stress level as compared to the mould cast concrete. On the other hand for the loading along E2 and E3 directions, the maximum bending stress occurs in the bulk concrete. As seen in the porosity measurement, the bulk concrete is more densified and has a lower porosity as compared to the mould cast concrete. This may explain the relatively higher flexural strengths obtained when tested along E2 and E3 directions. Similar anisotropic behaviour of 3D printable concrete in flexural tests have been also reported by few other researchers (Le *et al.*, 2012*b*; Panda *et al.*, 2017*a*).

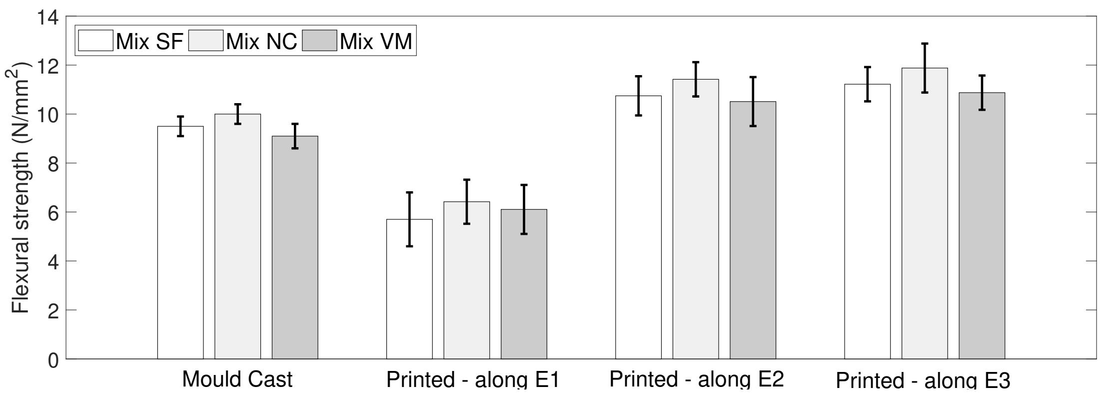

Figure 5.13: Comparison of flexural strength of printed concrete with that of mould cast concrete

It must be noted that for the porosity assessment, a total of four samples were tested. For the direct shear test, the number of tested samples were six while for the compression and the flexural strength test, a total of twelve samples each were tested. The bar graphs in Figures 5.10 to 5.13 indicate the average with the error bar as the standard deviation of the tested samples. The individual test results are also provided in Appendix B for reference.

5.3.5 Design perspectives for a 3D printed wall

At present, a problem pertaining to the use of 3D printed structures is that there are no standardized procedures for characterizing its mechanical behaviour (Buswell *et al.*, 2018). There is a need to understand how the values obtained from the mechanical characterization can be utilized in formulating a structural design procedure. To address this, some perspectives are provided on the design of a 3D printed wall. Further, a demonstration of how the values obtained from the current test procedures can be utilized in obtaining the parameters required for the structural design is also provided.

The results shown in Sections 5.3.1 and 5.3.2 indicate that the interfaces between the layers of a 3D printed element are weaker with higher porosity as compared to the bulk. Therefore, the design of a 3D printed wall can be considered analogous to that of a concrete masonry wall with bed joints. For a masonry wall, axial compression, out-of-plane flexure, in-plane and out-of-plane shear (see Figure 5.14) are important aspects to be considered in the design (TEK 14-7C, 2013). The design requirements with respect to each of these aspects for a 3D printed wall are presented in the following sections.

It should be noted that the comparison to a masonry wall may not be applicable for all cases. In systems where the interlayer bonding is good, the design may be carried out like a conventional monolithic concrete structure without the need to consider the effect of interfaces. However, for the cases where the effect of interfaces is significant, the design procedure outlined in the following sections can be made applicable.

Axial compression

Based on the design recommendations for unreinforced concrete masonry (TEK 14-7C, 2013), the allowable axial compressive stress, f_a in a 3D printed wall element can be calculated as given below:

$$f_a = \frac{\phi f_m^{'}}{F}. \tag{5.2}$$

In the above equation, $f_m^{'}$ is the compressive stress measured by the testing of cubes along the direction D1 (see Figure 5.5) and F is the factor of safety. The factor ϕ is used to account for the difference in the height to thickness ratio of the actual wall element with respect to that of the cubes used for measuring the compressive stress. The value of ϕ may be chosen based on the recommendations given in the design codes for concrete masonry (TEK 14-7C, 2013). But for a more realistic calculation, it can be obtained by determining the compressive strength of printed specimens with different height to thickness ratios to obtain an empirical correlation between the compressive strength and height to thickness ratio. The value of ϕ may be then chosen based on this empirical relationship. Apart from the failure criteria given by Equation (5.2), the wall may also undergo a buckling failure. Based on the design recommendations for unreinforced concrete masonry (TEK 14-7C, 2013), the buckling load (P_e) can be calculated by the following equation:

$$P_e = \left(\frac{\pi^2 E I_{xx}}{F h^2}\right)\left(1 - 0.577\frac{e}{r_{xx}}\right)^3. \tag{5.3}$$

In the above equation, I_{xx}, moment of inertia along the centroidal x-axis and r_{xx}, radius of gyration along the centroidal x-axis are the section properties. h, e and E are the effective height of the wall, eccentricity in loading and the modulus of elasticity respectively. Although the modulus of elasticity is not computed for the current study, it can be computed from a strain controlled compression test along D1 direction (see Figure 5.5) or alternatively by measuring the deflection from a strain controlled bending test along the E1 direction (see Figure 5.8b) and using the deflection equation to compute the modulus of elasticity.

Out-of-plane flexure

For a wall element, the out-of-plane bending can occur in two directions - via direction E1 shown in Figure 5.8b and direction E2 shown in Figure 5.9b. The three-point bending tests along these these directions therefore provide the flexural strength (f_b)

values needed for the design. Based on the recommendations for unreinforced concrete masonry (TEK 14-7C, 2013), the moment carrying capacity, M for both E1 and E2 directions can be calculated using the following equation:

$$f_b = \frac{1}{F}\left(\frac{Mt}{2I} - \frac{P}{A}\right). \tag{5.4}$$

In the above equation, I is the moment of inertia ($I = I_{xx}$, moment of inertia along centroidal x-axis for the loading along E1 direction while $I = I_{zz}$, moment of inertia along centroidal z-axis for loading along E2 direction), t is the thickness of the wall, P is the applied compression load and A is the cross-sectional area of the wall. The first term on the right hand side of Equation (5.4) denotes the maximum tensile bending stress while P/A is the axial compressive stress acting on the wall. If f_b calculated from Equation (5.4) is negative, it indicates that there is net compression under the combined action of bending and axial compression. In such a case, the maximum compressive stress is to be computed as shown below:

$$f_b = \frac{1}{F}\left(-\frac{Mt}{2I} - \frac{P}{A}\right). \tag{5.5}$$

The value of f_b calculated from the above equation should be less than f_a, the maximum allowable compressive stress computed using Equation (5.2).

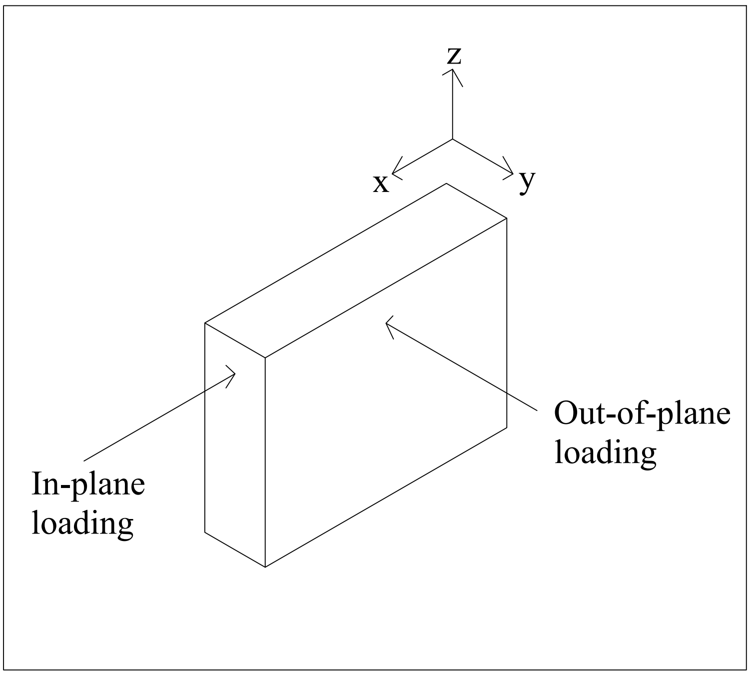

Figure 5.14: In-plane and out-of-plane loading in a wall element

In-plane and out-of-plane shear

The in-plane and out-of-plane shear are also aspects to be considered in the design of a wall element. From the design recommendations for unreinforced concrete masonry (TEK 14-7C, 2013), the shear load, V can be computed by using the following equation:

$$f_v = \frac{VQ}{FIb}. \tag{5.6}$$

The above equation is applicable for calculating both in-plane and out-of-plane shear stress. In the above equation, b is the width of the section at which the shear stress (f_v) is evaluated, Q is the first moment of area between the extreme fiber and the section at which shear stress is calculated ($Q = Q_{xx}$, first moment of area parallel to x-axis for evaluating out-of-plane shear stress along E1 direction, $Q = Q_{zz}$, first moment of area determined parallel to z-axis for evaluating out-of-plane shear stress along E2 direction and $Q = Q_{yy}$, first moment of area determined parallel to y-axis for evaluating in-plane shear stress), I is the moment of inertia ($I = I_{xx}$, moment of inertia along centroidal x-axis for evaluating out-of-plane shear stress along E1 direction, $I = I_{zz}$, moment of inertia along centroidal z-axis for evaluating out-of-plane shear stress along E2 direction and $I = I_{yy}$, moment of inertia along centroidal y-axis for evaluating in-plane shear stress).

When subjected to in-plane loading (see Figure 5.14), shear stresses develop along the interface between vertical layers. Therefore the bond shear strength between the vertical layers could be considered as the limiting value for the allowable in-plane shear stress. Similarly, for the out-of-plane loading along E1 direction (see Figure 5.8b), shear stress can develop along the interface between vertical layers. Therefore, again the bond strength between the vertical layers could be used as the limiting stress. For the out-of-plane loading along E2 direction (see Figure 5.8b), transverse shear stress can occur along the interface between horizontal layers. Therefore, the bond shear strength between horizontal layers may be considered as the limiting stress value for this case.

Utilizing the geometric flexibility in design

In 3D printed construction, structures with complex shape can be produced without the need of formwork. Therefore, for a designer it is important to realize that the load carrying capacity can be further improved by utilizing this geometric flexibility. For instance, consider a loading case where the out-of-plane flexure along E1 is more critical. As seen in Equation (5.4), apart from the bending resistance, f_b, the moment carrying capacity also depends on section properties such as the moment of inertia. With 3D printed structures, the designer has the flexibility to choose more efficient cross-sections. For instance, choosing a hollow rectangular section with the same cross-sectional area increases the moment of inertia and therefore, the moment carrying capacity along the E1 direction. Such shapes can be easily 3D printed without any additional formwork cost as compared to a conventional concrete structure.

In the foregoing sections, a design procedure for a 3D printed wall element, analogous to that of unreinforced concrete masonry was presented. However, it is to be noted that for a safe design, the failure of the structure must occur in a ductile manner. For this, understanding the post-crack behaviour of 3D printed concrete elements becomes important. Further, the possibility of introducing reinforcements needs to be explored.

5.4 Summary

In this chapter, test methods for characterizing the mechanical behaviour of 3D printed wall elements were presented. At first, the effect of interfaces present in a printed concrete element was examined through an assessment of porosity and bond shear test. The porosity was evaluated using specimens extracted from the bulk as well as from the interfaces between horizontal and vertical layers of printed concrete. It was found that the porosity in the bulk was lower by 6-8 % as compared to the mould cast concrete. On the other hand, the porosity at the interface between horizontal and vertical layers was found to be higher by 11-14 % and 10-16 % respectively. Therefore, although the bulk in 3D printed elements is more densified, the interfaces are weak with higher porosity. The interfaces were further evaluated by a direct bond shear test. Compared to the shear strength of the mould cast concrete, the shear strength at the interface between the horizontal and vertical layers was found to be lower by 24-25 % and 22-30 % respectively. The compressive strength of the printed concrete was similar when tested in different loading directions but lower by 12-22 % as compared to the mould cast concrete. This reduction in compressive strength may be due to the higher porosity at the interfaces present in printed concrete elements. The flexural strength was found to depend on the region subjected to the maximum bending moment. When tested along the direction where the maximum bending moment and therefore the maximum bending stress occurs at the weaker interfaces between layers, the flexure strength was lower by about 32-40 %. On the other hand, the flexural strength was found to increase by 13-20 % when tested in directions where maximum bending stress is induced in the bulk concrete, having a lower porosity as compared to the mould cast concrete. Finally, some perspectives were provided on formulating a structural design procedure for a 3D printed wall element.

CHAPTER 6

A THERMODYNAMIC-BASED RHEOLOGICAL MODEL FOR CEMENTITIOUS SYSTEMS

6.1 Introduction

The mix development approach for 3D printable concrete developed in this work has been mostly based on empirical methods. For instance, in Chapter 3, the range of yield stress that allows both extrudability and buildability was experimentally determined using trials conducted with the small-scale test bed printer. Therefore, it must be noted that the performance of developed mixes is dependant on the 3D printer system used in the study. However, simulation studies of the extrusion process can be performed to examine if the developed mixes are extrudable using other 3D printer systems or to predict the deformation in the printed layer when there is a change in print parameters like the nozzle dimensions. In this regard, there is a need for a complete three-dimensional rheological model that can describe cementitious systems. Although there are existing rheological models, these models have several shortcomings, such as being only one-dimensional and not necessarily complying to the fundamental requirements of continuum mechanics and thermodynamics. In this chapter, using a thermodynamics based approach, a three-dimensional model is developed for cementitious systems. The yielding behaviour is described by using the notion of multiple natural configurations. A structural parameter, with its evolution with deformation, is used to characterize the thixotropic behavior. The solution of the proposed model for a torsional flow problem and its corroboration with the experimental results are also presented.

6.2 Development of the model

6.2.1 Preliminaries

Let κ_r be a reference configuration, and κ_t be the current configuration at any time, t, of a body, as shown in Figure 6.1. Upon the removal of the external forces acting on the body, it is assumed that the body instantaneously takes a new configuration, κ_p, which is referred to as the preferred natural configuration. A more detailed description of the framework of natural configurations can be found in the work of the Rajagopal (1995). Let the gradient of the mapping from $\kappa_r \mapsto \kappa_t$ be denoted as $\mathbf{F}_{\kappa_r}$, that from $\kappa_p \mapsto \kappa_t$ and $\kappa_r \mapsto \kappa_p$ be denoted as $\mathbf{F}_{\kappa_p}$ and $\mathbf{G}$, respectively. $\mathbf{F}_{\kappa_r}$, $\mathbf{F}_{\kappa_p}$, and $\mathbf{G}$ are related through

$$\mathbf{F}_{\kappa_p} := \mathbf{F}_{\kappa_r}\mathbf{G}^{-1}. \tag{6.1}$$

Let $\mathbf{L}$ be the velocity gradient. Therefore,

$$\mathbf{L} := \dot{\mathbf{F}}_{\kappa_r}\mathbf{F}_{\kappa_r}^{-1}. \tag{6.2}$$

Let $\mathbf{L}_p$ be defined as follows

$$\mathbf{L}_p := \dot{\mathbf{G}}\mathbf{G}^{-1}. \tag{6.3}$$

Taking the time derivative of Equation (6.1) and using Equations (6.2) and (6.3), it can be shown that

$$\dot{\mathbf{F}}_{\kappa_p} = \mathbf{L}\mathbf{F}_{\kappa_p} - \mathbf{F}_{\kappa_p}\mathbf{L}_p. \tag{6.4}$$

Let $\mathbf{B}_{\kappa_p}$ be given by

$$\mathbf{B}_{\kappa_p} := \mathbf{F}_{\kappa_p}\mathbf{F}_{\kappa_p}^T. \tag{6.5}$$

Substituting from Equation (6.1) in Equation (6.5),

$$\mathbf{B}_{\kappa_p} = \mathbf{F}_{\kappa_r}\mathbf{G}^{-1}\mathbf{G}^{-T}\mathbf{F}_{\kappa_r}^T. \tag{6.6}$$

Taking the time derivative of Equation (6.6) and using Equations (6.1) to (6.3), it can be shown that

$$\dot{\mathbf{B}}_{\kappa_p} = -2\mathbf{F}_{\kappa_p}\mathbf{D}_p\mathbf{F}_{\kappa_p}^T + \mathbf{L}\mathbf{B}_{\kappa_p} + \mathbf{B}_{\kappa_p}\mathbf{L}, \tag{6.7}$$

where $\mathbf{D}_p$ is the symmetric part of $\mathbf{L}_p$. The upper convected or Oldroyd derivative (Oldroyd, 1958) for $\mathbf{B}_{\kappa_p}$ is given by

$$\overset{\triangledown}{\mathbf{B}}_{\kappa_p} = \dot{\mathbf{B}}_{\kappa_p} - \mathbf{L}\mathbf{B}_{\kappa_p} - \mathbf{B}_{\kappa_p}\mathbf{L}^T. \tag{6.8}$$

From Equations (6.7) and (6.8), it can be shown that

$$\overset{\triangledown}{\mathbf{B}}_{\kappa_p} = -2\mathbf{F}_{\kappa_p}\mathbf{D}_p\mathbf{F}_{\kappa_p}^T. \tag{6.9}$$

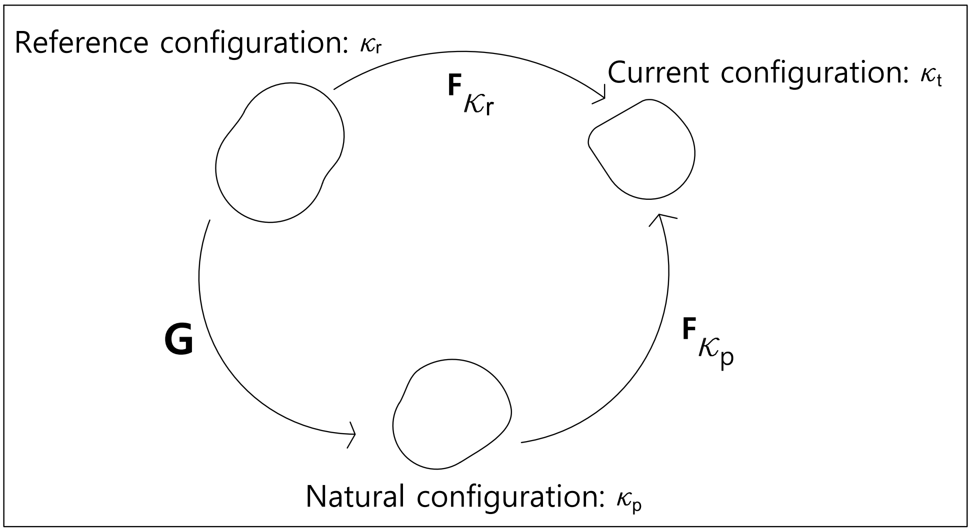

Figure 6.1: Reference, current and natural configurations

6.2.2 Thermodynamic considerations

In developing the constitutive equation, it is assumed that the material can undergo only isochoric motions. Therefore, it is stipulated that

$$tr(\mathbf{L}) = tr(\mathbf{L}_p) = tr(\mathbf{D}_p) = 0. \tag{6.10}$$

By using Equations (6.5), (6.8) and (6.10), it can be shown that

$$\overset{\nabla}{\mathbf{B}}_{\kappa_p}.\mathbf{B}_{\kappa_p}^{-1} = 0. \tag{6.11}$$

For isothermal processes, the rate of dissipation, ξ, is given by the equation (see Rajagopal and Srinivasa (2000))

$$\xi = \mathbf{T.L} - \rho\dot{\psi} \geq 0, \tag{6.12}$$

where $\mathbf{T}$ is the stress tensor, and ψ is the Helmholtz potential. Let the Helmholtz potential, ψ be a function of the stretch tensor, $\mathbf{B}_{\kappa_p}$, and also a structural parameter, λ:

$$\psi = \hat{\psi}(\mathbf{B}_{\kappa_p}, \lambda). \tag{6.13}$$

Using the chain rule of differentiation and using Equation (6.7), the material time derivative of ψ can be obtained as

$$\dot{\psi} = 2\frac{\partial\hat{\psi}}{\partial\mathbf{B}_{\kappa_p}}\mathbf{B}_{\kappa_p}.\mathbf{D} - 2\mathbf{F}_{\kappa_p}^T\frac{\partial\hat{\psi}}{\partial\mathbf{B}_{\kappa_p}}\mathbf{F}_{\kappa_p}.\mathbf{D}_p + \frac{\partial\hat{\psi}}{\partial\lambda}\dot{\lambda}. \tag{6.14}$$

By substituting Equation (6.14) in Equation (6.12), it can be shown that

$$\left(\mathbf{T} - 2\rho\frac{\partial\hat{\psi}}{\partial\mathbf{B}_{\kappa_p}}\mathbf{B}_{\kappa_p}\right).\mathbf{D} + 2\rho\mathbf{F}_{\kappa_p}^T\frac{\partial\hat{\psi}}{\partial\mathbf{B}_{\kappa_p}}\mathbf{F}_{\kappa_p}.\mathbf{D}_p - \rho\frac{\partial\hat{\psi}}{\partial\lambda}\dot{\lambda} = \xi \geq 0. \tag{6.15}$$

The above equation must hold for all possible values of $\mathbf{D}$, $\mathbf{D}_p$, and $\dot{\lambda}$, including the cases where $\mathbf{D}_p = \mathbf{0}$ and $\dot{\lambda} = 0$. This implies that

$$\mathbf{T} = \hat{\mathbf{T}} - p\mathbf{1}, \tag{6.16}$$

$$\text{where} \qquad \hat{\mathbf{T}} := 2\rho\frac{\partial\hat{\psi}}{\partial\mathbf{B}_{\kappa_p}}\mathbf{B}_{\kappa_p}. \tag{6.17}$$

In the above equation, the term $p\mathbf{1}$ arises due to the incompressibility constraint. Substituting, Equations (6.16) and (6.17) in Equation (6.15), and also using Equation (6.10), it can be shown that

$$2\rho\mathbf{F}_{\kappa_p}^T\frac{\partial\hat{\psi}}{\partial\mathbf{B}_{\kappa_p}}\mathbf{F}_{\kappa_p}.\mathbf{D}_p - \rho\frac{\partial\hat{\psi}}{\partial\lambda}\dot{\lambda} = \xi \geq 0. \tag{6.18}$$

The rate of dissipation is assumed to be of the form

$$\xi = \hat{\xi}(\mathbf{B}_{\kappa_p}, \lambda, \mathbf{D}_p, \dot{\lambda}). \tag{6.19}$$

Proceeding along the lines proposed by Rajagopal and Srinivasa (1998), it is assumed that the state of the body changes such that the rate of dissipation is maximized with respect to $\mathbf{D}_p$ and $\dot{\lambda}$, subject to the constraints of incompressibility (Equation (6.10)) and the reduced dissipation equation (Equation (6.18)). For the constrained maximization of the rate of dissipation function, ξ using the Lagrange method, an auxiliary function, ξ^*, is defined as

$$\xi^* := \xi - \hat{k}\left(\xi - 2\rho\mathbf{F}_{\kappa_p}^T\frac{\partial\hat{\psi}}{\partial\mathbf{B}_{\kappa_p}}\mathbf{F}_{\kappa_p}.\mathbf{D}_p + \rho\frac{\partial\hat{\psi}}{\partial\lambda}\dot{\lambda}\right) - \hat{q}\left(\mathbf{1}.\mathbf{D}_p\right). \tag{6.20}$$

In the above equations, $\hat{k}$ and $\hat{q}$ are Lagrange multipliers. For finding the maxima, the derivatives of the auxiliary function ξ^* with respect to $\mathbf{D}_p$ and $\dot{\lambda}$ are set equal to zero. This results in the following equations:

$$k\frac{\partial\xi}{\partial\mathbf{D}_p} = \mathbf{F}_{\kappa_p}^T\hat{\mathbf{T}}\mathbf{F}_{\kappa_p}^{-T} - q\mathbf{1}, \tag{6.21}$$

$$k\frac{\partial\xi}{\partial\dot{\lambda}} = -\rho\frac{\partial\hat{\psi}}{\partial\lambda}, \tag{6.22}$$

where $k = \dfrac{\hat{k}-1}{\hat{k}}$, and $q = \dfrac{\hat{q}}{\hat{k}}$. Equations (6.21) and (6.22) represent the evolution equation for $\mathbf{B}_{\kappa_p}$ and λ, respectively. The values of k and q can be determined by the satisfaction of the constraints given by Equations (6.10) and (6.18).

6.2.3 Specific constitutive assumptions

Specific forms for ψ and ξ are proposed that will result in a constitutive equation that can describe these attributes of cement paste. Let the Helmholtz potential and the rate of dissipation function be as follows:

$$\rho\hat{\psi}(\mathbf{F}_{\kappa_p}, \lambda) = \frac{1}{2}\mu(\lambda)\left[tr(\mathbf{B}_{\kappa_p}) - 3\right] + a\lambda^2, \tag{6.23}$$

$$\xi = Y(\lambda)\alpha^{\frac{1}{2}} + \eta(\lambda)\alpha + c\dot{\lambda}^2, \tag{6.24}$$

$$\text{where } \mu(\lambda) = \mu_0 e^{n_1\lambda}, \tag{6.25}$$

$$Y(\lambda) = Y_0 e^{n_2\lambda}, \tag{6.26}$$

$$\eta(\lambda) = \eta_0 e^{n_3\lambda}, \tag{6.27}$$

$$\alpha = \mathbf{F}_{\kappa_p}\mathbf{D}_p.\mathbf{F}_{\kappa_p}\mathbf{D}_p. \tag{6.28}$$

In the above equations, $\mu(\lambda)$ is a shear modulus function, and $Y(\lambda)$ and $\eta(\lambda)$ are the yield stress and viscosity functions, respectively. The expression for the extra stress can be obtained by combining Equation (6.23) with Equation (6.17):

$$\hat{\mathbf{T}} = \mu(\lambda)\mathbf{B}_{\kappa_p}. \tag{6.29}$$

To describe the yielding behavior in the model, an approach similar to that by Srinivasa (2001) is used. Due to the presence of the term $Y\alpha^{\frac{1}{2}}$ in Equation (6.24), ξ is non-differentiable when $\mathbf{D}_p = \mathbf{0}$. It is, therefore, necessary to consider two cases, separately - when $\mathbf{D}_p = \mathbf{0}$ and $\mathbf{D}_p \neq \mathbf{0}$. When $\mathbf{D}_p = \mathbf{0}$, Equation (6.24) becomes

$$\xi = c\dot{\lambda}^2. \tag{6.30}$$

Since ξ is a function of $\dot{\lambda}$ only, the auxiliary equation (Equation (6.20)) is first modified by setting $\mathbf{D}_p = \mathbf{0}$. Then, its derivative is set to zero for maximization of ξ with respect to $\dot{\lambda}$. Using $\mathbf{D}_p = \mathbf{0}$ in Equation (6.9), the following constitutive equations can be obtained

$$\overset{\triangledown}{\mathbf{B}}_{\kappa_p} = \mathbf{0}, \tag{6.31}$$

$$2ck\dot{\lambda} = -n_1\mu(\lambda)\left[tr(\mathbf{B}_{\kappa_p}) - 3\right] - 2a\lambda. \tag{6.32}$$

Substituting $\mathbf{D}_p = \mathbf{0}$ in Equation (6.18) and by using Equation (6.22), it can be shown that

$$k = \frac{\xi}{\dfrac{\partial \xi}{\partial \dot{\lambda}} \dot{\lambda}}. \tag{6.33}$$

Substituting Equation (6.30), the value of k can be obtained to be

$$k = \frac{1}{2}. \tag{6.34}$$

Now, consider the case when $\mathbf{D}_p$ is non-zero. From Equations (6.24) and (6.28), it can be shown that

$$\frac{\partial \xi}{\partial \mathbf{D}_p} = \left[Y(\lambda) \alpha^{-\frac{1}{2}} + 2\eta(\lambda) \right] \mathbf{C}_{\kappa_p} \mathbf{D}_p, \tag{6.35}$$

$$\text{where } \mathbf{C}_{\kappa_p} := \mathbf{F}_{\kappa_p}^T \mathbf{F}_{\kappa_p}. \tag{6.36}$$

Equation (6.35) was derived using the fact that $\mathbf{C}_{\kappa_p}$ and $\mathbf{D}_p$ have the same eigenvalues and, therefore, commute. By substituting Equation (6.35) in Equation (6.21) and using Equation (6.9), a relationship can be obtained for $\mathbf{B}_{\kappa_p}$ as follows:

$$\hat{\mathbf{T}} - q\mathbf{1} = -\frac{1}{2} k \left[Y(\lambda) \alpha^{-\frac{1}{2}} + 2\eta(\lambda) \right] \overset{\nabla}{\mathbf{B}}_{\kappa_p}. \tag{6.37}$$

By substituting Equations (6.23) and (6.24) in Equation (6.22), it can be shown that the evolution equation for λ will remain the same as that given by Equation (6.32). By substituting Equations (6.21) and (6.22) in Equation (6.18), and using Equations (6.10) and (6.16), the value of k can be obtained as

$$k = \frac{\xi}{\dfrac{\partial \xi}{\partial \mathbf{D}_p} . \mathbf{D}_p + \dfrac{\partial \xi}{\partial \dot{\lambda}} \dot{\lambda}}. \tag{6.38}$$

From Equations (6.24) and (6.35), it follows that

$$k = \frac{Y(\lambda) \alpha^{\frac{1}{2}} + \eta(\lambda) \alpha + c \dot{\lambda}^2}{Y(\lambda) \alpha^{\frac{1}{2}} + 2\eta(\lambda) \alpha + 2c \dot{\lambda}^2}. \tag{6.39}$$

Taking the inner product with $\mathbf{B}_{\kappa_p}^{-1}$ on both sides of Equation (6.37) and using Equations (6.11) and (6.29), the value of q can be obtained as

$$q = \frac{3\mu(\lambda)}{tr(\mathbf{B}_{\kappa_p}^{-1})}. \tag{6.40}$$

Substituting from Equation (6.9) in Equation (6.37) and post-multiplying with $\mathbf{F}_{\kappa_p}^{-T}$ on both sides, the following result can be obtained

$$kY(\lambda)\alpha^{-\frac{1}{2}}\mathbf{F}_{\kappa_p}\mathbf{D}_p = \left(\hat{\mathbf{T}} - q\mathbf{1}\right)\mathbf{F}_{\kappa_p}^{-T} - 2k\eta(\lambda)\mathbf{F}_{\kappa_p}\mathbf{D}_p. \tag{6.41}$$

Taking the inner product of Equation (6.41) with itself and using Equations (6.9) and (6.28), it can be shown that

$$[kY(\lambda)]^2 = \left(\hat{\mathbf{T}} - q\mathbf{1}\right)\cdot\left(\hat{\mathbf{T}} - q\mathbf{1}\right)\mathbf{B}_{\kappa_p}^{-1} + 2k\eta(\lambda)\overset{\nabla}{\mathbf{B}}_{\kappa_p}\cdot\left(\hat{\mathbf{T}} - q\mathbf{1}\right)\mathbf{B}_{\kappa_p}^{-1} + 4[k\eta(\lambda)]^2\alpha. \tag{6.42}$$

By substituting Equations (6.29) and (6.40) and using Equation (6.11), it follows that

$$[kY(\lambda)]^2 = [\mu(\lambda)]^2\left[tr(\mathbf{B}_{\kappa_p}) - \frac{9}{tr(\mathbf{B}_{\kappa_p}^{-1})}\right] + 2k\eta(\lambda)\mu(\lambda)tr(\overset{\nabla}{\mathbf{B}}_{\kappa_p}) + 4[k\eta(\lambda)]^2\alpha. \tag{6.43}$$

When $\mathbf{D}_p$ tends to zero, the above equation reduces to

$$[kY(\lambda)]^2 = [\mu[\lambda)]^2\left[tr(\mathbf{B}_{\kappa_p}) - \frac{9}{tr(\mathbf{B}_{\kappa_p}^{-1})}\right]. \tag{6.44}$$

The above equation represents the yield criterion. The final constitutive equations are summarized as follows

$$
\begin{aligned}
\text{Yield criterion:} \quad [kY(\lambda)]^2 \geq\ & [\mu(\lambda)]^2 \left[tr(\mathbf{B}_{\kappa_p}) - \frac{9}{tr(\mathbf{B}_{\kappa_p}^{-1})} \right] \\
& + 2k\eta(\lambda)\mu(\lambda) tr(\overset{\nabla}{\mathbf{B}}_{\kappa_p}) + 4[k\eta(\lambda)]^2\alpha. \\
\text{Stress:} \quad \mathbf{T} =\ & -p\mathbf{1} + \mu(\lambda)\mathbf{B}_{\kappa_p}. \\
\text{Below yield:} \quad \overset{\nabla}{\mathbf{B}}_{\kappa_p} =\ & \mathbf{0}. \\
\text{Above yield:} \quad \overset{\nabla}{\mathbf{B}}_{\kappa_p} =\ & -\frac{2}{\phi}\left[\mu(\lambda)\mathbf{B}_{\kappa_p} - q\mathbf{1}\right]. \\
\text{Evolution of } \lambda: \quad 2ck\dot{\lambda} =\ & -n_1\mu(\lambda)\left[tr(\mathbf{B}_{\kappa_p}) - 3\right] - 2a\lambda. \\
q =\ & \frac{3\mu(\lambda)}{tr(\mathbf{B}_{\kappa_p}^{-1})}, \\
k =\ & \frac{Y(\lambda)\alpha^{\frac{1}{2}} + \eta(\lambda)\alpha + c\dot{\lambda}^2}{Y(\lambda)\alpha^{\frac{1}{2}} + 2\eta(\lambda)\alpha + 2c\dot{\lambda}^2}, \\
\mu(\lambda) =\ & \mu_0 e^{n_1\lambda}, \\
Y(\lambda) =\ & Y_0 e^{n_2\lambda}, \\
\eta(\lambda) =\ & \eta_0 e^{n_3\lambda}, \\
\phi =\ & k\left[Y(\lambda)\alpha^{-\frac{1}{2}} + 2\eta(\lambda)\right].
\end{aligned}
\tag{6.45}
$$

6.2.4 Relationship with the Bingham model

The three-dimensional form of the Bingham model is given by the following equation (Beverly and Tanner, 1992)

$$
\begin{aligned}
\text{Yield criteria:} \quad Y \geq\ & \sqrt{II_T}, \\
\text{Below yield:} \quad \mathbf{D} =\ & \mathbf{0}, \\
\text{Above yield:} \quad \left(\frac{Y}{\sqrt{II_D}} + \eta\right)\mathbf{D} =\ & \hat{\mathbf{T}}.
\end{aligned}
\tag{6.46}
$$

where II_D and II_T are the second invariants of $\mathbf{D}$ and $\hat{\mathbf{T}}$, respectively. To show the similarity between the proposed model and Equation (6.46), Equation (6.9) is substituted in Equation (6.37) which gives the result

$$
k\left[Y(\lambda)\alpha^{-\frac{1}{2}} + 2\eta(\lambda)\right]\mathbf{F}_{\kappa_p}\mathbf{D}_p\mathbf{F}_{\kappa_p}^T = \hat{\mathbf{T}} - q\mathbf{1}. \tag{6.47}
$$

Pre-multiplying with $\mathbf{F}_{\kappa_p}^{-1}$ and post-multiplying with $\mathbf{F}_{\kappa_p}^{-T}$ on both sides of Equation (6.47), and on re-arranging, it follows that

$$\begin{aligned} &\text{Below yield:} & \mathbf{D}_p =& \ \mathbf{0}, \\ &\text{Above yield:} & \left[\frac{Y(\lambda)}{\sqrt{\alpha}} + 2\eta(\lambda)\right]\mathbf{D}_p =& \ \frac{1}{k}\mathbf{F}_{\kappa_p}^{-1}\left(\hat{\mathbf{T}} - q\mathbf{1}\right)\mathbf{F}_{\kappa_p}^{-T}. \end{aligned} \tag{6.48}$$

The above set of equations of the proposed model has a form similar to that of Equation (6.46). If $\mu(\lambda)$ tends to infinity, it can be shown that $\mathbf{D}_p \rightarrow \mathbf{D}$, and the scalar $\alpha \rightarrow II_D$. Further, if $Y(\lambda)$ and $\eta(\lambda)$ are also taken as constants, the proposed model will reduce to the Bingham model.

6.2.5 Thixotropic behavior

To understand how the structural changes due to thixotropy are accounted for in the model, the evolution equation for λ (Equation $(6.45)_5$) must be examined. For instance, consider the case when the material is subjected to a simple-shear motion. Because of the form for $\mathbf{T}$ given by Equation $(6.45)_2$, the value of $\mu(\lambda)[tr(\mathbf{B}_{\kappa_p}) - 3]$ increases as shearing occurs in the material. If λ is initially zero and n_1 is negative, then the form for the evolution equation for λ suggests λ would increase with time. The term $2a\lambda$ would, however, ensure that the λ would eventually approach a steady state. Considering n_2 and n_3 also as negative constants, this implies that the modulus, yield stress, and viscosity functions decrease as the value of λ increases, which in turn, captures the shear-induced structural breakdown in the material. In the absence of shear, the term $n_1\mu(\lambda)[tr(\mathbf{B}_{\kappa_p}) - 3]$ becomes zero. In this case, Equation (6.40) becomes

$$2ck\dot{\lambda} = -2a\lambda. \tag{6.49}$$

An analytical solution for λ can be obtained for the above equation and is given by

$$\lambda(t) = \lambda_0 exp\left(-\frac{at}{ck}\right). \tag{6.50}$$

The above equation gives λ as a function of the rest time, t, with λ_0 being value of λ immediately before the shear load is removed. Considering a and c as positive constants, the above equation suggests that the value of $\dot{\lambda}$ decreases with the rest time, t.

Since n_1, n_2, and n_3 are negative constants, this implies that the modulus, yield stress, and viscosity functions increase as the rest time increases, which in turn, describes the structural build-up in the material in the absence of deformation.

In this way, $\lambda = 0$ indicates a fully intact microstructure with no degradation, while $\lambda = \infty$ represents a completely broken down microstructure for the material. The evolution equation for λ is such that the structural parameter increases when subjected to deformation. But, this increase is reversible in the sense that the value for λ will decrease in the absence of deformation. In this manner, the reversible changes due to thixotropy is described by the model.

6.3 Experimental work

6.3.1 Materials used

Initially, the experimental corroboration of the model was planned to be done using the VM mix developed for the small-scale 3D printer (Chapter 3). However, due to the large size particles of quartz sand 1 and quartz sand 2 (having d_{50} of 434 and 750 micron respectively) contained in the VM mix, the mix could not be tested in the dynamic shear rheometer used in the current study. To facilitate the testing in rheometer, an attempt was made to obtain an equivalent mortar for the VM mix with only the smaller size quartz powder (d_{50} of 24 micron) as the fine aggregate using the concrete equivalent mortar (CEM) method (Assaad and Khayat, 2004; Erdem *et al.*, 2009; Kabagire *et al.*, 2015). However, based on the preliminary studies, the CEM mix was found to be not truly representative of the original VM mix (the procedures involved in proportioning the CEM mix and its comparison with the original VM mix are illustrated in Appendix C). In light of this, it was decided that the model validation will be performed using a non-representative cement paste sample. Later, as a future scope to the current study, the model will be extended to mixes developed in the current study by conducting experiments using rheometer capable of testing mortars and concrete.

The cement paste used in the study was prepared using an ASTM Type I cement ASTM C150 / C150M-19a (2019) with a water-to-cement ratio of 0.3. The cement used had a specific gravity of 3.15 and has a Blaine and BET specific surface area of

412 and 1318 m^2/kg, respectively. Its oxide composition is shown in Table 6.1. A polycarboxylic ether (PCE) based superplasticizer was used at a dosage of 0.3 % of the cement content. The superplasticizer was used in the liquid form with a solid content of 34 %.

The mixing was done using a high shear blender. At first, the water mixed with the superplasticizer was added to the mixer, followed by the cement. The mixing was done for a total duration of two minutes.

Table 6.1: Oxide composition of cement used

Oxide present	Quantify (% by mass)
CaO	63.21
SiO_2	19.60
Al_2O_3	4.09
Fe_2O_3	3.39
MgO	3.37
SO_3	3.17
LOI	2.54

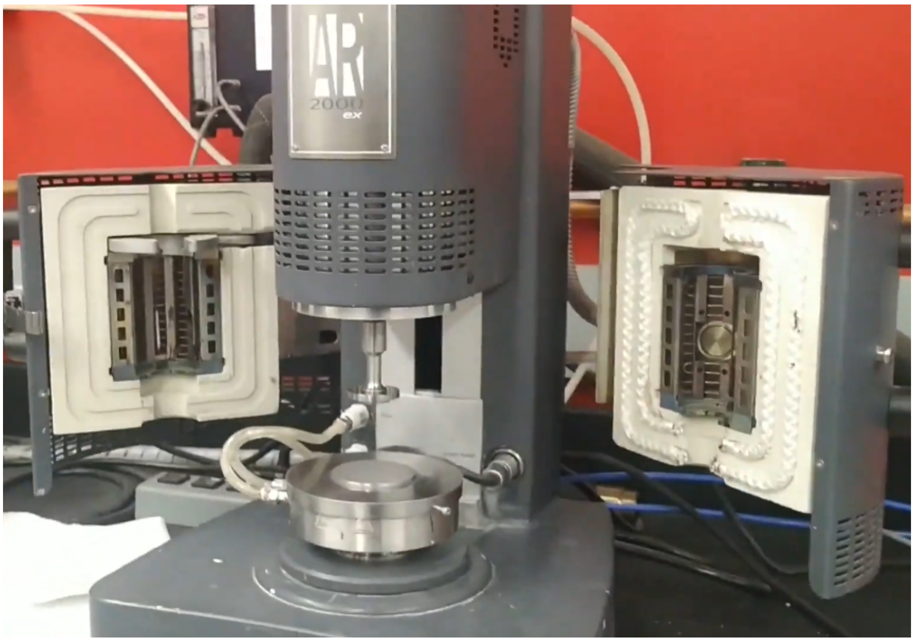

Figure 6.2: Dynamic shear rheometer attached with 20 mm parallel plate fixture

6.3.2 Rheological measurements

Performing rheological experiments on suspensions like cement paste can be quite challenging. Some of the aspects that needs to be considered while planning such experiments are summarized in Appendix D. The rheological experiments for modelling work were done during a one month exchange program to Arizona State University, Tempe, USA. The measurements were carried out using a dynamic shear rheometer fitted with a parallel plate geometry with serrated upper and lower plates (Figure 6.2). The diameter of the plates was 20 mm, and the gap between the plates during measurement was 1 mm. Prior to performing the actual testing, all mixes were subjected to a pre-shear. The pre-shear consisted of applying a constant strain rate of 10 s^{-1} for a duration of 60 seconds, followed by a rest period of another 60 seconds. Two sets of tests were carried out. In the first set, a constant strain rate was applied, and the stress response was monitored over a total duration of 100 seconds. Such experiments were conducted at strain rates of 0.1, 0.3, 1, 3, and 10 s^{-1}. A fresh cement paste was used for each case. The second set of experiments consisted of shear ramp-up and ramp-down experiments. The shear rates applied during the ramp-up and ramp-down experiment are shown in Figure 6.3. All tests were performed at least twice to confirm repeatability.

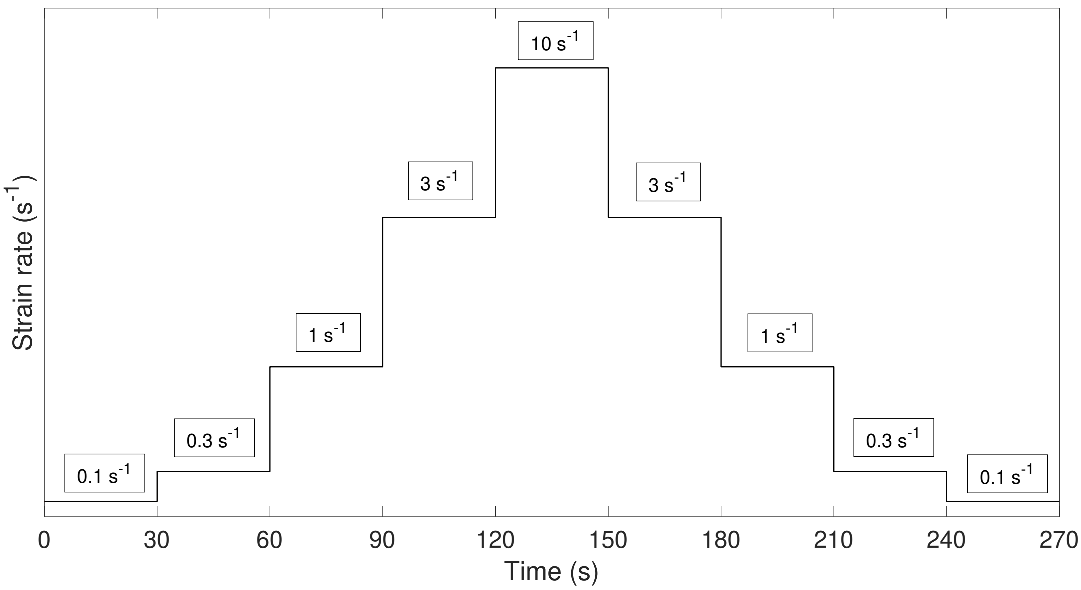

Figure 6.3: Ramp up and ramp down of strain rate

6.4 Corroboration of model with experimental data

6.4.1 Solution for torsional flow

Considering a cylindrical coordinate system, the velocity gradient for the torsional flow in the parallel-plate geometry was assumed to be of the form:

$$\mathbf{L} = \begin{pmatrix} 0 & z\dot{\Omega} & 0 \\ z\dot{\Omega} & 0 & r\dot{\Omega} \\ 0 & 0 & 0 \end{pmatrix}, \tag{6.51}$$

where Ω represents the twist per unit length. A semi-inverse approach was used to obtain the solution, by assuming a form for $\mathbf{B}_{\kappa_p}$:

$$\mathbf{B}_{\kappa_p} = \begin{pmatrix} B_{11} & 0 & 0 \\ 0 & B_{22} & B_{23} \\ 0 & B_{23} & B_{33} \end{pmatrix}. \tag{6.52}$$

Substituting Equation (6.52) in Equation (6.51), it can be shown that

$$\overset{\triangledown}{\mathbf{B}}_{\kappa_p} = \begin{pmatrix} \dot{B}_{11} & 0 & 0 \\ 0 & B_{22} - 2\dot{\gamma}B_{23} & \dot{B}_{23} - \dot{\gamma}B_{23} \\ 0 & \dot{B}_{12} - \dot{\gamma}B_{23} & \dot{B}_{33} \end{pmatrix}, \tag{6.53}$$

where $\dot{\gamma}$ is the shear strain rate. The value of $\mathbf{B}_{\kappa_p}$ and λ can now be obtained by substituting Equation (6.53) in Equation $(6.45)_3$ and $(6.45)_4$ and solving the resulting ordinary differential equation along with the evolution equation for λ (Equation $(6.45)_5$) using a numerical method. The torque can be obtained by

$$M(t) = 2\pi \int_0^R T_{\theta z} r^2 dr = 2\pi \int_0^R \mu(\lambda) B_{23} r^2 dr. \tag{6.54}$$

Steady-state flow condition

With time, both $\mathbf{B}_{\kappa_p}$ and λ will reach steady-state conditions. Under the steady-state conditions, $\dot{\mathbf{B}}_{\kappa_p} = \mathbf{0}$. Using this condition in Equation (6.53), it follows that

$$\overset{\nabla}{\mathbf{B}}_{\kappa_p} = \begin{pmatrix} 0 & 0 & 0 \\ 0 & -2\dot{\gamma}B_{23} & -\dot{\gamma}B_{23} \\ 0 & -\dot{\gamma}B_{23} & 0 \end{pmatrix}. \tag{6.55}$$

Substituting Equation (6.52) in Equation $(6.45)_4$, the following result can be obtained

$$\overset{\nabla}{\mathbf{B}}_{\kappa_p} = -\frac{2}{\phi}\begin{pmatrix} \mu(\lambda)B_{11} - q & 0 & 0 \\ 0 & \mu(\lambda)B_{22} - q & \mu(\lambda)B_{23} \\ 0 & \mu(\lambda)B_{23} & \mu(\lambda)B_{33} - q \end{pmatrix}. \tag{6.56}$$

Solving Equations (6.55) and (6.56), and using the steady-state condition $\dot{\lambda} = 0$ in Equation $(6.45)_5$, the following equations can be obtained for the steady-state condition

$$\mathbf{B}_{\kappa_p} = \frac{q}{\mu(\lambda)}\begin{pmatrix} 1 & 0 & 0 \\ 0 & 1 + \frac{\dot{\gamma}^2\phi^2}{2\mu(\lambda)^2} & \frac{\dot{\gamma}^2\phi^2}{2\mu(\lambda)^2} \\ 0 & \frac{\dot{\gamma}^2\phi^2}{2\mu(\lambda)^2} & 1 \end{pmatrix}, \tag{6.57}$$

$$0 = n_1\mu(\lambda)\left(tr(\mathbf{B}_{\kappa_p}) - 3\right) + 2a\lambda. \tag{6.58}$$

The incompressibility condition implies that $\det \mathbf{B}_{\kappa_p} = 1$. Therefore,

$$q = \frac{\mu(\lambda)}{\left[1 + \left[\frac{\dot{\gamma}\phi}{2\mu(\lambda)}\right]^2\right]^{\frac{1}{3}}}. \tag{6.59}$$

The steady-state values of $\mathbf{B}_{\kappa_p}$ and λ can be obtained by solving the above equations using a numerical method.

6.4.2 Model parameters by manual fitting

For determining the model predictions for the constant strain tests, the Equations (6.57) and (6.59) were solved using an ODE solver in Matlab R2019a. The stress obtained was used to determine torque by evaluating the integral in Equation (6.54) using Simpson's method. The parameters μ_0, Y_0, η_0, n_1, n_2, and n_3 can be determined by fitting the steady-state response of the model to the steady-state results from the experiments. The remaining model parameter, c, was determined by the fitting of the entire torque vs. time curve. From Figure 6.4, it can be observed that the steady-state torque versus the strain rate curve has a non-zero y-intercept, which will depend on the initial yield stress (Y_0) and initial modulus (μ_0). Also, from Figure 6.4, it can be seen that the material has a shear-thinning behavior. In the model, this is characterized by making the yield stress and the viscosity as decreasing functions of the structural parameter, λ. The shear-thinning behavior will also depend on the evolution of the structural parameter with time. This is controlled by the parameters a, μ_0, n_1, and c. From the entire torque vs. time curve shown in Figure 6.5, it can be seen that the torque initially overshoots to reach a peak, and then decreases to reach a steady state. In the model, this overshoot is described by making the yield stress and modulus as a function of the structural parameter, i.e., by controlling the values of n_1 and n_2.

A manual fitting was conducted, as shown in Figures 6.4 and 6.5, to determine the model parameters as given below:

$$\begin{aligned}
\mu_0 &= 100 \text{ Pa}, \\
Y_0 &= 27 \text{ Pa}, \\
\eta_0 &= 55 \text{ Pa-s}, \\
n_1 &= \text{-0.09}, \\
n_2 &= \text{-32}, \\
n_3 &= \text{-13.7}, \\
a &= 1, \\
c &= 10.
\end{aligned} \tag{6.60}$$

6.4.3 Ramp up and ramp down of shear rate - experiment and model prediction

The model prediction of torque during the ramp-up and ramp-down of strain rates was obtained using Matlab R2019a and compared with the experimental data, as shown in Figure 6.6a. From the experimental data, it can be observed that for a given strain rate, the torque overshoots for the ramp-up portion is lower than that obtained for the steady-shear experiments (Figure 6.5). During the steady-shear experiments, the sample was given a rest duration prior to the application of shear. On the other hand, in the ramp-up and ramp-down experiment, there were no rest periods provided between subsequent steps of shear-rate. As a result, the initial structure of the material is relatively more broken down and, the torque overshoot obtained during the ramp-up portion for a given strain rate is relatively lower than that obtained in the steady-shear experiment. In the model, this is characterized by the evolution of the structural parameter, λ as shown in Figure 6.6b. With an increase in step strain rate, the value of structural parameter increases to higher values. Since yield stress and the modulus are decreasing functions of the structural parameter, this decreases the torque overshoot as compared to that obtained in the steady-shear experiments.

In summary, the model predictions of both the transient and the steady-state torque compare well with the experimental data. This indicates that the proposed model is able to capture the time-dependent changes associated with the thixotropic behavior of cement paste.

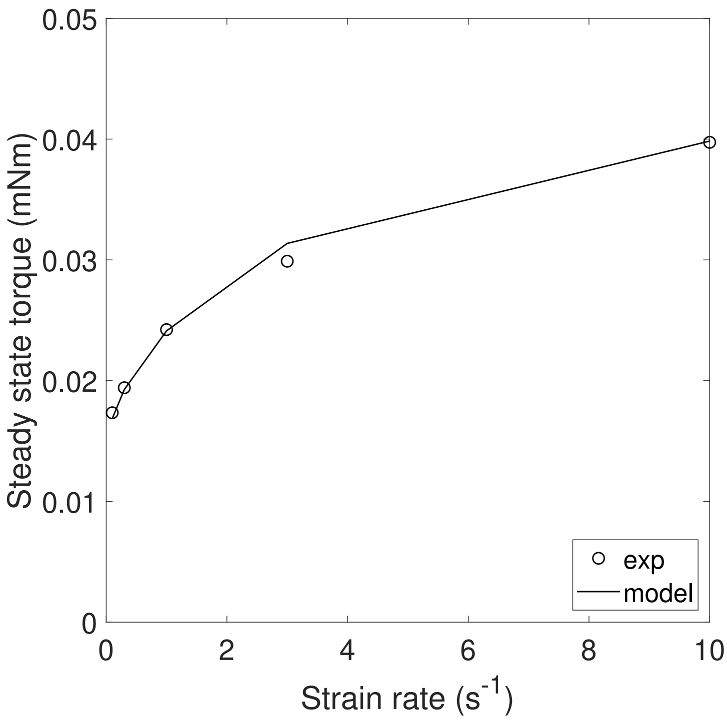

Figure 6.4: Comparison between model prediction and experimental values of the steady-state torque at different strain rates

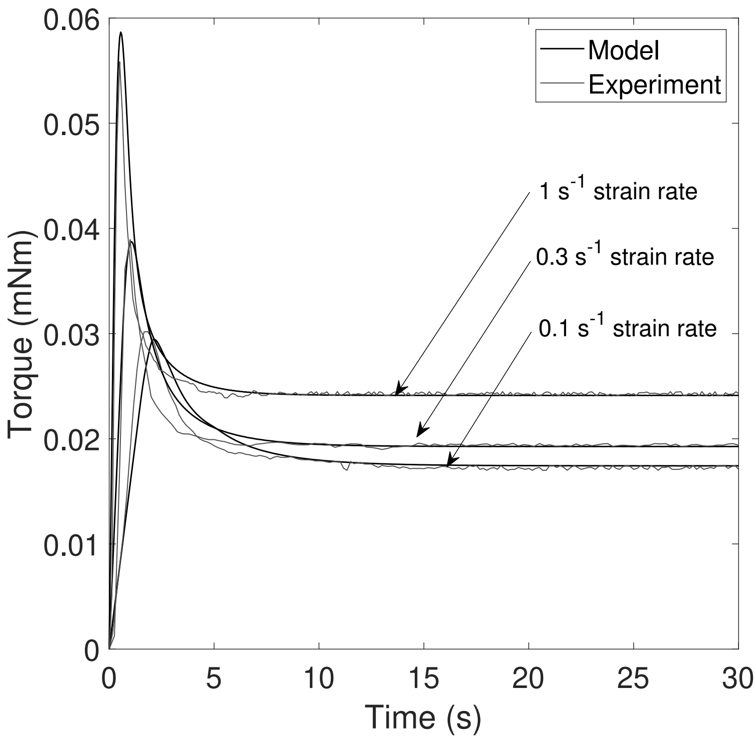

(a)

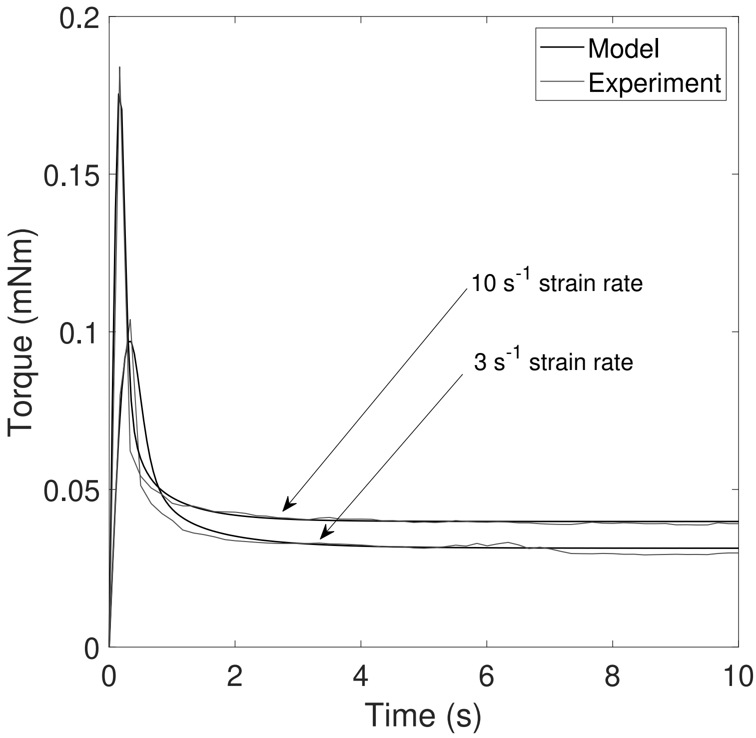

(b)

Figure 6.5: Comparison between model prediction and experimental values of the evolution of torque at (a) 0.1, 0.3 and 1 s^{-1} (b) (b) 3 and 10 s^{-1}

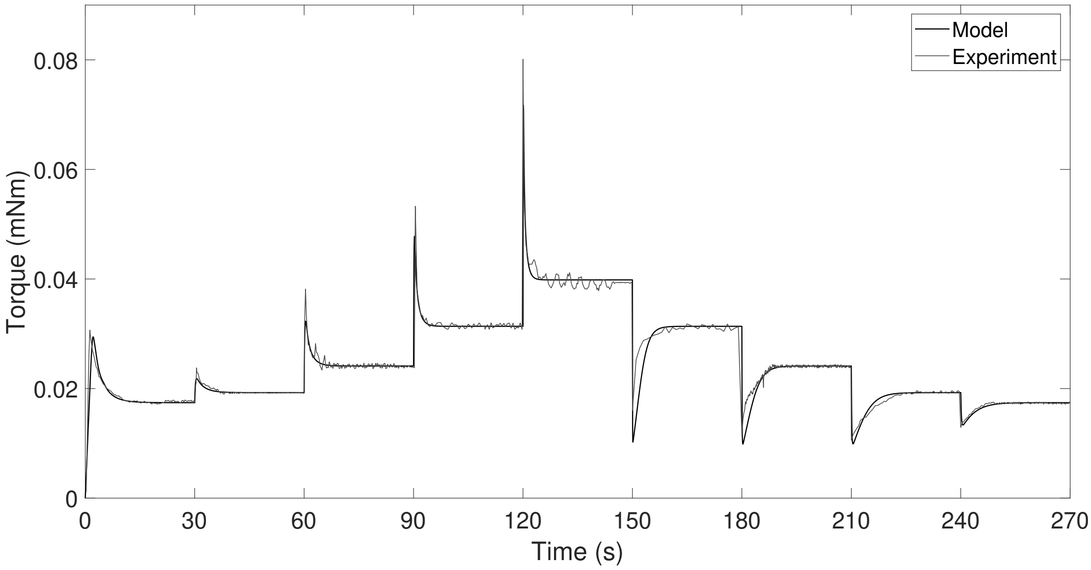

(a)

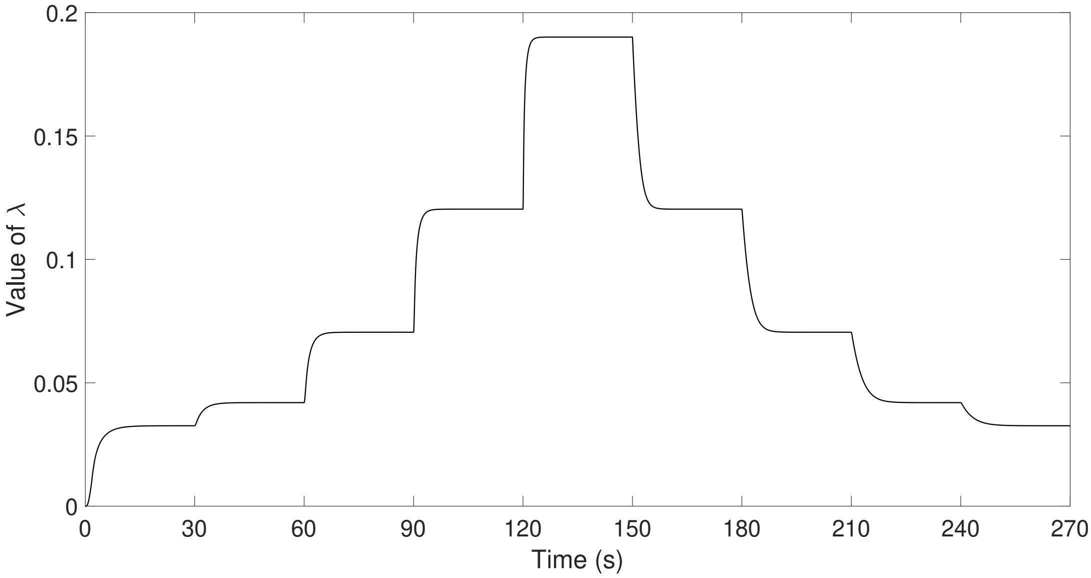

(b)

Figure 6.6: (a) Torque versus time, and (b) λ versus time during ramp-up and ramp-down of strain rate

6.5 Other variants of the model

In deriving Equation (6.45), specific forms were chosen for the Helmholtz potential, ψ and the rate of dissipation function, ξ, so that the resultant constitutive equations can accurately model the rheological behavior of cement paste in the experiments. However, other variants of this model can also be developed using the same framework. For instance, let ψ be given by Equation (6.23) and ξ be as follows

$$\xi = Y\beta^{\frac{1}{2}} + \eta\beta + c\dot{\lambda}^2, \tag{6.61}$$

$$\text{where } \beta = \mathbf{D}_p.\mathbf{D}_p. \tag{6.62}$$

By following similar procedures to that shown in section 6.2.3, the following constitutive equations can be obtained:

$$\begin{array}{lrl}
\text{Yield criterion:} & [kY(\lambda)]^2 \geq & [\mu(\lambda)]^2 \left[tr(\mathbf{B}^2_{\kappa_p}) - \dfrac{[tr(\mathbf{B}_{\kappa_p})]^2}{3}\right] \\
 & & +2k\eta(\lambda)\mu(\lambda)tr(\overset{\nabla}{\mathbf{B}}_{\kappa_p}) + 4[k\eta(\lambda)]^2\beta. \\
\text{Stress:} & \mathbf{T} = & -p\mathbf{1} + \mu(\lambda)\mathbf{B}_{\kappa_p}. \\
\text{Below yield:} & \overset{\nabla}{\mathbf{B}}_{\kappa_p} = & \mathbf{0}. \\
\text{Above yield:} & \overset{\nabla}{\mathbf{B}}_{\kappa_p} = & -\dfrac{2}{\phi}\left[\mu(\lambda)\mathbf{B}_{\kappa_p} - q\mathbf{1}\right]\mathbf{B}_{\kappa_p}. \\
\text{Evolution of } \lambda: & 2ck\dot{\lambda} = & -n_1\mu(\lambda)\left[tr(\mathbf{B}_{\kappa_p}) - 3\right] - 2a\lambda. \\
 & q = & \dfrac{\mu(\lambda)tr(\mathbf{B}_{\kappa_p})}{3}, \\
 & k = & \dfrac{Y(\lambda)\beta^{\frac{1}{2}} + \eta(\lambda)\beta + c\dot{\lambda}^2}{Y(\lambda)\beta^{\frac{1}{2}} + 2\eta(\lambda)\beta + 2c\dot{\lambda}^2}, \\
 & \mu(\lambda) = & \mu_0 e^{n_1\lambda}, \\
 & Y(\lambda) = & Y_0 e^{n_2\lambda}, \\
 & \eta(\lambda) = & \eta_0 e^{n_3\lambda}, \\
 & \phi = & k\left[Y(\lambda)\beta^{-\frac{1}{2}} + 2\eta(\lambda)\right].
\end{array} \tag{6.63}$$

The above model can also describe both yielding and thixotropic behavior.

A Herschel-Bulkley (Herschel and Bulkley, 1926) type model can also be obtained using the same framework. The three-dimensional form of the Herschel-Bulkley model can be written as

$$\begin{array}{lrl}
\text{Yield criterion:} & Y \geq & \sqrt{II_T}, \\
\text{Below yield:} & \mathbf{D} = & \mathbf{0}, \\
\text{Above yield:} & \left(\dfrac{Y}{\sqrt{II_D}} + \eta_H II_D^{\frac{n-1}{2}}\right)\mathbf{D} = & \hat{\mathbf{T}}.
\end{array} \tag{6.64}$$

where II_T abd II_D are the second invariants of the deviatoric stress and velocity gradient tensor, respectively, and η_H and n are the viscosity parameter and the power-law index, respectively. Let the specific forms for ψ and ξ be as follows

$$\rho\hat{\psi}(\mathbf{F}_{\kappa_p},\lambda) = \frac{1}{2}\mu(\lambda)\left[tr(\mathbf{B}_{\kappa_p}) - 3\right] + a\lambda^2, \tag{6.65}$$

$$\xi = Y\alpha^{\frac{1}{2}} + \eta\alpha^n + c\dot{\lambda}^2, \tag{6.66}$$

$$\text{where } \alpha = \mathbf{F}_{\kappa_p}\mathbf{D}_p.\mathbf{F}_{\kappa_p}\mathbf{D}_p. \tag{6.67}$$

This will result in the following constitutive equations:

$$\begin{array}{lrl}
\text{Yield criterion:} & [kY(\lambda)]^2 \geq & [\mu(\lambda)]^2\left[tr(\mathbf{B}_{\kappa_p}) - \dfrac{9}{tr(\mathbf{B}^{-1}_{\kappa_p})}\right] + \\
 & & 2k\eta(\lambda)\mu(\lambda)\alpha^{n-1}tr(\overset{\triangledown}{\mathbf{B}}_{\kappa_p}) + 4[k\eta(\lambda)]^2\alpha^{2n-1}. \\
\text{Stress:} & \mathbf{T} = & -p\mathbf{1} + \mu(\lambda)\mathbf{B}_{\kappa_p}. \\
\text{Below yield:} & \overset{\triangledown}{\mathbf{B}}_{\kappa_p} = & \mathbf{0}. \\
\text{Above yield:} & \overset{\triangledown}{\mathbf{B}}_{\kappa_p} = & -\dfrac{2}{\phi}\left[\mu(\lambda)\mathbf{B}_{\kappa_p} - q\mathbf{1}\right]. \\
\text{Evolution of } \lambda: & 2ck\dot{\lambda} = & -n_1\mu(\lambda)\left[tr(\mathbf{B}_{\kappa_p}) - 3\right] - 2a\lambda. \\
 & q = & \dfrac{3\mu(\lambda)}{tr(\mathbf{B}^{-1}_{\kappa_p})}, \\
 & k = & \dfrac{Y(\lambda)\alpha^{\frac{1}{2}} + \eta(\lambda)\alpha^n + c\dot{\lambda}^2}{Y(\lambda)\alpha^{\frac{1}{2}} + 2\eta(\lambda)n\alpha^n + 2c\dot{\lambda}^2}, \\
 & \mu(\lambda) = & \mu_0 e^{n_1\lambda}, \\
 & Y(\lambda) = & Y_0 e^{n_2\lambda}, \\
 & \eta(\lambda) = & \eta_0 e^{n_3\lambda}, \\
 & \phi = & k\left[Y(\lambda)\alpha^{-\frac{1}{2}} + 2\eta(\lambda)n\alpha^{n-1}\right].
\end{array} \tag{6.68}$$

By using a similar procedure to that shown in section 6.2.4, Equation $(6.68)_3$ and $(6.68)_4$ can be rearranged to get the following equations

$$\begin{array}{lrl}
\text{Below yield:} & \mathbf{D}_p = & \mathbf{0}, \\
\text{Above yield:} & \left(\dfrac{Y(\lambda)}{\alpha^{\frac{1}{2}}} + 2n\eta(\lambda)\alpha^{n-1}\right)\mathbf{D}_p = & \dfrac{1}{k}\mathbf{F}^{-1}_{\kappa_p}\left(\hat{\mathbf{T}} - q\mathbf{1}\right)\mathbf{F}^{-T}_{\kappa_p}.
\end{array} \tag{6.69}$$

The above set of equations has a form similar to that of Equation (6.64).

6.6 Importance and possible improvements in the current work

The current work presents a thermodynamic-based framework for developing models that can describe the rheology of cementitious systems. The characteristics required while choosing the specific forms for the Helmholtz potential and the rate of dissipation functions that are essential for developing such models are pointed out. The model developed using one such form was described extensively and corroborated with the experimental data. Although there is good experimental corroboration, the large number of parameters used is a shortcoming. There exist phenomenological models with lesser model parameters that can describe the rheological behaviour of cement paste (Roussel, 2005). However, it must be noted that, compared to a complete three-dimensional model obtained using the current approach, such phenomenological models are only one-dimensional. Further, the compliance of such models to fundamental laws of continuum mechanics and laws of thermodynamics is questionable.

With respect to the rheology of cement paste, another aspect that warrants discussion is the occurrence of shear banding in yield stress fluids. Fall *et al.* (2010) observed that when thixotropic yield stress fluids are subjected to different sustained shear stress, no flow occurs when the strain rate corresponding to the applied stress was below a critical non-zero value, indicating a discontinuity in the flow with respect to the stress. The specific forms for ψ and ξ described in Section 6.2.3 does account for the occurrence of shear banding. A constitutive equation for the structural parameter that can also capture the effect of shear banding is described in the work by Roussel *et al.* (2004). Based on this work, further improvements may be made in the forms for ψ and ξ, which can also capture the effect of shear banding using the thermodynamic framework.

Another aspect is the fact that the cement particles undergoes hydration reaction as time proceeds. Within the thermodynamic framework, chemically reacting systems can also be modelled (Kannan and Rajagopal, 2011). Therefore, incorporating the effect of cement hydration would also be another aspect that could be explored in future works using this framework.

6.7 Summary

In this chapter, a rheological model for cement paste was formulated using a thermodynamic framework. The yielding behaviour was accounted for in the model by using the approach of multiple natural configurations. The structural changes associated with thixotropy were captured using a structural parameter and its evolution with deformation. The final constitutive equations were obtained using the second law of thermodynamics and the maximum rate of dissipation criterion. From the corroboration of the model with experimental results, it was seen that the proposed model can describe both the yielding behaviour as well as the reversible structural changes associated with thixotropy of cement paste. The it is unable to account for the effect of sear banding as well as for the irreversible structural changes with time due to cement hydration. However, the framework developed in this study can be suitably extended so that these features are also captured by the model.

CHAPTER 7

CONCLUDING REMARKS AND WAY FORWARD

7.1 General conclusions

Extrusion-based concrete 3D printing is a promising technology for the future. But to harness the technology, it is paramount to understand its material requirements. In this work, the mixture design, the mechanical properties and the development of a rheological model that can be useful for simulation studies in 3D printing were presented. The general conclusions are as follows:

1. In this work, a systematic procedure is presented for the mixture proportioning of 3D printable concrete. The approach is based on adjusting the superplasticizer dosage such that the mixture has a yield stress that allows both extrudability and buildability during printing. It was shown that the addition of methyl cellulose is required to obtain robust printable mixtures. On the other hand, the additions of nanoclay and silica fume can provide an increased structural build-up for the mixtures.

2. An approach-based on desorptivity was formulated for assessing the water drainage that may occur when high pressure is applied during an extrusion process. Using this approach, an index was formulated that can predict the failure in extrudability tests when phase separation occurs in the concrete mixture. This approach can be used to design mixtures for large-sale 3D printer systems where cementitious systems are to be subjected to high extrusion pressure.

3. The uniaxial compression tests can be used to characterize the early age mechanical behaviour of 3D printed concrete. Using the strength and elastic modulus obtained from the tests, a rough estimate of failure height considering both plastic and buckling collapse that may occur during printing can be obtained.

4. For an accurate analysis of failure or to assess the deformation in the layers during printing, simulation studies are needed. A three-dimensional rheological model was

developed based on a sound thermodynamic framework for cementitious systems. The model can capture the yielding and the thixotropic behaviour and can be useful in simulation studies of the printing process. The model can also be useful for other applications like predicting formwork pressure in SCC and also for designing slip-form concrete.

5. From this work, insights are also provided about the hardened properties of 3D printable concrete. Due to the presence of interface between the layers, the compressive and flexural strength of 3D printed concrete are lower than that of conventional concrete. Based on an analogy to masonry structures, recommendations are provided for the structural design of a 3D printed vertical wall element.

7.2 Specific conclusions

The specific conclusions from this work are as follows:

1. **Studies using the small-scale 3D printer**:

(a) Layer-wise buildability is possible only when the material yield stress is within a certain range. A low yield stress value causes the layers to collapse preventing layer-wise buildability. On the other hand, if the yield stress is too high, the material is too stiff to allow extrudability. The working mixtures were found to have a yield stress within 1.5 - 2.5 kPa.

(b) The preliminary reference mixture design was prepared by using a binder combination of portland cement and fly ash. The proportioning of dry granular materials was based on the particle packing method. The dosage of superplasticizer was determined by performing the buildability and extrudability tests. The mixture lacked stability and robustness. Also, it was printable only for 15 minutes.

(c) Additions of nanoclay improved the robustness of the mixture. To reach the same superplasticizer dosage as that of the reference mixture, superplasticizer dosage had to be increased. The yield stress increased with an increase in nanoclay content. The addition of VMA and silica fume also resulted in a robust and stable mixture. But again, the yield stress was found to increase with the addition of both VMA and silica fume.

(d) The mix VM (0.1 % VMA) had the maximum robustness and passed both extrudability and buildability tests for a range of 0.16 - 0.19 % superplasticizer dosages. The mix NC (0.3 % nanoclay) and SF (10 % silica fume) had a working range of 0.12 - 0.14 % and 0.17 - 0.18 % superplasticizer dosages respectively.

(e) The structural build-up in the material was assessed by using evolution of yield stress with time plots, penetration curves and semi-adiabatic heat curves. The results obtained were in good agreement with each other. The VM mix had the slowest while the SF mix showed the fastest structural build-up.

2. **Addressing the issues in scaling up to a larger 3D printer**:

(a) A critical aspect to be addressed in scaling-up to a large 3D printer system is the occurrence of water drainage due to the high extrusion pressure. A desorptivity-based approach was developed to address this issue.

(b) It was found that the addition of methylcellulose caused a significant reduction in the desorptivity. This behaviour can be associated with the intermolecular sorption of water or the formation of hydrocolloidal gels with the addition of methylcellulose. The formation of the gels blocks the pores within the granular skeleton and makes it more difficult for the water to drain out, thereby decreasing the desorptivity.

(c) Based on the extrudability tests conducted on a wide range of mixes with different desorptivity values, an index (I_{norm}) was proposed to predict the occurrence of phase separation during the extrusion process. The index, I_{norm} was calculated for the maximum possible pressure of 4 kg/cm^2 and an extrusion time of 330 seconds.

(d) Since the large-scale 3D printer also allowed the extrusion of mixes containing coarse aggregates, mixes with incorporation of LECA (nominal maximum size of 10 mm) were developed. For this, the influence of coarse aggregate addition on extrudability was first examined. The addition of coarse aggregates increased the desorptivity values, which indicates that the water retention capacity of the mix decreased with the increase in coarse aggregate content. This can be attributed to lower packing density of the mixes with the higher coarse aggregate content. Further, a significant reduction in the workability occurred after the extrusion process for mixes containing coarse aggregate mainly because of dewatering that occurred during the extrusion process.

(e) From the extrudability tests of mixes containing different volume substitution of LECA, it was found that the maximum LECA content that could be incorporated without affecting extrudability is 30 % by volume. Mixes having LECA content beyond this level failed the extrudability test due to the liquid phase separation in the piston pump.

(f) The buildability of the mixes developed for the large-scale printer was assessed using uniaxial compression tests. The stress-strain response of the concrete obtained from the uniaxial test shows that the material behaviour evolved gradually from an elasto-plastic type response at relatively younger ages to strain-softening type response, more typical of hardened concrete at older ages. This evolution of compression and elastic modulus can be modelled by using existing models, such as by Perrot *et al.* (2016).

(g) It was found that both the compressive strength and the elastic modulus were higher for the mix containing LECA (30 % by volume) as compared to the control mix by 45-60 % and 25-50 % respectively. This increase can be attributed to the relatively higher amount of dewatering and the subsequent loss of workability in the CA30 mix. Hence, although the dewatering can be detrimental to extrudability, it can be considered as beneficial in improving the buildability of concrete. Finally, using existing models, a comparison was made between two mixes with respect to the critical height at which plastic and buckling type collapse may occur during printing. The lower density and the higher strength for mix containing LECA increases the critical height significantly considering a plastic collapse (56-72 %). However, for a buckling type collapse, the use of LECA indicated only a nominal increase of 4-8 %.

3. **Assessment of mechanical behaviour**:

(a) To understand the influence of layering on mechanical behaviour, the three mixes (SF, NC and VM) developed using the small-scale 3D printer were subjected to evaluation of porosity, flexural, compression and direct bond shear tests. For all the mixes considered, the porosity was found to be higher for the specimens extracted from the interfaces between horizontal and vertical layers compared to a mould cast concrete. The porosity was higher by 11-14 % for specimens extracted from interface between horizontal layers while it was 10-16 % for the specimens extracted from the interface between vertical layers. On the contrary, the porosity was found to be lower by about 6-8 % for the specimens extracted from the bulk in the printed concrete. Overall, this suggests that although the bulk portion in printed concrete is more denser as compared to mould cast concrete, the interface forms weak regions with higher porosity.

(b) For all the three mixes studied, the bond shear strength at the interface between the horizontal and vertical layers was found to be lower by 24-25 % and 22-30 % respectively as compared to the shear strength determined for mould cast concrete. This indicates a weak joint being formed at the interface between layers for the printed concrete. These results are in agreement with the trends observed in the porosity measurements.

(c) Due to the presence of weak interfaces in the printed concrete, the compressive strength was lower by 12-22 % as compared to the mould cast concrete. The compressive strength was found to be similar when tested along the three loading directions D1, D2 and D3. Therefore, no anisotropic behaviour was observed when subjected to compression loads for printed concrete.

(d) The flexural strength of the printed concrete was found to depend on the region subjected to the maximum bending moment in the three-point bending test. When tested along E1 direction, the maximum bending moment and hence the maximum flexural stress, occurs at the interface between vertical layers existing at the center of the beam. Since the interface is weaker with higher porosity relative to the bulk, this resulted in a reduced flexural strength along this direction. For the three mixes, the flexural strength was lower by about 32-40 % when tested along E1 direction. On the other hand, the flexural strength increased by 13-20 % as compared to the mould cast concrete when tested along E2 and E3 directions. This is because for these loading cases, the maximum flexural stress is induced in the bulk of the printed concretes which has a relatively lower porosity as compared to the mould cast concrete.

(e) A problem concerning the use of 3D printed structures is how the different tests conducted for characterizing its mechanical behaviour can be utilized in formulating a structural design procedure. Based on the recommendations for unreinforced concrete masonry, a structural design procedure was presented for 3D printed concrete wall elements. Expressions for assessment of axial compression, out-of-plane flexure, in-plane and out-of-plane shear are provided. Further, it is important to utilize the geometric flexibility in design of 3D printed structures. Since no additional cost is required for formwork, complex and more efficient sections can be specified by a designer to improve the load carrying capacities of 3D printed elements.

4. **Development of a rheological model**:

(a) Simulation studies are useful to examine if the mixes developed in the current study are suitable for other 3D printer system or for the same system with a different set of print parameters such as extrusion velocity or nozzle size. A rheological model was developed using a thermodynamic framework which can be useful in performing such simulation studies.

(b) In this approach, the material behaviour was characterized by using the two thermodynamic quantities, the stored energy function and the rate of dissipation function. The yielding behaviour exhibited by cementitious systems was accounted for in the model by approach of a multiple natural configurations based on the maximum rate of dissipation criterion. Thixotropy of cementitious systems was captured for by making the stored energy as a function of a structural parameter and the rate of dissipation as a function of its time derivative.

(c) To corroborate with experimental results, steady shear and step shear experiments were performed using cement paste. The predictions from the model were found to match well with the experimental data.

7.3 Outcomes from the study

The scientific and engineering outcomes from the study are summarized below.

7.3.1 Scientific outcomes

1. The rheology of concrete for special applications like 3D printing and slip-forming is quite different from that of the concretes for normal applications. This study provides a more fundamental understanding on the rheological requirements for such concretes.

2. The study has helped to understand the role of special additives like nanoclay, microsilica and VMA in formulating 3D printable concrete mixtures.

3. The desorptivity based approach presented in this work provides a more fundamental understanding on how water drainage occurs in concrete when subjected to a given pressure. This can be useful in understanding and solving issues related to concrete pumping and extrusion process.

4. Compared to the phenomenological models used in the literature, a thermodynamic based model was developed that can describe the attributes like yielding and thixotropic behaviour exhibited by cementitious systems.

7.3.2 Engineering outcomes

1. The proposed test methods and the systematic approach for mix design presented in Chapter 3 can help formulate mix design guidelines for 3D printable concretes in the future.

2. The structural design procedure that is analogous to the design of concrete masonry wall presented in Chapter 4 can help formulate guidelines for the structural design of vertical 3D printed elements.

3. The rheological model developed in the current work can be used for simulation of extrusion process. This can be useful in designing automation systems for concrete 3D printing.

7.3.3 Guidelines for mixture proportioning

One of the significant outcomes from this work is the formulation of a mixture proportioning procedure for 3D printable concrete. The following step-by-step procedure is recommended:

1. **Calibration using a reference mixture**: For a given 3D printer and set of print parameters, the required yield stress for the concrete mixture that allows both buildability and extrudability needs to be first established. For instance, for the small-scale 3D printer used in the study, a yield stress of 1.6 kPa and 1.9 kPa may be used for the nozzle sizes of 30 $\times$ 20 mm and 30 $\times$ 30 mm respectively. This can be determined by performing the extrudability and buildability tests using a reference mixture based on the procedure illustrated in Section 3.4.1. Once the yield stress

required has been established using the reference mixture, this can now be used as the basis for developing other mixture compositions.

2. **Proportion of the granular skeleton**: The proportion of the granular skeleton can be based on the optimum particle packing approach. Commercially available software such as EMMA (Elkem, 2017) can be used for this. The maximum size of aggregate is restricted by the type of pump used with the 3D printer. For screw pumps, the maximum particle size is usually restricted to 2 mm. This aspect has to be considered while selecting the size of the aggregates to be used in the mixture composition. The w/c can be selected based on the strength and durability requirements. Since cement content and w/c are known, the water content in the mix can now be calculated.

3. **Ensuring robustness**: The next step is to determine the dosage of chemical admixtures. To have a robust mixture, it is recommended to use methyl cellulose as an additive at a dosage of 0.1 % of the binder content. Alternatively, to also have high improved structural build-up, the use of silica fume at 10% replacement level or nanoclay at 0.3 % dosage may be considered.

4. **Determining the superplasticizer dosage**: The amount of superplasticizer should be determined such that the mixture has both extrudability and buildability. This can be ensured by adjusting the superplasticizer dosage in the mixture such that it has the same yield stress as that of the reference mixture.

5. **Additional requirements for large-scale 3D printer systems**: The steps illustrated above are suitable for designing printable mixtures for small-scale 3D printer systems. However, for large-scale systems such as that used in Chapter 4, it is also important to ensure that the designed mixture has sufficient water retention capacity. The index developed in Section 4.3.2 can be used to assess the resistance against the phase separation during the extrusion process.

6. **Desorptivity measurements**: For determining the index to assess phase separation, the desorptivity of the mixture has to be determined. The procedure illustrated in Section 4.2.3 can be used to measure the desorptivity value.

7. **Improving the water retention capacity**: Once the desorptivity values are determined, the index to assess phase separation can be calculated. If the index value for

the mixture is not within the permissible range suggested in Section 4.3.2, then the water retention capacity of the mixture has to be improved. For this, the dosage of methyl cellulose may be increased by increments of 0.05 % of the binder content.

8. **Final mixture design**: Since the addition of methyl cellulose modifies the yield stress of the mixture, the superplasticizer dosage must again be adjusted to have the same yield stress as that of the reference mixture. Therefore, steps 4 to 7 has to be repeated until the phase separation index for the mixture falls within the permissible range.

9. **Failure height**: Prior to printing, it is beneficial also to have an assessment of critical failure height, considering both plastic and buckling type collapse. For this, uniaxial compression tests may be conducted after different time intervals (Section 4.2.7). Then, based on the equations suggested in Section 4.3.4, a rough estimate of the failure height can be obtained. However, for a more accurate analysis, simulation studies may also be performed using the three-dimensional rheological model described in Chapter 6 of the thesis work.

7.4 Suggestions for future research

1. **Displacement-control testing for characterizing the mechanical response**: In the current study, the mechanical behaviour of 3D printable concrete was evaluated using a stress-control loading system. However, it must be understood that for a safe design, the failure of the structure must occur in a ductile manner. For this, assessing the post-crack behaviour of 3D printed concrete elements becomes important. Further, the possibility of introducing reinforcements needs to be explored. For improving ductility, the additive manufacturing of high performance fiber composites can also be considered as future extension to the current work.

2. **Using accelerators to improve buildability**: The large-scale 3D printer used in the current study can print up to a maximum height of 0.45 m. As pointed out earlier in Chapter 3, the objective of the ongoing 3D printing project in IIT Madras is to develop concrete formulations for 3D printer systems that can manufacture full-scale structures, reaching up to a height of 2 m. For such system, it is necessary to increase the structural build-up in the concrete developed in the current study.

This can be done by hydration control achieved through the use of accelerators. To introduce accelerators without reducing the time limit of printability, accelerators may be sprayed on the surface of the printed concrete. The influence of spraying accelerators post-printing on the structural build-up needs to be investigated. This is an ongoing study at IIT Madras.

3. **Simulation studies using the developed rheological model**: The rheological model developed in Chapter 6 can be used for performing simulation studies for both the extrusion process as well as for the prediction of deformation in the printed layers. Further, the rheological model developed in the current study can be improved by also accounting for the effect of cement hydration. This can be achieved by the introduction of another structural parameter in the model.

REFERENCES

1. **Assaad, J.** and **K. H. Khayat** (2004). Assessment of thixotropy of self-consolidating concrete and concrete-equivalent-mortar- effect of binder composition and content. *Materials Journal*, **101**(5), 400–408.

2. **Assaad, J.**, **K. H. Khayat**, and **H. Mesbah** (2003). Assessment of thixotropy of flowable and self-consolidating concrete. *Materials Journal*, **100**(2), 99–107.

3. **ASTM C109 / C109M-16a**, *Standard test method for compressive strength of hydraulic cement mortars (using 2-in. or [50-mm] cube specimens)*. ASTM International, 2016.

4. **ASTM C1240-15**, *Standard specification for coal fly ash and raw or calcined natural pozzolan for use in concrete*. ASTM International, 2017.

5. **ASTM C1437-15**, *Standard test method for flow of hydraulic cement mortar*. ASTM International, 2015.

6. **ASTM C150 / C150M-19a**, *Standard Specification for Portland Cement*. ASTM International, 2019.

7. **ASTM C1741-18**, *Standard Test Method for Bleed Stability of Cementitious Post-Tensioning Tendon Grout*. ASTM International, 2018.

8. **ASTM C348-14**, *Standard test method for flexural strength of hydraulic-cement mortars*. ASTM International, 2014.

9. **ASTM C403/C403M-16**, *Standard test method for time of setting of concrete mixtures by penetration resistance*. ASTM International, 2016.

10. **ASTM C618-17a**, *Standard specification for coal fly ash and raw or calcined natural pozzolan for use in concrete*. ASTM International, 2017.

11. **ASTM C989 / C989M-18a**, *Standard test method for compressive strength of hydraulic cement mortars (using 2-in. or [50-mm] cube specimens)*. ASTM International, 2018.

12. **Banfill, P. F. G.** (2006). Rheology of fresh cement and concrete. *Rheology reviews*, 61–130.

13. **Banfill, P. F. G.** and **D. C. Saunders** (1981). On the viscometric examination of cement pastes. *Cement and Concrete Research*, **11**(3), 363–370.

14. **Beverly, C. R.** and **R. I. Tanner** (1992). Numerical analysis of three-dimensional bingham plastic flow. *Journal of non-newtonian fluid mechanics*, **42**(1-2), 85–115.

15. **Bingham, E. C.**, *Fluidity and plasticity*, volume 2. McGraw-Hill, 1922.

16. **Bos, F.**, **R. Wolfs**, **Z. Ahmed**, and **T. Salet** (2016). Additive manufacturing of concrete in construction: potentials and challenges of 3D concrete printing. *Virtual and Physical Prototyping*, **11**(3), 209–225.

17. **Bourell, D. L.**, **H. L. Marcus**, **J. W. Barlow**, and **J. J. Beaman** (1992). Selective laser sintering of metals and ceramics. *International Journal of Powder Metallurgy (Princeton, New Jersey)*, **28**(4), 369–381.

18. **Brumaud, C.**, **H. Bessaies-Bey**, **C. Mohler**, **R. Baumann**, **M. Schmitz**, **M. Radler**, and **N. Roussel** (2013). Cellulose ethers and water retention. *Cement and Concrete Research*, **53**, 176–184.

19. **Bu, Y.**, **R. Spragg**, and **W. J. Weiss** (2014). Comparison of the pore volume in concrete as determined using ASTM C642 and vacuum saturation. *Advances in Civil Engineering Materials*, **3**(1), 308–315.

20. **Buchli, J.**, **M. Giftthaler**, **N. Kumar**, **M. Lussi**, **T. Sandy**, **K. Dörfler**, and **N. Hack** (2018). Digital in situ fabrication-challenges and opportunities for robotic in situ fabrication in architecture, construction, and beyond. *Cement and Concrete Research*, **112**, 66–75.

21. **Bülichen, D.**, **J. Kainz**, and **J. Plank** (2012). Working mechanism of methyl hydroxyethyl cellulose (MHEC) as water retention agent. *Cement and Concrete Research*, **42**(7), 953–959.

22. **Bülichen, D.** and **J. Plank** (2013). Water retention capacity and working mechanism of methyl hydroxypropyl cellulose (MHPC) in gypsum plaster- which impact has sulfate? *Cement and Concrete Research*, **46**, 66–72.

23. **Buscall, R.** and **L. R. White** (1987). The consolidation of concentrated suspensions. Part 1- The theory of sedimentation. *Journal of the Chemical Society, Faraday Transactions 1: Physical Chemistry in Condensed Phases*, **83**(3), 873–891.

24. **Buswell, R. A.**, **W. R. L. de Silva**, **S. Z. Jones**, and **J. Dirrenberger** (2018). 3D printing using concrete extrusion: a roadmap for research. *Cement and Concrete Research*, **112**, 37–49.

25. **Buswell, R. A.**, **R. C. Soar**, **A. G. F. Gibb**, and **A. Thorpe** (2007). Freeform construction: mega-scale rapid manufacturing for construction. *Automation in construction*, **16**(2), 224–231.

26. **Buswell, R. A.**, **A. Thorpe**, **R. C. Soar**, and **A. G. F. Gibb** (2008). Design, data and process issues for mega-scale rapid manufacturing machines used for construction. *Automation in Construction*, **17**(8), 923–929.

27. **Cheng, D. C. H.** and **F. Evans** (1965). Phenomenological characterization of the rheological behaviour of inelastic reversible thixotropic and antithixotropic fluids. *British Journal of Applied Physics*, **16**(11), 1599.

28. **Choi, M. S.**, **Y. J. Kim**, **K. P. Jang**, and **S. H. Kwon** (2014). Effect of the coarse aggregate size on pipe flow of pumped concrete. *Construction and Building Materials*, **66**, 723–730.

29. **Coussot, P.**, **Q. D. Nguyen**, **H. T. Huynh**, and **D. Bonn** (2002). Viscosity bifurcation in thixotropic, yielding fluids. *Journal of rheology*, **46**(3), 573–589.

30. **D-shape** (2019). Available from: `https://d-shape.com`. Accessed: 3 November 2019.

31. **De Koker, D.** and **G. van Zijl** (2004). Extrusion of engineered cement-based composite material. *Proceedings of BEFIB*, 1301–1310.

32. **de Souza Mendes, P. R.**, **K. R. Rajagopal**, and **R. L. Thompson** (2013). A thermodynamic framework to model thixotropic materials. *International Journal of Non-Linear Mechanics*, **55**, 48–54.

33. **Dhandapani, Y.** and **M. Santhanam** (2017). Assessment of pore structure evolution in the limestone calcined clay cementitious system and its implications for performance. *Cement and Concrete Composites*, **84**, 36–47.

34. **Dunn, J. E.** and **R. L. Fosdick** (1974). Thermodynamics, stability, and boundedness of fluids of complexity 2 and fluids of second grade. *Archive for Rational Mechanics and Analysis*, **56**(3), 191–252.

35. **Dzuy, N. Q.** and **D. V. Boger** (1983). Yield stress measurement for concentrated suspensions. *Journal of Rheology*, **27**(4), 321–349.

36. **Elkem** (2017). Available from: `www.elkem.com`. Accessed: 15 March 2017.

37. **EN 196-9**, *Methods of testing cement- part 9: heat of hydration- semi-adiabatic method*. British Standard, 2010.

38. **Erdem, T. K.**, **K. H. Khayat**, and **A. Yahia** (2009). Correlating rheology of self-consolidating concrete to corresponding concrete-equivalent mortar. *ACI Materials Journal*, **106**(2), 154.

39. **Fall, A.**, **J. Paredes**, and **D. Bonn** (2010). Yielding and shear banding in soft glassy materials. *Physical review letters*, **105**(22), 225502.

40. **Fennis, S. A.** and **J. C. Walraven** (2012). Using particle packing technology for sustainable concrete mixture design. *Heron, 57 (2012) 2*.

41. **Fernàndez-Altable, V.** and **I. Casanova** (2006). Influence of mixing sequence and superplasticiser dosage on the rheological response of cement pastes at different temperatures. *Cement and Concrete Research*, **36**(7), 1222–1230.

42. **Ferron, R. P.**, **A. Gregori**, **Z. Sun**, and **S. P. Shah** (2007). Rheological method to evaluate structural buildup in self-consolidating concrete cement pastes. *ACI materials journal*, **104**(3), 242.

43. **Feys, D.**, **R. Cepuritis**, **S. Jacobsen**, **K. Lesage**, **E. Secrieru**, and **A. Yahia** (2018). Measuring rheological properties of cement pastes: most common techniques, procedures and challenges. *RILEM technical letters*, **2**, 129–135.

44. **Funk, J. E.** and **D. R. Dinger**, *Predictive process control of crowded particulate suspensions: applied to ceramic manufacturing*. Springer Science & Business Media, 2013.

45. **Goddard, J. D.** (2006). A dissipative anisotropic fluid model for non-colloidal particle dispersions. *Journal of Fluid Mechanics*, **568**, 1–17.

46. **Govin, A.**, **M.-C. Bartholin**, **B. Biasotti**, **M. Giudici**, **V. Langella**, and **P. Grosseau** (2016). Modification of water retention and rheological properties of fresh state cement-based mortars by guar gum derivatives. *Construction and Building Materials*, **122**, 772–780.

47. **Green, K. M.**, **M. A. Carter**, **W. D. Hoff**, and **M. A. Wilson** (1999). The effects of lime and admixtures on the water-retaining properties of cement mortars. *Cement and concrete research*, **29**(11), 1743–1747.

48. **Gross, B. C.**, **J. L. Erkal**, **S. Y. Lockwood**, **C. Chen**, and **D. M. Spence** (2014). Evaluation of 3D printing and its potential impact on biotechnology and the chemical sciences.

49. **Hack, N.** and **W. V. Lauer** (2014). Mesh-mould: Robotically fabricated spatial meshes as reinforced concrete formwork. *Architectural Design*, **84**(3), 44–53.

50. **Hack, N.**, **W. V. Lauer**, **F. Gramazio**, and **M. Kohler**, Mesh mould: Robotically fabricated metal meshes as concrete formwork and reinforcement. *In Proceedings of the 11th International Symposium on Ferrocement and 3rd ICTRC International Conference on Textile Reinforced Concrete, Aachen, Germany*. 2015.

51. **Hack, N.**, **T. Wangler**, **J. Mata-Falcón**, **K. Dörfler**, **N. Kumar**, **A. N. Walzer**, **K. Graser**, **L. Reiter**, **H. Richner**, **J. Buchli**, *et al.*, Mesh mould: an on site, robotically fabricated, functional formwork. *In Second Concrete Innovation Conference (2nd CIC), Paper*, 19. 2017.

52. **Heikal, M.** and **N. S. Ibrahim** (2016). Hydration, microstructure and phase composition of composite cements containing nano-clay. *Construction and Building Materials*, **112**, 19–27.

53. **Herschel, W. H.** and **R. Bulkley** (1926). Konsistenzmessungen von gummibenzollösungen. *Colloid & Polymer Science*, **39**(4), 291–300.

54. **Hwang, H.-J.**, **S.-H. Lee**, and **E. Sakai** (2009). Rheological behavior of a slag cement paste prepared by adjusting the particle size distribution. *Journal of Ceramic Processing Research*, **10**(4), 409–413.

55. **IS 12269**, *Specification for 53 grade ordinary Portland cement*. Bureau of Indian Standards, New Delhi, 2013.

56. **Jacobs, P. F.**, *Rapid prototyping & manufacturing: fundamentals of stereolithography*. Society of Manufacturing Engineers, 1992.

57. **Jayasree, C.** and **R. Gettu** (2008). Experimental study of the flow behaviour of superplasticized cement paste. *Materials and Structures*, **41**(9), 1581–1593.

58. **Jha, K. N.**, *Formwork for concrete structures*. Tata McGraw Hill Education Private Limited, New Dilhi, India, 2012.

59. **Kabagire, D.**, **P. Diederich**, and **A. Yahia** (2015). New insight into the equivalent concrete mortar approach for self-consolidating concrete. *Journal of Sustainable Cement-Based Materials*, **4**(3-4), 215–224.

60. **Kannan, K.** and **K. R. Rajagopal** (2011). A thermodynamical framework for chemically reacting systems. *Zeitschrift für angewandte Mathematik und Physik*, **62**(2), 331–363.

61. **Kawashima, S.**, **M. Chaouche**, **D. J. Corr**, and **S. P. Shah** (2013). Rate of thixotropic rebuilding of cement pastes modified with highly purified attapulgite clays. *Cement and Concrete Research*, **53**, 112–118.

62. **Kazemian, A.**, **X. Yuan**, **E. Cochran**, and **B. Khoshnevis** (2017). Cementitious materials for construction-scale 3D printing: Laboratory testing of fresh printing mixture. *Construction and Building Materials*, **145**, 639–647.

63. **Khayat, K. H.** (1998). Viscosity-enhancing admixtures for cement-based materials—an overview. *Cement and Concrete Composites*, **20**(2-3), 171–188.

64. **Khayat, K. H.**, **A. Yahia**, and **P. Duffy** (1999). High-performance cement grout for post-tensioning applications. *Materials Journal*, **96**(4), 471–477.

65. **Khelifi, H.**, **T. Lecompte**, **A. Perrot**, and **G. Ausias** (2016). Mechanical enhancement of cement-stabilized soil by flax fibre reinforcement and extrusion processing. *Materials and Structures*, **49**(4), 1143–1156.

66. **Khoshnevis, B.** (2004). Automated construction by contour crafting—related robotics and information technologies. *Automation in construction*, **13**(1), 5–19.

67. **Khoshnevis, B.** and **R. Dutton** (1998). Innovative rapid prototyping process makes large sized, smooth surfaced complex shapes in a wide variety of materials. *Materials Technology*, **13**(2), 53–56.

68. **Khoshnevis, B.**, **D. Hwang**, **K.-T. Yao**, and **Z. Yeh** (2006). Mega-scale fabrication by contour crafting. *International Journal of Industrial and Systems Engineering*, **1**(3), 301–320.

69. **Kirchmajer, D. M.** and **R. Gorkin III** (2015). An overview of the suitability of hydrogel-forming polymers for extrusion-based 3D-printing. *Journal of Materials Chemistry B*, **3**(20), 4105–4117.

70. **Knapen, E.** and **D. Van Gemert** (2009). Cement hydration and microstructure formation in the presence of water-soluble polymers. *Cement and concrete Research*, **39**(1), 6–13.

71. **Kuder, K. G.** and **S. P. Shah** (2007). Rheology of extruded cement-based materials. *ACI materials journal*, **104**(3), 283–290.

72. **Kumar, N.**, **N. Hack**, **K. Doerfler**, **A. N. Walzer**, **G. J. Rey**, **F. Gramazio**, **M. D. Kohler**, and **J. Buchli**, Design, development and experimental assessment of a robotic end-effector for non-standard concrete applications. *In 2017 IEEE International Conference on Robotics and Automation (ICRA)*. IEEE, 2017.

73. **Lapasin, R.**, **V. Longo**, and **S. Rajgelj** (1979). Thixotropic behaviour of cement pastes. *Cement and Concrete Research*, **9**(3), 309–318.

74. **Lapasin, R.**, **A. Papo**, and **S. Rajgelj** (1983). Flow behavior of fresh cement pastes. a comparison of different rheological instruments and techniques. *Cement and Concrete Research*, **13**(3), 349–356.

75. **Le, T. T.**, **S. A. Austin**, **S. Lim**, **R. A. Buswell**, **A. G. Gibb**, and **T. Thorpe** (2012*a*). Mix design and fresh properties for high-performance printing concrete. *Materials and structures*, **45**(8), 1221–1232.

76. **Le, T. T.**, **S. A. Austin**, **S. Lim**, **R. A. Buswell**, **R. Law**, **A. G. Gibb**, and **T. Thorpe** (2012*b*). Hardened properties of high-performance printing concrete. *Cement and Concrete Research*, **42**(3), 558–566.

77. **Leutner, R.** (1979). Untersuchung des schichtenverbundes beim bituminösen oberbau. *Bitumen*, **41**(3).

78. **Lim, S.**, **R. A. Buswell**, **T. T. Le**, **S. A. Austin**, **A. G. F. Gibb**, and **T. Thorpe** (2012). Developments in construction-scale additive manufacturing processes. *Automation in construction*, **21**, 262–268.

79. **Lloret, E.**, **A. R. Shahab**, **M. Linus**, **R. J. Flatt**, **F. Gramazio**, **M. Kohler**, and **S. Langenberg** (2015). Complex concrete structures: merging existing casting techniques with digital fabrication. *Computer-Aided Design*, **60**, 40–49.

80. **Lloret-Fritschi, E.**, **L. Reiter**, **T. Wangler**, **F. Gramazio**, **M. Kohler**, and **R. J. Flatt** (2017). Smart dynamic casting: slipforming with flexible formwork-inline measurement and control. *HPC/CIC Tromsø 2017*, Paper–no.

81. **Lowke, D.**, **E. Dini**, **A. Perrot**, **D. Weger**, **C. Gehlen**, and **B. Dillenburger** (2018). Particle-bed 3D printing in concrete construction–Possibilities and challenges. *Cement and Concrete Research*, **112**, 50–65.

82. **Ma, G.**, **Z. Li**, and **L. Wang** (2018). Printable properties of cementitious material containing copper tailings for extrusion based 3D printing. *Construction and building materials*, **162**, 613–627.

83. **Macosko, C. W.** and **R. G. Larson** (1994). Rheology: principles, measurements, and applications.

84. **Málek, J.** and **K. R. Rajagopal** (2008). A thermodynamic framework for a mixture of two liquids. *Nonlinear Analysis: Real World Applications*, **9**(4), 1649–1660.

85. **Martinez, S.**, **A. Jardon**, **A. Gimenez**, **C. Balaguer**, **J. M. Navarro**, and **C. Barcena**, Robotized lean assembly in the building industry. *In Proceedings of the 25th International Symposium on Automation and Robotics in Construction (ISARC)*. 2008.

86. **Mehta, P. K.** and **P. J. Monteiro**, *Concrete microstructure, properties and materials*. McGraw-Hill Education, 2006.

87. **Mewis, J.** and **N. J. Wagner** (2009). Thixotropy. *Advances in Colloid and Interface Science*, **147**, 214–227.

88. **Mohamed, O. A.**, **S. H. Masood**, and **J. L. Bhowmik** (2015). Optimization of fused deposition modeling process parameters: a review of current research and future prospects. *Advances in Manufacturing*, **3**(1), 42–53.

89. **Nehdi, M.** and **M.-A. Rahman** (2004). Effect of geometry and surface friction of test accessory on oscillatory rheological properties of cement pastes. *Materials Journal*, **101**(5), 416–424.

90. **Nerella, V.**, **M. Krause**, **M. Näther**, and **V. Mechtcherine**, Studying printability of fresh concrete for formwork free concrete on-site 3D printing technology (conprint3d). *In Proceeding for the 25th conference on rheology of building materials*. 2016.

91. **Nessim, A. A.** and **R. L. Wajda** (1965). The rheology of cement pastes and fresh mortars. *Magazine of Concrete Research*, **17**(51), 59–68.

92. **Oldroyd, J. G.** (1958). Non-newtonian effects in steady motion of some idealized elastico-viscous liquids. *Proceedings of the Royal Society of London. Series A. Mathematical and Physical Sciences*, **245**(1241), 278–297.

93. **Panda, B.**, **J. H. Lim**, and **M. J. Tan** (2019). Mechanical properties and deformation behaviour of early age concrete in the context of digital construction. *Composites Part B: Engineering*, **165**, 563–571.

94. **Panda, B.**, **S. C. Paul**, **L. J. Hui**, **Y. W. D. Tay**, and **M. J. Tan** (2017*a*). Additive manufacturing of geopolymer for sustainable built environment. *Journal of Cleaner Production*, **167**, 281–288.

95. **Panda, B.**, **S. C. Paul**, **N. A. N. Mohamed**, **Y. W. D. Tay**, and **M. J. Tan** (2018). Measurement of tensile bond strength of 3D printed geopolymer mortar. *Measurement*, **113**, 108–116.

96. **Panda, B.**, **S. C. Paul**, and **M. J. Tan** (2017*b*). Anisotropic mechanical performance of 3D printed fiber reinforced sustainable construction material. *Materials Letters*, **209**, 146–149.

97. **Papo, A.** (1988). Rheological models for cement pastes. *Materials and Structures*, **21**(1), 41–46.

98. **Papo, A.** and **L. Piani** (2004). Effect of various superplasticizers on the rheological properties of portland cement pastes. *Cement and Concrete Research*, **34**(11), 2097–2101.

99. **Patural, L.**, **P. Marchal**, **A. Govin**, **P. Grosseau**, **B. Ruot**, and **O. Deves** (2011). Cellulose ethers influence on water retention and consistency in cement-based mortars. *Cement and Concrete Research*, **41**(1), 46–55.

100. **Paul, S. C.**, **Y. W. D. Tay**, **B. Panda**, and **M. J. Tan** (2018). Fresh and hardened properties of 3d printable cementitious materials for building and construction. *Archives of Civil and Mechanical Engineering*, **18**(1), 311–319.

101. **Pegna, J.** (1997). Exploratory investigation of solid freeform construction. *Automation in construction*, **5**(5), 427–437.

102. **Peled, A.**, **M. F. Cyr**, and **S. P. Shah** (2000). High content of fly ash (class f) in extruded cementitious composites. *Materials Journal*, **97**(5), 509–517.

103. **Perrot, A.**, **A. Pierre**, **S. Vitaloni**, and **V. Picandet** (2015). Prediction of lateral form pressure exerted by concrete at low casting rates. *Materials and Structures*, **48**(7), 2315–2322.

104. **Perrot, A.**, **D. Rangeard**, **V. N. Nerella**, and **V. Mechtcherine** (2018). Extrusion of cement-based materials-an overview. *RILEM Technical Letters*, **3**, 91–97.

105. **Perrot, A.**, **D. Rangeard**, and **A. Pierre** (2016). Structural built-up of cement-based materials used for 3D-printing extrusion techniques. *Materials and Structures*, **49**(4), 1213–1220.

106. **Pham, D. T.** and **R. S. Gault** (1998). A comparison of rapid prototyping technologies. *International Journal of machine tools and manufacture*, **38**(10-11), 1257–1287.

107. **PMAY-HFA** (2019). Available from: `https://pmaymis.gov.in`. Accessed: 3 November 2019.

108. **Qian, Y.** and **G. De Schutter** (2018). Enhancing thixotropy of fresh cement pastes with nanoclay in presence of polycarboxylate ether superplasticizer (pce). *Cement and Concrete Research*, **111**, 15–22.

109. **Qian, Y.** and **S. Kawashima** (2016). Use of creep recovery protocol to measure static yield stress and structural rebuilding of fresh cement pastes. *Cement and Concrete Research*, **90**, 73–79.

110. **Quanji, Z.**, **G. R. Lomboy**, and **K. Wang** (2014). Influence of nano-sized highly purified magnesium alumino silicate clay on thixotropic behavior of fresh cement pastes. *Construction and Building Materials*, **69**, 295–300.

111. **Rajagopal, K. R.** (1995). Multiple configurations in continuum mechanics. *Reports of the institute for computational and applied mechanics*, **6**.

112. **Rajagopal, K. R.** and **A. R. Srinivasa** (1997). On the inelastic behavior of solids-part II. energetics of deformation twinning. *Int. J. Plasticity*, **13**(1/2), 1–35.

113. **Rajagopal, K. R.** and **A. R. Srinivasa** (1998). Mechanics of the inelastic behavior of materials. Part II: Inelastic response. *International Journal of Plasticity*, **14**(10-11), 969–995.

114. **Rajagopal, K. R.** and **A. R. Srinivasa** (1999). Thermomechanical modeling of shape memory alloys. *ZAMP*, **50**, 459–496.

115. **Rajagopal, K. R.** and **A. R. Srinivasa** (2000). A thermodynamic frame work for rate type fluid models. *Journal of Non-Newtonian Fluid Mechanics*, **88**(3), 207–227.

116. **Rajagopal, K. R.** and **A. R. Srinivasa** (2004*a*). On the thermomechanics of materials that have multiple natural configurations part I: Viscoelasticity and classical plasticity. *Zeitschrift für angewandte Mathematik und Physik ZAMP*, **55**(5), 861–893.

117. **Rajagopal, K. R.** and **A. R. Srinivasa** (2004*b*). On the thermomechanics of materials that have multiple natural configurations. part II: Twinning and solid to solid phase transformation. *Zeitschrift für angewandte Mathematik und Physik*, **55**(6), 1074–1093.

118. **Ramge, P.** and **L. Lohaus**, Robustness by mix design–a new approach for mixture proportioning of scc. *In Design, Production and Placement of Self-Consolidating Concrete*. Springer, 2010, 37–49.

119. **Rao, I. J.** and **K. R. Rajagopal** (2002). A thermodynamic framework for the study of crystallization in polymers. *Zeitschrift für angewandte Mathematik und Physik ZAMP*, **53**(3), 365–406.

120. **Repetier-Host** (2019). Available from: `www.repetier.com`. Accessed: 3 November 2019.

121. **Roussel, N.** (2005). Steady and transient flow behaviour of fresh cement pastes. *Cement and concrete research*, **35**(9), 1656–1664.

122. **Roussel, N.** (2006). A thixotropy model for fresh fluid concretes: theory, validation and applications. *Cement and Concrete Research*, **36**(10), 1797–1806.

123. **Roussel, N.** (2018*a*). Rheological requirements for printable concretes. *Cement and Concrete Research*, **112**, 76 – 85.

124. **Roussel, N.** (2018*b*). Rheological requirements for printable concretes. *Cement and Concrete Research*, **112**, 76–85.

125. **Roussel, N.**, **R. Le Roy**, and **P. Coussot** (2004). Thixotropy modelling at local and macroscopic scales. *Journal of non-newtonian fluid mechanics*, **117**(2-3), 85–95.

126. **Rushing, T. S.**, **G. Al-Chaar**, **B. A. Eick**, **J. Burroughs**, **J. Shannon**, **L. Barna**, and **M. Case** (2017). Investigation of concrete mixtures for additive construction. *Rapid Prototyping Journal*, **23**(1).

127. **Saak, A. W.**, **H. M. Jennings**, and **S. P. Shah** (2001). The influence of wall slip on yield stress and viscoelastic measurements of cement paste. *Cement and concrete research*, **31**(2), 205–212.

128. **Sandy, T.**, **M. Giftthaler**, **K. Dörfler**, **M. Kohler**, and **J. Buchli**, Autonomous repositioning and localization of an in situ fabricator. *In 2016 IEEE International Conference on Robotics and Automation (ICRA)*. IEEE, 2016.

129. **Sanjayan, J. G.**, **B. Nematollahi**, **M. Xia**, and **T. Marchment** (2018). Effect of surface moisture on inter-layer strength of 3D printed concrete. *Construction and Building Materials*, **172**, 468–475.

130. **Saric-Coric, M.**, **K. H. Khayat**, and **A. Tagnit-Hamou** (2003). Performance characteristics of cement grouts made with various combinations of high-range water reducer and cellulose-based viscosity modifier. *Cement and Concrete Research*, **33**(12), 1999–2008.

131. **Schultz, M. A.** and **L. J. Struble** (1993). Use of oscillatory shear to study flow behavior of fresh cement paste. *Cement and Concrete Research*, **23**(2), 273–282.

132. **Shao, Y.**, **S. Marikunte**, and **S. P. Shah** (1995). Extruded fiber-reinforced composites. *Concrete international*, **17**(4), 48–53.

133. **Shao, Y.** and **S. P. Shah**, High performance fiber-cement composites by extrusion processing. *In Materials for the New Millennium:*. ASCE, 1996.

134. **Sharma, A.** (2019). *Cost-benefit analysis of 3D printing of concrete structures*. Master's thesis, department of civil engineering, Indian Institute of Technology Madras, India.

135. **Slic3r** (2019). Available from: `https://slic3r.org`. Accessed: 3 November 2019.

136. **Srinivasa, A. R.** (2001). Large deformation plasticity and the poynting effect. *International Journal of Plasticity*, **17**(9), 1189–1214.

137. **Srinivasan, R.**, **D. DeFord**, and **S. P. Shah** (1999). The use of extrusion rheometry in the development of extruded fiber-reinforced cement composites. *Concrete Science and Engineering*, **1**(1), 26–36.

138. **Struble, L. J.** and **M. A. Schultz** (1993). Using creep and recovery to study flow behavior of fresh cement paste. *Cement and concrete research*, **23**(6), 1369–1379.

139. **Takashima, H.**, **K. Miyagai**, **T. Hashida**, and **V. C. Li** (2003). A design approach for the mechanical properties of polypropylene discontinuous fiber reinforced cementitious composites by extrusion molding. *Engineering fracture mechanics*, **70**(7-8), 853–870.

140. **Tay, Y. W. D.**, **B. Panda**, **S. C. Paul**, **N. A. Noor Mohamed**, **M. J. Tan**, and **K. F. Leong** (2017). 3D printing trends in building and construction industry: a review. *Virtual and Physical Prototyping*, **12**(3), 261–276.

141. **TEK 14-7C**, *Allowable stress design of concrete masonry based on the 2012 IBC and 2011 MSJC*. National Concrete Masonry Association, 2013.

142. **Terzaghi, K.**, *Theoretical Soil Mechanics*. John Wiley Sons, Inc., Hoboken, NJ, USA, 1965.

143. **TotalKustom** (2019). Available from: `http://www.totalkustom.com/`. Accessed: 3 November 2019.

144. **Tregger, N. A.**, **M. E. Pakula**, and **S. P. Shah** (2010). Influence of clays on the rheology of cement pastes. *Cement and concrete research*, **40**(3), 384–391.

145. **Tvasta – Industrial 3D Printing** (2019). Available from: `www.tvastagroup.in`. Accessed: 3 November 2019.

146. **Van Der Vurst, F.**, **S. Grünewald**, **D. Feys**, **K. Lesage**, **L. Vandewalle**, **J. Vantomme**, and **G. De Schutter** (2017). Effect of the mix design on the robustness of fresh self-compacting concrete. *Cement and Concrete Composites*, **82**, 190–201.

147. **Voigt, T.**, **T. Malonn**, and **S. P. Shah** (2006). Green and early age compressive strength of extruded cement mortar monitored with compression tests and ultrasonic techniques. *Cement and Concrete Research*, **36**(5), 858–867.

148. **Voigt, T.**, **J.-J. Mbele**, **K. Wang**, and **S. P. Shah** (2010). Using fly ash, clay, and fibers for simultaneous improvement of concrete green strength and consolidatability for slip-form pavement. *Journal of Materials in Civil Engineering*, **22**(2), 196–206.

149. **Wallevik, J. E.** (2005). Thixotropic investigation on cement paste: Experimental and numerical approach. *Journal of non-newtonian fluid mechanics*, **132**(1-3), 86–99.

150. **Wallevik, J. E.** (2009). Rheological properties of cement paste: thixotropic behavior and structural breakdown. *Cement and Concrete Research*, **39**(1), 14–29.

151. **Wangler, T.**, **E. Lloret**, **L. Reiter**, **N. Hack**, **F. Gramazio**, **M. Kohler**, **M. Bernhard**, **B. Dillenburger**, **J. Buchli**, **N. Roussel**, *et al.* (2016). Digital concrete: opportunities and challenges. *RILEM Technical Letters*, **1**, 67–75.

152. **Williams, D. A.**, **A. W. Saak**, and **H. M. Jennings** (1999). The influence of mixing on the rheology of fresh cement paste. *Cement and Concrete Research*, **29**(9), 1491–1496.

153. **Winsun** (2019). Available from: `www.winsun3d.com`. Accessed: 3 November 2019.

154. **Wohlers, T.** (1998). Rapid prototyping & tooling state of the industry: 1998 worldwide progress report. *Materials Technology*, **13**(4), 174–176.

155. **Wolfs, R. J. M.**, **F. P. Bos**, and **T. A. M. Salet** (2018). Early age mechanical behaviour of 3D printed concrete: Numerical modelling and experimental testing. *Cement and Concrete Research*, **106**, 103–116.

156. **Zhou, S.-C.**, **H.-L. Lv**, **N. Li**, and **J. Zhang** (2019). Effects of chemical admixtures on the working and mechanical properties of ordinary dry-mixed mortar. *Advances in Materials Science and Engineering*, **2019**.

APPENDIX A

3D PRINTED STRUCTURES AND ELEMENTS

A.1 A 3D printed modular structure

A structure of size 1.8 × 0.8 × 2 m was fabricated by assembling modules fabricated using the large-scale 3D printer. It is India's first full-scale structure made with 3D printed elements. The concrete formulation used was the control mix presented in Chapter 3 of the thesis. Each module consisted of 14 to 17 layers. Each layer filament was extruded through a 15 × 15 mm square nozzle. The total height of the modules varied from 190 to 240 mm. Each module consisted of a hollow structure with two horizontal layers forming the perimeter. The print speed used was 30 mm/s and for this print speed, the time gap between the two successive horizontal and vertical layers was about 2.5 and 5 minutes respectively.

The different stages in the construction of the modular structure is shown in Figure A.1. The first stage was the printing of each individual module as shown in Figure A.1a. The module after printing was moved from print bed and cured using wet hessian cloth. The second stage involved assembling two modules by aligning them horizontally as shown in Figure A.1b to form the entire perimeter of the structure. Cement mortar was used to join the different modules together. In this manner, many sets of the horizontally aligned modules were stacked one above the other to from the entire structure. After assembling of all the modules, 12 mm diameter reinforcement bars were inserted manually through holes provided at the four corners of the structure. The reinforcement was held in place by filling the hollow sections by pouring cement grout. The roof of the structure was made using a wooden panel and the base of structure was a precast concrete slab made by conventional casting. The completed and fully assembled structure is shown in Figure A.1c.

(a)

(b)

(c)

Figure A.1: (a) Printing of each individual module (b) Modules are aligned to form the full perimeter of the structure (c) Completed 3D printed modular structure with a wooden panel roof

A.2 3D printed furniture

The control mix was also used in the fabrication of 3D printed furniture. Some examples are shown in Figures A.2 and A.3. The furniture printing was done using 20 mm circular nozzles as shown in Figures A.2a and A.3a. Since the perimeters were small, the time gaps between the horizontal layers was less than 1 minute and that between the vertical layers was less than 2 minutes. Therefore, to ensure a faster structural build-up in the mix, an aluminum sulphate based accelerator was sprayed from outside post-printing. The effect of spraying on increasing buildability is an ongoing study at IIT Madras.

(a) (b)

Figure A.2: (a) Printing of a chair (b) Completed structure

(a) (b)

Figure A.3: (a) Printing of a stool (b) Completed stool

APPENDIX B

INDIVIDUAL RESULTS OF MECHANICAL TESTS

The values obtained during the assessment of mechanical properties presented in Chapter 5 are summarized below.

Table B.1: Individual test results for the porosity assessment of SF mix

Sample type	Sample no.	Porosity value (%)	Average porosity (%)
Mould cast	1	9.53	9.8 ± 0.7
	2	9.0	
	3	10.1	
	4	10.6	
Printed - bulk	1	8.8	9.1 ± 0.7
	2	8.3	
	3	9.4	
	4	9.9	
Printed - vertical layers	1	11.0	11.3 ± 0.8
	2	10.4	
	3	11.6	
	4	11.2	
Printed - horizontal layers	1	10.8	11.1 ± 0.8
	2	10.2	
	3	11.4	
	4	12.0	

Table B.2: Individual test results for the porosity assessment of NC mix

Sample type	Sample no.	Porosity value (%)	Average porosity (%)
Mould cast	1	9.9	10.1 ± 0.6
	2	9.4	
	3	10.3	
	4	10.8	
Printed - bulk	1	9.1	9.4 ± 0.7
	2	8.6	
	3	9.4	
	4	10.2	
Printed - vertical layers	1	12.3	11.3 ± 0.8
	2	11.1	
	3	10.4	
	4	11.4	
Printed - horizontal layers	1	12.5	11.4 ± 0.8
	2	10.7	
	3	11.4	
	4	11.0	

Table B.3: Individual test results for the porosity assessment of VM mix

Sample type	Sample no.	Porosity value (%)	Average porosity (%)
Mould cast	1	11.0	10.4 ± 0.6
	2	10.74	
	3	10.20	
	4	9.66	
Printed - bulk	1	10.4	9.6 ± 0.7
	2	9.3	
	3	9.4	
	4	8.7	
Printed - vertical layers	1	12.4	11.5 ± 0.8
	2	11.9	
	3	11.3	
	4	10.5	
Printed - horizontal layers	1	12.7	11.6 ± 0.9
	2	11.0	
	3	11.9	
	4	10.7	

Table B.4: Individual test results for the shear strength of SF mix

Sample type	Sample no.	Shear strength (N/mm^2)	Average shear strength (N/mm^2)
Mould cast	1	8.5	8 ± 0.3
	2	7.6	
	3	7.8	
	4	8.0	
	5	7.8	
	6	8.1	
Printed - vertical layers	1	6.3	5.7 ± 0.4
	2	5.2	
	3	5.6	
	4	5.4	
	5	5.6	
	6	5.9	
Printed - horizontal layers	1	6.6	6.1 ± 0.4
	2	5.8	
	3	6.1	
	4	5.5	
	5	6.1	
	6	6.3	

Table B.5: Individual test results for the shear strength of NC mix

Sample type	Sample no.	Shear strength (N/mm^2)	Average shear strength (N/mm^2)
Mould cast	1	6.3	5.7 ± 0.5
	2	5.0	
	3	5.7	
	4	6.1	
	5	5.4	
	6	5.9	
Printed - vertical layers	1	6.3	5.7 ± 0.4
	2	5.2	
	3	5.6	
	4	5.4	
	5	5.6	
	6	5.9	
Printed - horizontal layers	1	6.7	5.9 ± 0.5
	2	5.5	
	3	5.7	
	4	5.4	
	5	5.9	
	6	6.4	

Table B.6: Individual test results for the shear strength of VM mix

Sample type	Sample no.	Shear strength (N/mm^2)	Average shear strength (N/mm^2)
Mould cast	1	7.5	7.2 ± 0.3
	2	7.0	
	3	7.1	
	4	6.9	
	5	7.1	
	6	7.7	
Printed - vertical layers	1	6.0	5.6 ± 0.5
	2	5.3	
	3	5.4	
	4	5.2	
	5	5.2	
	6	6.4	
Printed - horizontal layers	1	5.5	5.5 ± 0.4
	2	6.1	
	3	5.2	
	4	5.3	
	5	5.0	
	6	5.7	

Table B.7: Individual test results for the compressive strength of SF mix

Sample type	Sample no.	Comp. strength (N/mm^2)	Average comp. strength (N/mm^2)
Mould cast	1	78.7	74.1 ± 3.5
	2	79	
	3	73	
	4	76.7	
	5	77.5	
	6	73.7	
	7	76.6	
	8	71.7	
	9	72.6	
	10	68.7	
	11	69.3	
	12	72.3	
Printed - direction D1	1	60.6	61.9 ± 5.1
	2	56.9	
	3	61.4	
	4	72.7	
	5	55.6	
	6	60.4	
	7	67	
	8	56.9	
	9	58	
	10	61.6	
	11	66	
	12	66	
Printed - direction D2	1	62.1	59.8 ± 4.8
	2	60.6	
	3	57.8	
	4	60.2	
	5	54.7	
	6	50.4	
	7	64.3	
	8	56.2	
	9	58.9	
	10	64.7	
	11	60	
	12	68.3	
Printed - direction D3	1	59.2	58.3 ± 4.9
	2	64.5	
	3	58.6	
	4	55.2	
	5	58.8	
	6	51.4	
	7	55	
	8	60.5	
	9	55.6	
	10	69.6	
	11	54.1	
	12	58.1	

Table B.9: Individual test results for the compressive strength of NC mix

Sample type	Sample no.	Comp. strength (N/mm^2)	Average comp. strength (N/mm^2)
Mould cast	1	73.4	72.1 ± 3.9
	2	67.1	
	3	74.9	
	4	71.6	
	5	75.7	
	6	76.1	
	7	71.5	
	8	65.7	
	9	76.1	
	10	70.3	
	11	67	
	12	76.3	
Printed - direction D1	1	68.9	61.9 ± 4.9
	2	57.6	
	3	56.8	
	4	67.6	
	5	64.7	
	6	65.7	
	7	67.9	
	8	56	
	9	58.6	
	10	56.2	
	11	60.5	
	12	62.4	
Printed - direction D2	1	54.2	58.7 ± 5.0
	2	55.4	
	3	54.2	
	4	67.8	
	5	55	
	6	67.8	
	7	62.4	
	8	58.4	
	9	54.4	
	10	61.2	
	11	56.2	
	12	57.8	
Printed - direction D3	1	64.5	58.0 ± 5.1
	2	59.1	
	3	57.9	
	4	54.1	
	5	61.2	
	6	62.9	
	7	52.8	
	8	50.3	
	9	55.7	
	10	51.2	
	11	61.9	
	12	64.4	

Table B.11: Individual test results for the compressive strength of VM mix

Sample type	Sample no.	Comp. strength (N/mm^2)	Average comp. strength (N/mm^2)
Mould cast	1	67.7	68.3 ± 3.3
	2	73.2	
	3	68.7	
	4	67.5	
	5	69.4	
	6	63.7	
	7	72.8	
	8	63.1	
	9	71.7	
	10	64.8	
	11	69.3	
	12	68.3	
Printed - direction D1	1	67.6	59.6 ± 5.4
	2	57.7	
	3	63.4	
	4	49.6	
	5	53	
	6	63.7	
	7	61.6	
	8	65.5	
	9	62.1	
	10	55.6	
	11	55.3	
	12	60.3	
Printed - direction D2	1	60.7	57.7 ± 5.2
	2	56.4	
	3	49.7	
	4	59.6	
	5	65.1	
	6	62.2	
	7	53.7	
	8	60.1	
	9	57.3	
	10	64.1	
	11	49	
	12	55.2	
Printed - direction D3	1	62.4	57.0 ± 5
	2	50.5	
	3	54.8	
	4	62.1	
	5	57.2	
	6	62.6	
	7	54	
	8	56	
	9	53.5	
	10	48.9	
	11	64.1	
	12	58.7	

Table B.13: Individual test results for the flexural strength of SF mix

Sample type	Sample no.	Flexural strength (N/mm^2)	Average flexural strength (N/mm^2)
Mould cast	1	8.9	9.5 ± 0.4
	2	10	
	3	9.4	
	4	9.9	
	5	9.7	
	6	9.6	
	7	9.9	
	8	9.3	
	9	9.3	
	10	8.9	
	11	10	
	12	9.8	
Printed - direction E1	1	7.4	5.7 ± 1.1
	2	4.4	
	3	7.1	
	4	5.2	
	5	4.4	
	6	4.9	
	7	6.7	
	8	4.8	
	9	6.3	
	10	6	
	11	4.9	
	12	6.8	
Printed - direction E2	1	10.6	10.7 ± 0.7
	2	11.3	
	3	11.5	
	4	10.5	
	5	10.5	
	6	12.1	
	7	10.3	
	8	10.6	
	9	10.5	
	10	11.8	
	11	10	
	12	10	
Printed - direction E3	1	10.3	11.2 ± 0.8
	2	11	
	3	10.2	
	4	12	
	5	10.7	
	6	12.1	
	7	12.1	
	8	10.8	
	9	12.1	
	10	10.2	
	11	11.7	
	12	11.8	

Table B.15: Individual test results for the flexural strength of NC mix

Sample type	Sample no.	Flexural strength (N/mm^2)	Average flexural strength (N/mm^2)
Mould cast	1	10.5	10.0 ± 0.4
	2	10.2	
	3	10	
	4	9.6	
	5	10.4	
	6	10.5	
	7	9.5	
	8	10	
	9	9.7	
	10	10.5	
	11	10.2	
	12	9.5	
Printed - direction E1	1	6.2	6.4 ± 0.9
	2	5.9	
	3	6.9	
	4	5.2	
	5	6.6	
	6	7	
	7	4.7	
	8	6.9	
	9	6	
	10	7.2	
	11	7.6	
	12	7.5	
Printed - direction E2	1	12.1	11.4 ± 0.7
	2	11.6	
	3	12.2	
	4	10.2	
	5	10.3	
	6	11.1	
	7	11.8	
	8	11.1	
	9	11.9	
	10	12.4	
	11	11.6	
	12	11.3	
Printed - direction E3	1	13	11.9 ± 1
	2	12	
	3	10.6	
	4	13	
	5	13.1	
	6	11.3	
	7	10.6	
	8	10.7	
	9	12.4	
	10	11.3	
	11	13	
	12	12.1	

Table B.17: Individual test results for the flexural strength of VM mix

Sample type	Sample no.	Flexural strength (N/mm^2)	Average flexural strength (N/mm^2)
Mould cast	1	8.3	9.1 ± 0.5
	2	9.5	
	3	9.3	
	4	9.4	
	5	9.6	
	6	9.3	
	7	9.3	
	8	9.7	
	9	9.6	
	10	8.4	
	11	8.3	
	12	9.1	
Printed - direction E1	1	6.1	6.1 ± 1
	2	5.8	
	3	8	
	4	5.9	
	5	7.2	
	6	7.6	
	7	5.6	
	8	6.4	
	9	5	
	10	6.1	
	11	5.5	
	12	4.7	
Printed - direction E2	1	9	10.5 ± 1
	2	11.4	
	3	9.3	
	4	10.6	
	5	10.9	
	6	11.5	
	7	9.3	
	8	10.4	
	9	11.4	
	10	12	
	11	11	
	12	9.9	
Printed - direction E3	1	11.3	10.9 ± 0.7
	2	10.2	
	3	11.3	
	4	10.3	
	5	11.5	
	6	12.3	
	7	10.1	
	8	10.4	
	9	10.2	
	10	10.6	
	11	11.4	
	12	11.5	

APPENDIX C

REPRESENTATIVE MORTAR FOR RHEOLOGICAL TESTING USING CONCRETE EQUIVALENT MORTAR (CEM) METHOD

C.1 Representative mortar for VM mix

In the concrete equivalent mortar (CEM) method, the larger size aggregates (quartz sand 1 and quartz sand 2) in the VM mix are replaced with an equivalent amount of quartz powder such that the equivalent mortar and the original VM mix has the same total surface area of aggregates. The steps involved in proportioning the CEM mix are as follows:-

1. At first, the specific surface area (SSA) of quartz sand 1, quartz sand 2 and quartz powder were determined as shown in Tables C.1 to C.3 respectively. To determine SSA for quartz sand 1 and quartz sand 2, sieve analysis was performed using 1 kg of the aggregate samples and the volume retained on each sieve size was noted (see column 2 of Tables C.1 and C.2). For quartz powder, the percentage passing determined by the laser diffraction method was used to determine the aggregate volume for different size ranges for a total of 1 kg aggregate sample (see column 2 of Table C.3). The surface area calculations were performed assuming that all aggregate particles are spherical in shape. When a fraction of the total aggregate sieved, retains in between two successive sieves, the diameter of all particles that retained was assumed to be the average of the two sieve sizes just above and below it (see column 3 of Tables C.1 to C.3).

2. The amount of aggregates required for 1 m^3 of the VM mix (from Table 3.5) is shown in column 2 of Table C.4. The SSA for the different aggregates (obtained by dividing the total surface area obtained from Tables C.1 to C.3 by the weight of total aggregate sample (1 kg)) is shown in column 3 of Table C.4. By multiplying the

aggregate quantity in column 2 with SSA, the total surface area of aggregates in 1 m^3 of VM mix can be calculated as shown in column 4 of Table C.4.

Table C.1: Specific surface area calculation for quartz sand 1

Sieve size ($\times 10^{-6}$ m)	Volume of material retained on each sieve ($\times 10^{-6}$ m^3)	Dia. of particle ($\times 10^{-5}$ m) D_i	Surface area of one particle ($\times 10^{-9}$ m^2) πD_i^2	Volume of one particle ($\times 10^{-14}$ m^3) $\pi D_i^3/6$	No. of particles ($\times 10^3$) column 2 / column 5	Total surface area (m^2) column 4 $\times$ column 6
75	7.84	3.75	4.42	2.76	284213.07	1.25
150	30.25	11.25	39.74	74.51	40595.12	1.61
300	82.53	22.50	158.96	596.11	13844.28	2.20
600	151.35	45.00	635.85	4768.88	3173.71	2.02
1180	80.26	89.00	2487.19	36893.38	217.55	0.54
2360	26.56	177.00	9837.31	290200.53	9.15	0.09
						$\sum = 7.71$

Table C.2: Specific surface area calculation for quartz sand 2

Sieve size ($\times 10^{-6}$ m)	Volume of material retained on each sieve ($\times 10^{-5}$ m^3)	Dia. of particle ($\times 10^{-5}$ m) D_i	Surface area of one particle ($\times 10^{-9}$ m^2) πD_i^2	Volume of one particle ($\times 10^{-14}$ m^3) $\pi D_i^3/6$	No. of particles ($\times 10^4$) column 2 / column 5	Total surface area (m^2) column 4 $\times$ column 6
75	0.00	3.75	4.42	2.76	0.00	0.00
150	1.85	11.25	39.74	74.51	2477.07	0.98
300	4.62	22.50	158.96	596.11	775.37	1.23
600	8.68	45.00	635.85	4768.88	182.01	1.16
1180	12.38	89.00	2487.19	36893.38	33.55	0.83
2360	10.35	177.00	9837.31	290200.53	3.57	0.35
						$\sum = 4.55$

3. The amount of quartz powder in CEM must be such the total surface area of aggregates in the VM mix and the CEM must be the same. Therefore,

$$\begin{aligned}\text{Quartz powder in CEM} &= \frac{\text{Total surface area of all aggregates in VM mix } (m^2)}{\text{SSA of quartz powder } (m^2/kg)} \\ &= \frac{110697.24}{215.80} \\ &= 513\,kg \end{aligned} \tag{C.1}$$

Table C.3: Specific surface area calculation for quartz powder

Particle size ($\times 10^{-6}$ m)	Volume of 1 kg material sample between 2 successive size range ($\times 10^{-5}$ m^3)	Dia. of particle ($\times 10^{-6}$ m)	Surface area of one particle ($\times 10^{-11}$ m^2)	Volume of one particle ($\times 10^{-18}$ m^3)	No. of particles ($\times 10^8$)	Total surface area (m^2)
		D_i	πD_i^2	$\pi D_i^3/6$	column 2 / column 5	column 4 × column 6
4.30	3.79	2.15	1.45	5.20	72828.66	105.71
8.26	3.79	6.28	12.38	129.62	2922.39	36.19
12.98	3.79	10.62	35.41	626.83	604.29	21.40
18.02	3.79	15.50	75.44	1948.83	194.37	14.66
23.97	3.79	21.00	138.41	4843.13	78.21	10.83
30.75	3.79	27.36	235.05	10718.32	35.34	8.31
37.60	3.79	34.18	366.73	20888.34	18.13	6.65
44.86	3.79	41.23	533.77	36679.08	10.33	5.51
54.17	3.79	49.52	769.84	63531.45	5.96	4.59
62.05	1.89	58.11	1060.31	102690.68	1.84	1.96
						$\sum = 215.80$

Table C.4: SSA required for CEM

Quantity of aggregates in 1 m^3 of the VM mix (kg)		SSA (m^2/kg)	Total surface area (m^2)
Quartz sand 1	369	7.71	2844.99
Quartz sand 2	369	4.55	1678.95
Quartz powder	492	215.80	106173.6
			$\sum = 110697.24$

4. The amount of binder content in 1 m^3 of VM mix is 738 kg (from Table 3.5). Therefore, the aggregate to binder ratio for CEM mix is 513:738 (41:59). The water-

cement ratio and the dosage of chemical admixtures in CEM are to be maintained the same as that in the original VM mix. Based on this, the final mixture proportion for 1 m^3 of CEM is calculated and summarized in Table C.5.

C.2 Comparison of CEM with the VM mix

In order to examine if the CEM mix is truly representative of the VM mix, extrudability test, yield stress measurement and flow table test were performed on CEM mix based on the procedures given in section 3.3.1. The comparisons of the test results with that obtained for the original VM mix are shown in Table C.6.

Clearly, the test results indicate that the CEM mix is much stiffer than the VM mix. The CEM mix had a yield stress value of 3.5 kPa which is outside the range of 1.5 to 2.5 kPa suggested for the small-scale 3D printer. As a result, the CEM mix did not pass the extrudability test. The flow value obtained for the CEM mix was also much lower than that obtained for the VM mix. Therefore, it was concluded that it was not possible to obtain a representative mortar by the CEM method for the VM mix.

Table C.5: Mixture proportion for CEM

Material	Quantity (kg/m^3)
Cement	885
Fly ash	221
Quartz powder	768
Water	354
Superplasticizer	5.85 (0.18 %)
VMA	1.11 (0.1 %)

Table C.6: Comparison of test results of CEM and VM mix

Test results	VM mix	CEM mix
Yield stress (kPa)	1.6 ± 0.3	3.5 ± 0.4
Flow value (%)	80 ± 5	40 ± 5
Extrudability (pass/fail)	Pass	Fail

APPENDIX D

PLANNING RHEOMETER STUDIES WITH CEMENT PASTE

The factors considering while performing rheological experiments using the dynamic shear rheometer are summarized below. This may be useful for future research scholars working in a similar area.

1. For the current study, parallel plate fixtures were used for both preliminary studies done at IIT Madras and for the actual experiments performed at the Arizona State University. For suspensions like cement paste, wall slip may occur at the interface between the plates and the sample which may lead to erroneous results (Saak *et al.*, 2001; Feys *et al.*, 2018). To prevent wall slippage, the use of serrated or sandblasted fixtures is recommended. For the preliminary studies done at IIT Madras, sandblasted parallel plates were used while for the actual experiments in Arizona State University, parallel plates with serrations were used (see Figure D.1).

(a)

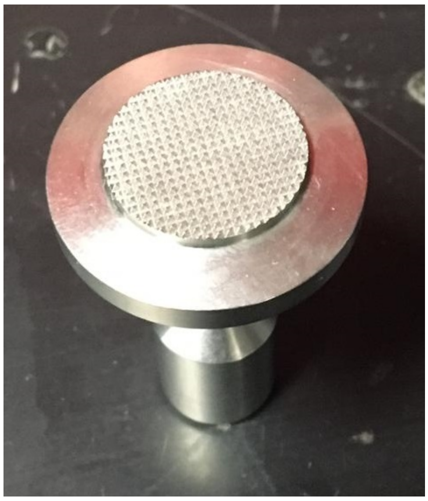

(b)

Figure D.1: (a) 20 mm diameter sandblasted parallel plate fixture used for preliminary studies at IIT Madras (b) 25 mm diameter serrated parallel plate fixture used for the experiments in Arizona State University

2. Diameter of parallel plates used must be such that the torque measurements while testing are always within the instrument torque capacity. For parallel plate geometry, the torque (M) and the shear stress (τ) are related by the following equation ((Macosko and Larson, 1994)):

$$\tau = \frac{M}{2\pi R^3}\left(3 + \frac{d\,lnM}{d\,ln\dot{\gamma}}\right) \tag{D.1}$$

In the above equation, $\dot{\gamma}$ is the strain rate and R is the radiius of the parallel plate. The ratio $\frac{d\,lnM}{d\,ln\dot{\gamma}}$ is one for Newtonian fluids. But for shear thinning fluids like cement paste, the value is less than one. The shear stress that may be obtained while testing cement paste usually lies within a range of $1 - 100$ Pa. Assuming $\frac{d\,lnM}{d\,ln\dot{\gamma}}$ as one for simplicity, the minimum and maximum torque values corresponding to the range of $1 - 100$ Pa can be calculated as $1.57R^3 - 157R^3$. Therefore, the radius of the parallel plates chosen must but such that the range $1.57R^3 - 157R^3$ lies within the instrument torque range suggested by the manufacturer. Also, for other geometries like coaxial, the diameter and height of cylinder must be chosen based on the torque to shear stress conversion equation in a similar manner.

3. Sample drying was observed during the preliminary trials done at IIT Madras. Sample drying can be detected by observing the axial force during measurements. If there is sample drying, the sample shrinks between the parallel plate leading to negative axial forces as time proceeds. This issue was solved by using a solvent trap (Figure D.2).

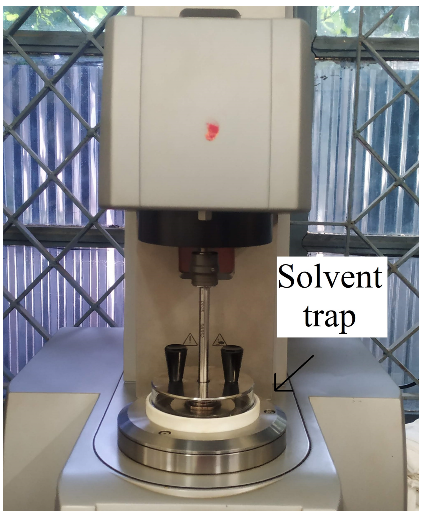

Figure D.2: Use of a solvent trap to prevent sample drying

4. For flow between the parallel plates, performing experiments at high strain rates may lead to instabilities like secondary flows. Hence, the maximum strain rate applied was restricted to 10 s^{-1}. For performing experiments at higher strain rates, the use of a coaxial geometry is more recommended.

LIST OF PAPERS BASED ON THESIS

1. A. V. Rahul, Manu Santhanam, Hitesh Meena, and Zimam Ghani. 3D printable concrete: Mixture design and test methods. *Cement and Concrete Composites*, 97, 13-23 (2019).

2. A. V. Rahul, Manu Santhanam, Hitesh Meena, and Zimam Ghani. Mechanical characterization of 3D printable concrete. *Construction and Building Materials*, 227, 116710 (2019).

3. A. V. Rahul, Abhisek Sharma, and Manu Santhanam. A desorptivity-based approach for the assessment of phase separation during extrusion of cementitious materials. *Cement and Concrete Composites*, 108, 103546 (2020).

4. A. V. Rahul, and Manu Santhanam. Evaluating the printability of concretes containing lightweight coarse aggregates. *Cement and Concrete Composites* 109, 103570 (2020).

5. A. V. Rahul, S. P. Atul Narayan, Narayanan Neithalath, and Manu Santhanam. A thermodynamic framework for modelling thixotropic yield stress fluids: Application to cement pastes. *Journal of Non-Newtonian Fluid Mechanics* 281, 104318 (2020).

6. Shantanu Bhattacherjee, A. V. Rahul, and Manu Santhanam. Concrete 3D printing – progress worldwide and in India. *Indian Concrete Journal*, 94(9), 8-25 (2020).

CURRICULUM VITAE

NAME	:	**A. V. RAHUL**
DATE OF BIRTH	:	26 APRIL 1989

EDUCATIONAL QUALIFICATIONS

2011 **Bachelor of Technology (B.Tech)**

Specialization	:	Civil Engineering
Institution	:	Government Engineering College Thrissur, Kerala

2013 **Master of Technology (M.Tech)**

Specialization	:	Construction Technology and Management
Institution	:	National Institute of Technology Surathkal, Karnataka

Doctor of Philosophy (Ph.D.)

Institution	:	Indian Institute of Technology Madras, Tamil Nadu
Registration	:	14 July 2016

DOCTORAL COMMITTEE

CHAIR PERSON	:	**Dr. K. Ramamurthy** Professor and Head, Department of Civil Engineering, IIT Madras, Chennai.
GUIDES	:	**Dr. Manu Santhanam** Professor, Department of Civil Engineering, IIT Madras, Chennai.
	:	**Dr. Atul Narayan** Assistant Professor, Department of Civil Engineering, IIT Madras, Chennai.
MEMBERS	:	**Dr. J. Murali Krishnan** Professor, Department of Civil Engineering, IIT Madras, Chennai.
	:	**Dr. Amlan K. Sengupta** Professor, Department of Civil Engineering, IIT Madras, Chennai.
	:	**Dr. Gandham Phanikumar** Professor, Department of Metallurgical and Materials Engineering, IIT Madras, Chennai.